PL-TR-92-2199(II)

ELASTIC MODULI AND SEISMIC WAVE ATTENUATION
IN DRY AND SATURATED ROCK:
MODULUS DISPERSION AND ATTENUATION

Robert W. Haupt
Randolph J. Martin, III
Xiao Ming Tang
William Dupree

NEW ENGLAND RESEARCH, INC.
76 Olcott Drive
White River Junction, VT 05001

31 July 1992

Final Report (Volume II)
15 May 1989 - 31 December 1991

DTIC
ELECTE
NOV 12 1992
S E D

APPROVED FOR PUBLIC RELEASE; DISTRIBUTION UNLIMITED

PHILLIPS LABORATORY
Directorate of Geophysics
AIR FORCE MATERIEL COMMAND
HANSCOM AIR FORCE BASE, MA 01731-5000

92-29303

The views and conclusions contained in this document are those of the authors and should not be interpreted as representing the official policies, either expressed or implied, of the Air Force or the U.S. Government.

This technical report has been reviewed and is approved for publication.

Katharine Kadinsky-Cade
for J. Lewkowicz

JAMES F. LEWKOWICZ
Contract Manager
Solid Earth Geophysics Branch
Earth Sciences Division

Donald H. Eckhardt

DONALD H. ECKHARDT, Director
Earth Sciences Division

REPORT DOCUMENTATION PAGE

Public reporting burden for this collection of information is estimated to average 1 hour per response, including the time for reviewing instructions, searching existing data sources, gathering and maintaining the data needed, and completing and reviewing the collection of information. Send comments regarding this burden estimate or any other aspect of this collection of information, including suggestions for reducing this burden, to Washington Headquarters Services, Directorate for Information Operations and Reports, 1215 Jefferson Davis Highway, Suite 1204, Arlington, VA 22202-4302, and to the Office of Management and Budget, Paperwork Reduction Project (0704-0188), Washington, DC 20503.

1. AGENCY USE ONLY (Leave blank)	2. REPORT DATE 7/31/92	3. REPORT TYPE AND DATES COVERED Final Report, 5/15/89 – 12/31/91

4. TITLE AND SUBTITLE Elastic Moduli and Seismic Wave Attenuation in Dry and Saturated Rock: Volume 2: Modulus Dispersion and Attenuation	5. FUNDING NUMBERS PE 62714E PR 9A10 TA DA WUDB Contract F19628-89-C-0097
6. AUTHOR(S) Robert W. Haupt, Randolph J. Martin, III, Xiao Ming Tang, and William Dupree	

7. PERFORMING ORGANIZATION NAME(S) AND ADDRESS(ES) New England Research, Inc. 76 Olcott Drive White River Junction, VT 05001	8. PERFORMING ORGANIZATION REPORT NUMBER

9. SPONSORING/MONITORING AGENCY NAME(S) AND ADDRESS(ES) Phillips Laboratory Hanscom AFB, MA 01731-5000 Contract Manager: James F. Lewkowicz/GPEH	10. SPONSORING/MONITORING AGENCY REPORT NUMBER PL-TR-92-2199(II)

11. SUPPLEMENTARY NOTES

12a. DISTRIBUTION/AVAILABILITY STATEMENT Approved for public release; Distribution unlimited	12b. DISTRIBUTION CODE

13. ABSTRACT (Maximum 200 words)

Four different laboratory techniques were used to determine Young's modulus and extensional wave attenuation as a function of frequency for the same rock specimen while minimizing variations in other important parameters. The data were then pieced together and compared over a net frequency bandwidth ranging from 10^{-2} to 10^6 Hz. Specimens of Sierra White granite and Berea sandstone were analyzed in dry and water saturated states. Dispersion in moduli and attenuation in the dry samples are negligible. Frequency dependent attenuation and modulus dispersion are clearly evident in the saturated samples and attributed to flow of pore fluid, unconfined sample boundaries and sample dimensions.

A cyclic loading technique was used to examine the effects of strain amplitude and water saturation at constant frequency. The modulus and attenuation determined from hysteresis loops are strain amplitude dependent in both dry and saturated states. As strain amplitudes are increased above 5×10^{-6}, the modulus continually drops while attenuation increases. A significant reduction in modulus is observed in the saturated samples that is attributed to a reduction in surface energy at the fluid/rock interface and an unconfined sample radial boundary.

14. SUBJECT TERMS IVE Rock Properties, Elastic Moduli, Attenuation			15. NUMBER OF PAGES 92
			16. PRICE CODE

17. SECURITY CLASSIFICATION OF REPORT unclassified	18. SECURITY CLASSIFICATION OF THIS PAGE unclassified	19. SECURITY CLASSIFICATION OF ABSTRACT unclassified	20. LIMITATION OF ABSTRACT SAR

NSN 7540-01-280-5500

Standard Form 298 (Rev. 2-89)
Prescribed by ANSI Std. Z39-18
298-102

CONTENTS

LIST OF FIGURES AND TABLES

MODULUS DISPERSION AND ATTENUATION

Robert Haupt, Randolph Martin, III, Xiao Ming Tang, William Dupree

New England Research, Inc.

76 Olcott Drive

White River Junction, VT

Large changes in elastic moduli and seismic wave attenuation in the source region resulting from a nuclear explosion influence seismic pulse characteristics observed in the far field. It is concluded from a number of laboratory studies that dispersions in moduli and attenuation occur over several orders of magnitude in frequency. However, these data have been collected using several methods where frequency bandwidth, strain amplitude, sample dimension, boundary conditions and fluid type vary considerably between data sets.

In this study, four different laboratory techniques were used to determine Young's modulus and extensional wave attenuation as a function of frequency for the same rock specimen while minimizing variations in other important parameters. The data were then pieced together and compared over a net frequency bandwidth ranging from 10^{-2} to 10^{6} Hz. Specimens of Sierra White granite and Berea sandstone were analyzed in dry and water saturated states. Dispersions in moduli and attenuation in the dry samples are negligible. Frequency dependent attenuation and modulus dispersion are clearly evident in the saturated samples and attributed to flow of pore fluid, unconfined sample boundaries and sample dimensions.

A cyclic loading technique was used to examine the effects of strain amplitude and water saturation at constant frequency. The modulus and attenuation determined from hysteresis loops are strain amplitude dependent in both dry and saturated states. As strain amplitudes are increased above 5×10^{-6}, the modulus continually drops while attenuation increases. A significant reduction in modulus is observed in the saturated samples that is attributed to a reduction in surface energy at the fluid/rock interface and an unconfined sample radial boundary.

INTRODUCTION

Mechanical rock properties in the vicinity of a high strain seismic source significantly influence the pulse characteristics observed in the far field. Within the source region, strain amplitudes vary several orders in magnitude while the host rock exhibits components of inelastic, anelastic, and elastic behavior. As a result, dominant changes in the seismic pulse occur within a few wavelengths of the source itself. Dispersions in seismic wave velocities, elastic moduli, and seismic wave attenuations are exhibited that depend on the loading conditions and the response of the host rock to loading. These observations can be attributed to the time and strain amplitude dependencies in the anelastic response of rock to varying loading conditions.

Anelastic mechanisms in rock produce a phase lag of strain behind stress and affect velocity, moduli and attenuation. The modulus, M, is represented by a complex quantity (Toksoz and Johnson, 1981),

$$M = M_R + iM_I \tag{1}$$

where M_R and M_I are the real and imaginary parts of the modulus, respectively. The phase lag, ϕ, is a direct measure of the intrinsic loss or attenuation, Q^{-1}. Attenuation can be determined from the energy input to the system relative to the energy lost to the system (Toksoz and Johnson, 1981),

$$Q^{-1} = M_I / M_R = \Delta W / 2\pi W = \tan \phi \tag{2}$$

where W is the elastic energy stored at the maximum stress and strain and ΔW is the loss per cycle.

Laboratory measurements offer a convenient means to determine these properties with imposed conditions similar to those in the source region. It is important to define the correlations between properties determined in the field at seismic frequencies and those determined in the laboratory overlapping seismic or at different frequencies. Significant differences in elastic moduli and wave attenuation have been observed for a given rock

measured with different laboratory and field techniques. A number of investigators have reported frequency, strain amplitude, and fluid saturation effects on M and Q^{-1} in crustal rocks (Gordon and Davis, 1968; Tittmann et al., 1977; Toksoz et al., 1979; Winkler et al., 1979; Spencer, 1981; Dunn, 1986; Paffenholz and Burkhardt, 1989; Lucet et al., 1991).

Spencer (1981) used a cyclic loading technique to examine the effects of frequency and fluid saturation in samples of sandstone, limestone, and granite for frequencies ranging from 4 to 400 Hz. He found that Young's modulus and extensional wave attenuation remained relatively constant over frequency in samples in a vacuum dry state. However, in saturated samples, the modulus and attenuation exhibited dependencies on fluid type and frequency. For all the fluids, similar trends in modulus dispersion and attenuation were observed. Reductions in moduli and increases in attenuation occurred due to the presence of pore fluid. The modulus increased with increasing frequency, eventually converging to the modulus of the dry condition. Attenuation increased with frequency more than an order of magnitude at frequencies above 100 Hz. Moreover, the degree of modulus reduction and attenuation increase showed a pronounced dependence on fluid type. The fluids had similar densities and viscosities but had very different chemical, electrochemical, and dielectric properties. He concluded that electrochemical interactions between the pore fluid and mineral surface were responsible for a reduction in surface energy at the fluid/pore wall interface. In turn, a frequency-dependent softening of the rock was generated. Spencer was able to predict the correlations between modulus dispersion and attenuation in fluid saturated and dry rocks using a Cole-Cole distribution (Cole and Cole, 1941) of stress relaxation times.

Tittmann et al. (1977), Tittmann et al. (1980), Bullau et al. (1984), and Lucet et al. (1991) used a resonant bar technique to measure modulus and Q^{-1} as a function of water saturation at frequencies between 5×10^3 and 2×10^4 Hz for a wide variety of igneous and sedimentary rocks. In general, attenuation rose while moduli dropped as the partial pressure of water increased. For example, as the vapor pressure in a specimen of Berea sandstone was increased from vacuum to 35% relative humidity, Q_E^{-1} rose by a factor of four while Young's modulus dropped 16% in magnitude.

Attenuation and elastic moduli determined at ultrasonic frequencies have been reported by several investigators (e.g. Gist, 1992; Toksoz et al., 1979; Coyner, 1984). At frequencies above 0.5×10^6 Hz, the Young's modulus in water saturated rocks is typically greater than that of dry rock. Extensional and compressional wave attenuations are often larger in dry rock than those of saturated. These observations are the opposite of those observed at frequencies less than 0.5×10^6 Hz. At ultrasonic frequencies, fluid content increases shear wave attenuation while

lowering the shear modulus. Toksoz et al., 1979 also noted that compressional, extensional, and shear wave attenuations decreased with an increase in confining pressure.

Recently, Tang (1991), developed a waveform inversion technique to measure moduli and attenuation in rock samples overlapping resonant bar and ultrasonic frequencies. He reported that attenuation began to increase above 5×10^4 Hz in dry samples of Sierra White granite. This increase was attributed to the decreasing wavelength and scattering interactions with sample grains, heterogeneities, and flaws.

Moduli and attenuation have been shown to change significantly with increasing strain amplitude in a variety of rock types and saturation conditions in experiments where frequency was held constant (Winkler et al., 1979; Johnson and Toksoz, 1980; Bulau et al., 1984; Martin et al., 1990). Winkler et al. (1979) used the cyclic loading technique at frequencies less than 1 Hz to examine the effects of strain amplitude and water saturation on stress-strain hysteresis loops. He observed that large changes in the modulus and attenuation occur in dry rock at strain amplitudes above 10^{-6}; the modulus decreased while attenuation increased. Below this amplitude, the modulus and attenuation typically varied by a small percentage. For saturated samples, the same modulus and attenuation trends were observed. However, the onset of dominant changes in these properties occurred at a slightly lower strain amplitude than 10^{-6}.

Focus of problem

These experimental data clearly demonstrate that elastic moduli and seismic wave attenuation depend on frequency, strain amplitude, fluid saturation, and confining pressure. However, these different laboratory methods are limited to specific frequency bandwidths with little to no overlap of each other. Using a single technique, only portions of certain important events could be measured for a given rock sample. Modulus dispersion and changes in attenuation occur over several orders of magnitude in frequency. For example, Spencer, 1981 was able to measure part of the low frequency end to 400 Hz of predicted attenuation peaks and modulus ramps that are defined from 1 to 10^5 Hz. Other techniques have been used to measure these properties at higher frequencies but strain amplitudes, sample geometries and boundary conditions were considerably different than those of Spencer's experiments. Characterizing the complete frequency dependence for a specific rock by piecing existing data together becomes difficult, since these data come from such diverse sources.

To overcome this problem, it is necessary to perform a series of experiments that quantify rock properties over many orders of magnitude in frequency for a single rock specimen while

holding other conditions constant. The approach here was to use multiple techniques on the same rock core to determine Young's modulus and Q_E^{-1} as a function of frequency, water saturation and strain amplitude.

EXPERIMENTAL PROCEDURE

Two basic studies were performed to examine the influence of frequency, strain amplitude, and water saturation on moduli and attenuation measured in laboratory experiments. The first study investigated the effects of frequency and water saturation over a large frequency band ranging from 10^{-2} to 10^6 Hz. The cyclic loading, resonant bar, wavefrom inversion and ultrasonic velocity methods were employed to determine Young's modulus and Q_E^{-1} as a function of frequency within their respective bandwidths. In the second study, the cyclic loading technique was used to investigate the strain amplitude and stress dependence of moduli and attenuation in dry and water saturated rocks. Stress-strain hysteresis loops with peak strain amplitudes ranging from 10^{-7} to 10^{-4} were generated while holding loading frequency constant at 10^{-1} Hz.

In order to compare the data obtained with each of the methods over the complete bandwidth, it is necessary to account for differences in strain amplitude, sample geometry and sample size required for each technique. Variations in strain amplitude, saturation, preload, and ambient conditions were minimized as much as possible between the different methods. The ultrasonic velocity, resonant bar, and waveform inversion measurements utilize pulse propagation techniques with peak strain amplitudes on the order of 10^{-8} to 10^{-6}. These data were compared with cyclic loading tests with strain amplitudes less than 5×10^{-6}. All measurements were carried out under room dry and fully water saturated states. The radial boundary of the samples was unconfined and at ambient room temperature, pressure and humidity. Table 1 lists the experimental techniques with corresponding sample dimensions and frequency bandwidths.

Measurements were made on representative specimens of two different and commonly found rock types: granites and sandstones. Each rock type has considerable differences in porosity, pore geometry, and other rock properties. Sierra White granite and Berea sandstone specimens from Raymond, CA and Berea, OH, were selected since they have been widely studied in many applications. The pore structure of Sierra White granite is characterized by populations of penny shaped microcracks (Martin et al., 1990). Berea sandstone contains spherical pores situated between cemented quartz grains with a percentage of clay between 10-20%. The porosities of the granite and sandstone samples were 0.9% and 17.8%, respectively.

Table 1 Experimental Techniques, Frequency Bandwidths, Sample Dimensions

Technique	Frequency	Rock Type	Sample Dimensions (mm)	
			length	diameter
Cyclic loading	0.01 - 100 Hz	Sierra White	305	152
		Berea	305	152
Resonant bar	1 - 200 kHz	Sierra White	120	6
		Berea	180	9
		Berea	394	32
		Berea	165	32
Waveform inversion	1 - 200 kHz	Sierra White	150	15
		Berea	150	15
Ultrasonic velocity	700 kHz	Sierra White	40	55
		Berea	40	55

Sample preparation

All samples were cored from a single block in the same orientation; the sample axis normal to bedding. Separate samples were dimensioned for each measurement technique. Test specimens were ground right circular cylinders. Some samples used in the resonant bar apparatus were square rods and are specified in Appendix C. All samples excluding those for the cyclic loading tests were initially vacuum dried for a period of 24 hours, then allowed to equilibrate to room humidity. The specimens were tested in the room dry state first, then they were saturated with water, then jacketed to minimize evaporation losses, and the measurement sequence was repeated. The large samples used in cyclic loading and those in ultrasonic tests were jacketed with cellophane. Resonant bar and waveform inversion samples were wrapped in Teflon tape.

Cyclic Loading (Hysteresis loop)

Cyclic loading tests were conducted on cylindrical samples housed in a servo-controlled loading frame. A continuous sinusoidal axial force was applied to one sample end with an axial ram operating in force-feedback mode. The force was measured with a load cell in series with the sample in the loading column to determine stress. Three axial LVDT displacement transducers were mounted to the sample with circumferential rings and used to determine strain. An axial preload of 1 MPa was applied to minimize mechanical losses across interfaces in the loading column.

Cyclic loads were prescribed from continuous sine functions at single frequencies ranging from 10^{-2} to 10^2 Hz. For frequencies below 5 Hz, the modulus and Q were determined from single loops, with 1400 points of data per cycle. The modulus was determined from the slope of the hysteresis loop (stress over strain) while attenuation was computed from the fractional energy loss per cycle (area inside the loop divided by the maximum stress). For frequencies at and above 5 Hz, up to 200 cycles were collected. Young's modulus and Q_E^{-1} were determined from the Fast Fourier Transforms of the multiple cycle stress and strain sinusoids. The complex modulus was calculated from the ratio of the peak stress and strain spectra. Q_E^{-1} was then computed from the ratio of the real and imaginary parts of the complex Young's modulus.

The experimental procedure was then duplicated for a low loss standard aluminum core with the same dimensions to calibrate the hysteresis of the experimental apparatus. The experimental apparatus, details of the experimental data acquisition, processing, and computation schemes are described further in Appendix A.

Resonant Bar

Benchtop resonant bar experiments were conducted on rock specimens suspended by a fine thread supported by a fixture in a modified desiccator bell-jar. Samples were thin cylindrical or square rods with a length to diameter ratio greater than 10. A standing extensional wave was generated from piezoelectric crystals mounted on the sample ends. A lock-in amplifier was then used to resonant the rod at fundamental resonances and at higher harmonics, up to the 18th harmonic in dry samples. As the mode or harmonic increased, the center frequency also increased. Young's modulus and Q_E^{-1} were determined as a function of frequency from the resonance peaks. Extensional velocity was first computed from the center frequency of the resonant peak and the sample length. Young's modulus was then computed from the velocity and sample density. Q_E^{-1} was computed from the center frequency and half-power bandwidth

7

of the resonance peak. The mass of the piezoelectric crystals and jackets used for the saturated samples were accounted for in a correction factor described by Lucet et al., (1991). Further details on the resonant bar measurements, data processing, and calculations are presented in Appendix B.

Waveform Inversion

Elastic wave velocities and attenuation were determined jointly for frequencies ranging from 10^3 to 2×10^5 Hz. The technique involves measuring waveforms in two cylindrical bars of the same material, but of different length. First, roughly estimated bar velocity and Poisson's ratio were used to propagate the waveform observed in the shorter bar to the length of the longer bar. Guided by the velocity model, the velocity dispersion curve was then computed from the model, the measured phase difference between the propagated waveform and the measured waveform within the longer bar. Using Rayleigh's solution for the low frequency phase velocities, the low frequency portion of the dispersion curve was inverted to obtain an accurate estimate of the bar velocity and Young's modulus.

Q_E^{-1} was computed in the following steps. The waveform of the shorter bar was theoretically continued to the length of the longer bar o match the measured waveform. The waveform inversion then was performed to minimize the amplitude difference between the two waveforms, from which Q_E^{-1} was computed. For further detail on the waveform inversion technique, see Tang (1992). Further details on the waveform inversion measurements are discussed in Appendix C.

Ultrasonic Measurements

A benchtop ultrasonic system was used to record compressional and shear wave travel times and waveforms propagating through the axis of rock cores. The sample core is placed in series between source and receiving piezoelectric ultrasonic transducers housed in the benchtop system. The source transducer was driven with a short electrical pulse with a center frequency of 10^6 Hz. A pneumatic actuator controls a small ram which exerts an axial preload to the sample on the order of 1 MPa. This preload is comparable to that of the cyclic loading experiments. Compressional (P) and shear (S) wave velocities for the rock were obtained by measuring the one-way travel time of a P or S wave through the core and dividing by its sample length. Dynamic Young's modulus was then computed from the compressional and shear wave velocities and sample density.

Q_E^{-1} was computed from values of Q_P and Q_S (P and S wave attenuation) determined with the spectral ratio technique using a low loss standard aluminum core for comparison with rock (Toksoz et al., 1979). P and S waves are recorded for an aluminum core with the same dimensions as the rock specimen. The Fast Fourier Transforms are computed from the P and S wave time series. The Q of the rock is computed from the slope of ratio of the aluminum and rock spectra versus frequency. Further details on the ultrasonic measurement and data reduction are presented in Appendix D.

EXPERIMENTAL RESULTS

The effects of frequency, strain amplitude, and water saturation on Young's modulus and extensional wave attenuation have been examined in specimens of Sierra White granite and Berea sandstone. Four different laboratory techniques were used acquire data over a large net frequency band ranging from 10^{-2} to 10^6 Hz. Dry and water saturated states were then compared as a function of frequency. The cyclic loading technique was employed to determine rock property at strain amplitudes ranging from 10^{-7} to 10^{-4} at constant frequency. Dry and water saturated states were compared as a function of strain amplitude.

Frequency Tests

Sierra White granite

Young's modulus and Q_E^{-1} are compared for room dry and water saturated rock as a function of frequency in Table 2 and shown in Figures 1 and 2. Moduli obtained from cyclic loading, resonant bar (first mode), and ultrasonic velocity measurements are shown in Figure 1. In the dry state, the modulus remains relatively constant with increasing frequency. The modulus determined from the waveform inversion technique at 25×10^3 Hz is more than 15% lower than those at other frequencies. A reduction in modulus is exhibited in saturated samples at frequencies less than 100 Hz. At 10^{-2} Hz, the modulus reduction from dry to saturated states is more than 20%.

As frequency is increased, the modulus of the saturated sample increases from 30.3 GPa at 10^{-2} Hz to 37.3 GPa at 10^2 Hz, converging in magnitude to that of the dry modulus. The resonant bar dry and saturated values differ by less than 1%. At ultrasonic frequencies, the modulus in the saturated sample is considerably larger than that of dry rock modulus by approximately 25%. In addition, the modulus determined in the saturated rock at ultrasonic frequencies is almost double that of the cyclic load value measured at 10^{-2} Hz.

Extensional wave attenuation in Sierra White granite is presented as a function of frequency in Figure 2 for cyclic loading, all modes of the resonant bar, waveform inversion, and ultrasonic measurements. Q_E^{-1} was only determined with the waveform inversion technique in the room dry condition. For dry granite, Q_E^{-1} is consistently less than 0.01 over frequency. A slight increase is observed especially at ultrasonic frequencies. Q_E^{-1} for the saturated condition exhibits a pronounced frequency dependence and is significantly greater than Q_E^{-1} for the dry

10

TABLE 2 FREQUENCY DEPENDENCE SIERRA WHITE GRANITE

technique	DRY STATE			SATURATED STATE		
	frequency (Hz)	Attenuation $(1000/Q_E^{-1})$	Young's mod (GPa)	frequency (Hz)	Attenuation $(1000/Q_E^{-1})$	Young's mod (GPa)
Cyclic Loading	0.01	4.62	38.36	0.01	10.6	30.33
	0.05	2.26	38.36	0.05	12.3	30.34
	0.10	2.68	38.36	0.10	17.5	30.35
	0.50	5.26	38.38	0.50	25.3	30.42
	1.00	4.95	38.40	1.00	24.9	30.50
	5.00	2.53	38.53	5.00	33.0	31.12
	10.00	2.03	38.68	10.00	38.3	31.77
	20.00	0.58	38.90	20.00	48.2	32.75
	30.00	9.32	39.04	30.00	47.6	33.37
	40.00	0.28	39.08	40.00	50.5	33.76
	50.00	6.92	39.04	50.00	59.1	34.02
	60.00		34.27			
	70.00		34.62			
	80.00		35.17			
	90.00		36.04			
	100.00		37.35			
Resonant Bar	11115	6.0	37.62	11135	45.0	36.40
	21940	6.4	37.65	21870	40.5	36.63
	32444	6.9	37.67	32415	40.7	36.86
	42490	0.5	37.70	43563	33.0	37.10
	53321	7.0	37.72	53138	34.8	37.30
	63737	7.1	37.74	63106	30.4	37.52
	73634	7.6	37.77	72934	30.4	37.73
	85257	7.4	37.79	74608	26.1	37.77
	96117	7.4	37.82	95070	28.9	38.21
	107841	8.1	37.85			
	118036	7.6	37.87			
	129730	8.4	37.90			
	141193	7.5	37.92			
	50809	8.5	37.95			
	161971	9.0	37.97			
	172541	7.7	38.00			
	182386	8.6	38.02			
	193475	8.3	38.05			
	204633	7.9	38.07			
	215994	7.6	38.10			
	225719	7.4	38.12			
Waveform Inversion	40000	7.8				
	60000	9.4				
	80000	9.0				
	100000	8.1				
	120000	9.6				
	140000	10.3				
Ultrasonic	700000	18.9	39.22	700000	12.4	51.26

Sierra White granite

(o) dry
(●) saturated

hys loop

res bar

ultra

wav inv

Young's modulus (GPa)

Frequency (Hz)

FIGURE 1

12

Sierra White granite

(o) dry
(●) saturated

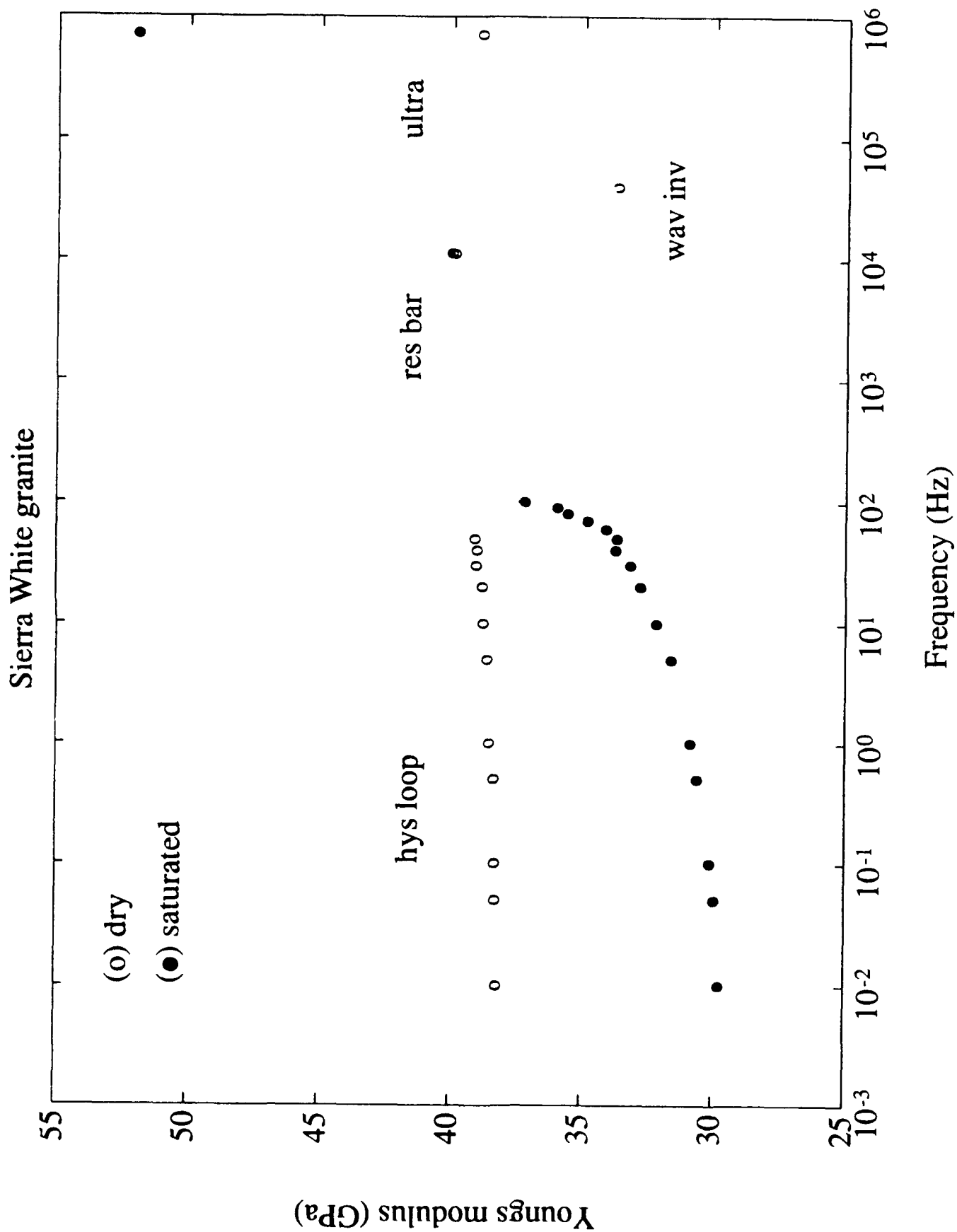hys loop

res bar

ultra

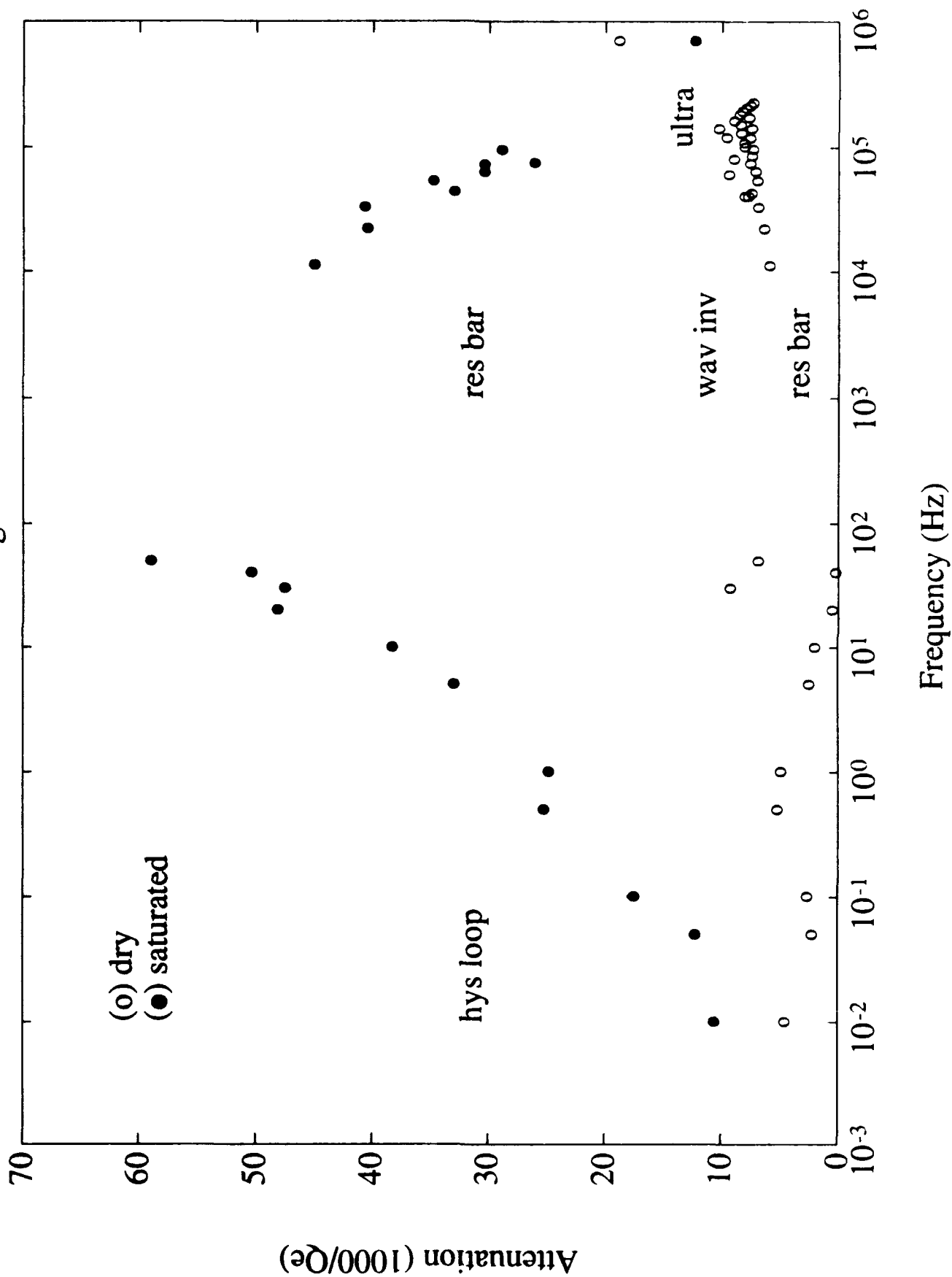wav inv

res bar

Frequency (Hz)

Attenuation (1000/Qe)

FIGURE 2

13

state at all frequencies less than 10^5 Hz. Attenuation measured in the large sample with the cyclic loading technique continually increases between 10^{-2} and 50 Hz, as much as a factor of six. In contrast, the resonant bar data show a large decrease from 0.045 to 0.025 as frequency increases from 10^3 to 10^5 Hz. Attenuation in the saturated sample drops even further at ultrasonic frequencies, just slightly less than that of the dry rock.

Berea Sandstone

The effects of frequency on Young's modulus and Q_E^{-1} for room dry and water saturated sandstone are presented in Table 3 and shown in Figures 3 and 4. A large data set was compiled for the dry state including cyclic loading, resonant bar, and ultrasonic measurements. However, cyclic loading data are only reported for the saturated sample. The modulus in the dry state remains relatively constant over frequency. A slight second order increase in modulus is observed, particularly at ultrasonic frequencies. A significant reduction in Young's modulus in saturated sandstone is also documented that is lower than the dry values by approximately 40% at all frequencies less than 10^2 Hz. The modulus of the saturated sample increases less than 6% over frequencies to 10^2 Hz.

Extensional wave attenuation in Berea sandstone is shown as a function of frequency in Figure 4. Values of attenuation in dry specimens were determined using all four techniques and compared. For a given technique, changes in Q_E^{-1} are relatively independent of frequency. Cyclic loading and waveform inversion attenuation data are approximately in the same range, averaging 0.03. However, resonant bar attenuations are typically three times less in magnitude than cyclic loading and waveform inversion data. Attenuation determined with the ultrasonic technique is almost double than those of cyclic loads and waveform inversion data.

Attenuation measurements in saturated sandstone are reported only for the cyclic loading technique. In these data, Q_E^{-1} is less than that of the dry state. For the large sandstone sample changes Q_E^{-1} in appear to be independent of frequency using this technique.

Strain Amplitude Tests

Sierra White granite

The effects of strain amplitude and water saturation are examined using the cyclic loading technique. Stress-strain hysteresis loops were generated at a frequency of 10^{-1} Hz and analyzed. Young's modulus and Q_E^{-1} for both the room dry and saturated conditions are presented as a

TABLE 3 FREQUENCY DEPENDENCE BEREA SANDSTONE

technique	DRY STATE			SATURATED STATE		
	frequency (Hz)	Attenuation $(1000/Q_E^{-1})$	Young's mod (GPa)	frequency (Hz)	Attenuation $(1000/Q_E^{-1})$	Young's mod (GPa)
Cyclic	0.01	35.3	9.14	0.01	22.2	5.61
Loading	0.05	35.1	9.23	0.05	22.6	5.71
	0.10	33.4	9.42	0.10	22.9	5.63
	0.50	35.2	9.56	0.50	20.3	5.85
	1.00	32.1	9.60	1.00	25.5	5.89
	5.00	30.6	9.75	5.00	19.1	5.96
	10.00	33.3	9.79	10.00	19.2	6.00
	20.00	36.8	9.87	20.00	21.5	6.06
	30.00	35.7	9.92	30.00	22.2	6.12
	40.00	33.4	9.87	40.00	23.9	6.18
	50.00	31.8	10.09	50.00	23.2	6.22
	60.00					6.44
	70.00					6.28
	80.00					6.35
	90.00					6.43
	100.00					6.33
Resonant	6064	6.3	10.41			
Bar	12220	6.5	10.56			
	17895	6.4	10.07			
	23955	6.7	10.15			
	30164	5.0	10.30			
	36229	6.8	10.32			
	42290	7.0	10.33			
	47668	7.2	10.05			
	53883	7.2	10.15			
	60287	7.0	10.29			
	65500	7.4	10.03			
	72240	6.9	10.26			
	78634	8.8	10.35			
	84174	9.8	10.23			
	89637	7.6	10.11			
	95447	11.1	10.07			
	101330	8.6	10.05			
	107545	9.2	10.10			
	111449	9.7	9.74			
	9762	9.1	9.06			
	10490	9.6	9.63			
	5661	9.2	9.23			
	11250	9.1	9.12			
	22500	9.1	9.11			
	2781	10.6	10.60			
	8317	11.5	11.50			

TABLE 3 FREQUENCY DEPENDENCE BEREA SANDSTONE

technique	DRY STATE			SATURATED STATE		
	frequency (Hz)	Attenuation $(1000/Q_E^{-1})$	Young's mod (GPa)	frequency (Hz)	Attenuation $(1000/Q_E^{-1})$	Young's mod (GPa)
Waveform Inversion	10000	25.7				
	20000	29.6				
	30000	29.9				
	40000	31.3				
	60000	28.9				
	80000	27.7				
Ultrasonic	700000	55.6	9.71	700000	12.35	51.26

Berea sandstone

FIGURE 3

17

Berea sandstone

(o) dry
(●) saturated

hys loop

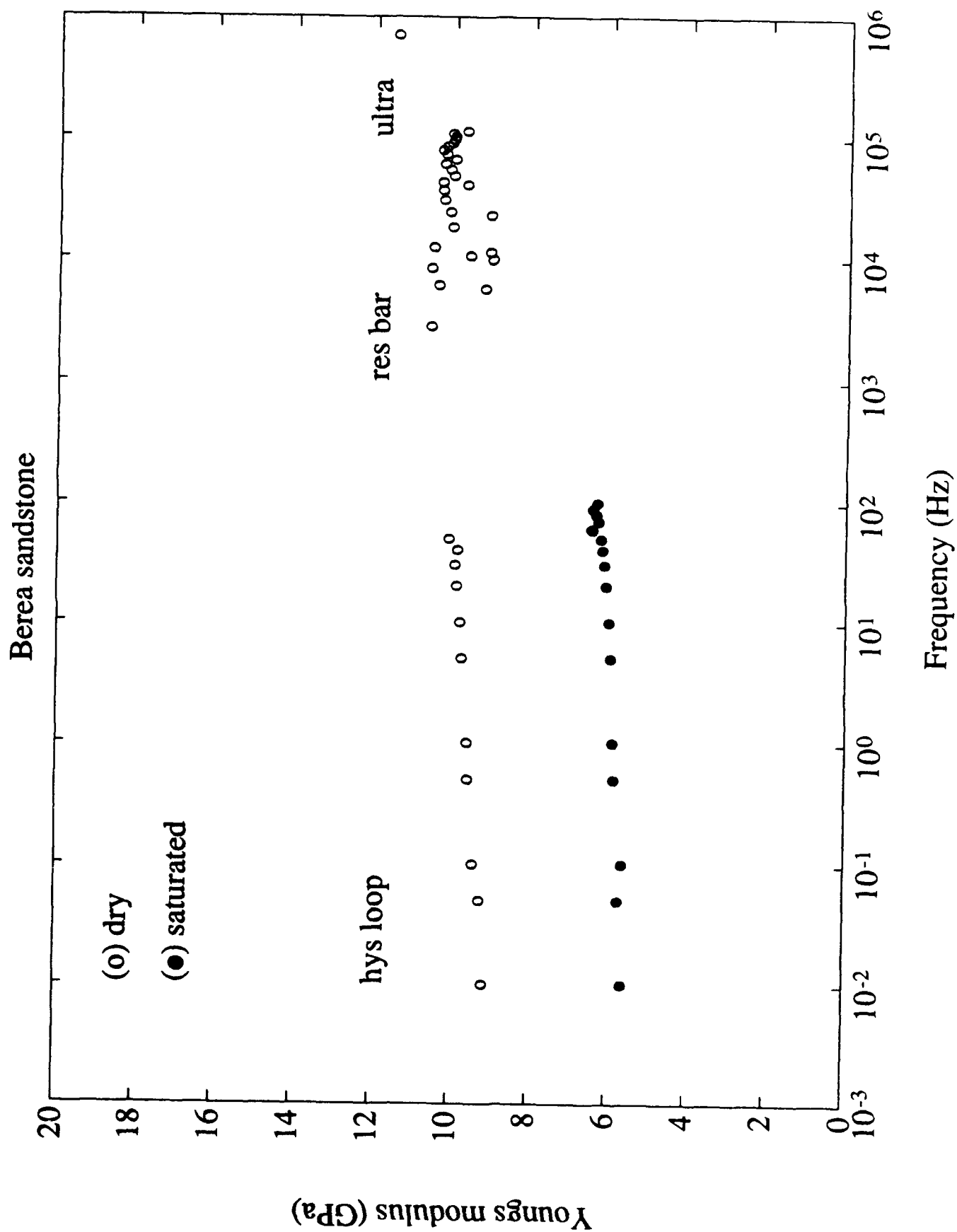wav inv

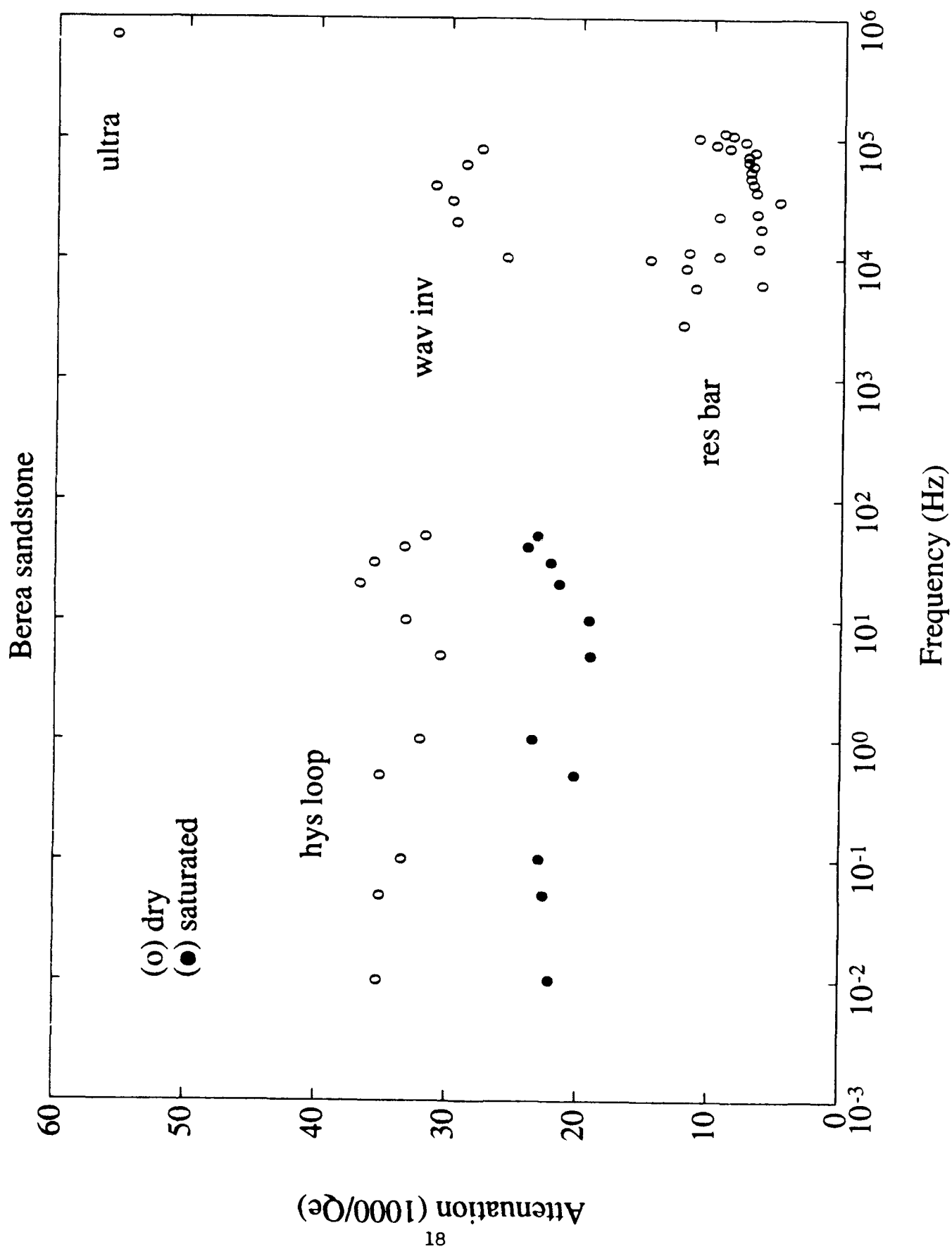ultra

res bar

Frequency (Hz)

Attenuation (1000/Qe)

FIGURE 4

18

function of strain amplitude in Table 4 and shown in Figures 5 and 6. In Figure 5, Young's modulus increases with strain amplitude in the room dry and saturated samples. The changes were most pronounced for strains above 5×10^{-6}. The modulus trends of the dry and saturated states are very similar. However, these trends are offset by a reduction in modulus from dry to saturated states.

An increase in strain amplitude also produces an increase in Q_E^{-1} that has similar trends in both the dry and saturated specimens as depicted in Figure 6. Q_E^{-1} remains constant below strain amplitudes of 5×10^{-6} in dry granite, but shows a sharp increase above this amplitude. For the saturated condition, the sharp increase in Q_E^{-1} is shifted to strain amplitudes as low as 10^{-7} to 10^{-6}. It appears that the rate of increase at high strain amplitudes is approximately the same for dry and saturated states.

Berea Sandstone

Strain amplitude affects Young's modulus and Q_E^{-1} in both the room dry and saturated sandstone sample. Results are presented in Table 5 and are shown in Figures 7 and 8. In Figure 7, the room dry and saturated samples exhibit a decrease in modulus with increasing strain amplitude, particularly above 5×10^{-6}. Data are also presented for 10 Hz hysteresis loops for comparison at a higher frequency in the saturated sandstone. The differences in moduli computed at 10^{-1} and 10 Hz are very small at a given strain amplitude. These data are consistently lower by as much as 40% at strain amplitudes of 10^{-6} compared to those of the dry state. This difference is less than 20% at larger strain amplitudes.

In dry and saturated sandstone, an increase in strain amplitude produces an increase in Q_E^{-1}, as depicted in Figure 8. For dry and saturated states, attenuation increases significantly at strain amplitudes above 5×10^{-6}. A small spread in the data is exhibited between the dry and saturated states. In these data, the attenuation in saturated sandstone is slightly less than that of dry rock above a strain of 5×10^{-6}.

TABLE 4 STRAIN AMPLITUDE DEPENDENCE SIERRA WHITE GRANITE

(axial preload 1 MPa)

	DRY STATE			SATURATED STATE		
technique	strain amp 10^{-6}	Attenuation $(1000/Q_E^{-1})$	Young's mod (GPa)	strain amp 10^{-6}	Attenuation $(1000/Q_E^{-1})$	Young's mod (GPa)
	0.1 Hz			0.1 Hz		
Cyclic	0.3	4.6	38.45	0.6	7.5	30.26
Loading	0.7	4.6	38.40	1.1	11.5	30.30
	1.5	5.2	38.35	1.9	12.4	30.17
	2.9	5.0	38.38	2.9	17.5	29.96
	7.5	7.6	37.88	5.5	25.1	29.19
	17.5	15.2	36.81	12.6	35.1	27.92
	33.2	25.3	35.56	22.9	40.1	26.83
				33.9	45.1	25.92

TABLE 5 STRAIN AMPLITUDE DEPENDENCE BEREA SANDSTONE

(axial preload 1 MPa)

	DRY STATE			SATURATED STATE		
technique	strain amp 10^{-6}	Attenuation $(1000/Q_E^{-1})$	Young's mod (GPa)	strain amp 10^{-6}	Attenuation $(1000/Q_E^{-1})$	Young's mod (GPa)
	0.1 Hz			0.1 Hz		
Cyclic	1.5	26.3	9.56	2.2	29.4	5.82
Loading	3.3	27.7	9.56	4.1	29.6	5.65
	4.8	29.6	9.45	6.9	42.2	5.43
	7.2	30.2	9.56	10.1	53.0	5.24
	9.9	40.9	8.58	15.6	68.5	5.01
	14..8	53.1	8.59	39.1	94.8	4.48
	17.9	66.1	8.21	51.2	97.8	4.31
	38.8	98.1	7.34			
	73.0	124.2	6.67			
	107.4	147.2	6.10			
	192.9	173.2	5.45			
				10 Hz		
				1.6	25.4	5.87
				4.2	30.3	5.85
				8.1	39.5	5.52
				14.8	49.8	5.18
				26.7	100.8	4.87

Sierra White granite

(o) dry
(●) saturated

0.1 Hz hysteresis loop

Strain Amplitude

FIGURE 5

Youngs modulus (GPa)

50 45 40 35 30 25 20

10^{-7} 10^{-6} 10^{-5} 10^{-4}

21

Sierra White granite

(o) dry
(●) saturated
0.1 Hz hysteresis loop

Attenuation (1000/Qe)

Strain Amplitude

FIGURE 6

22
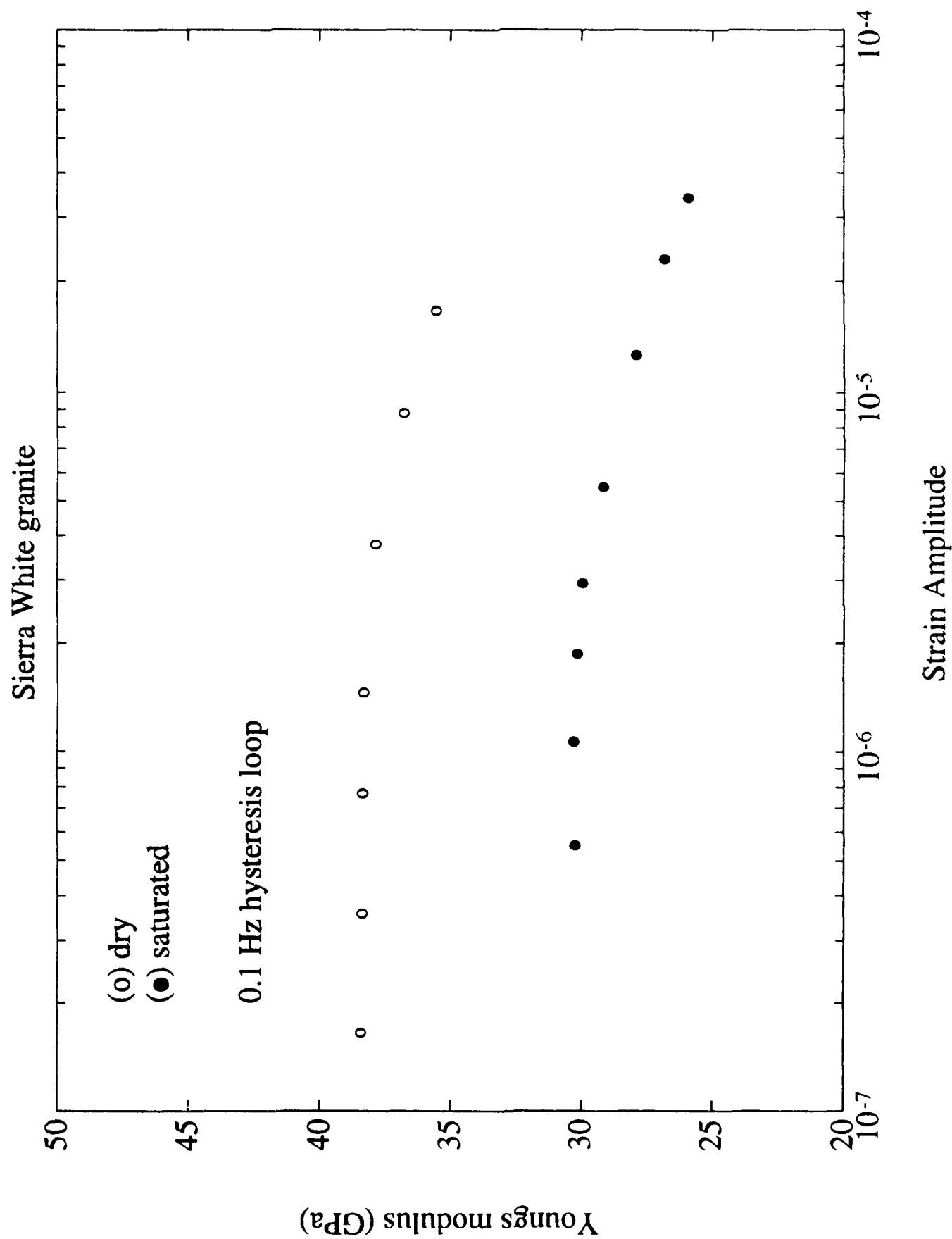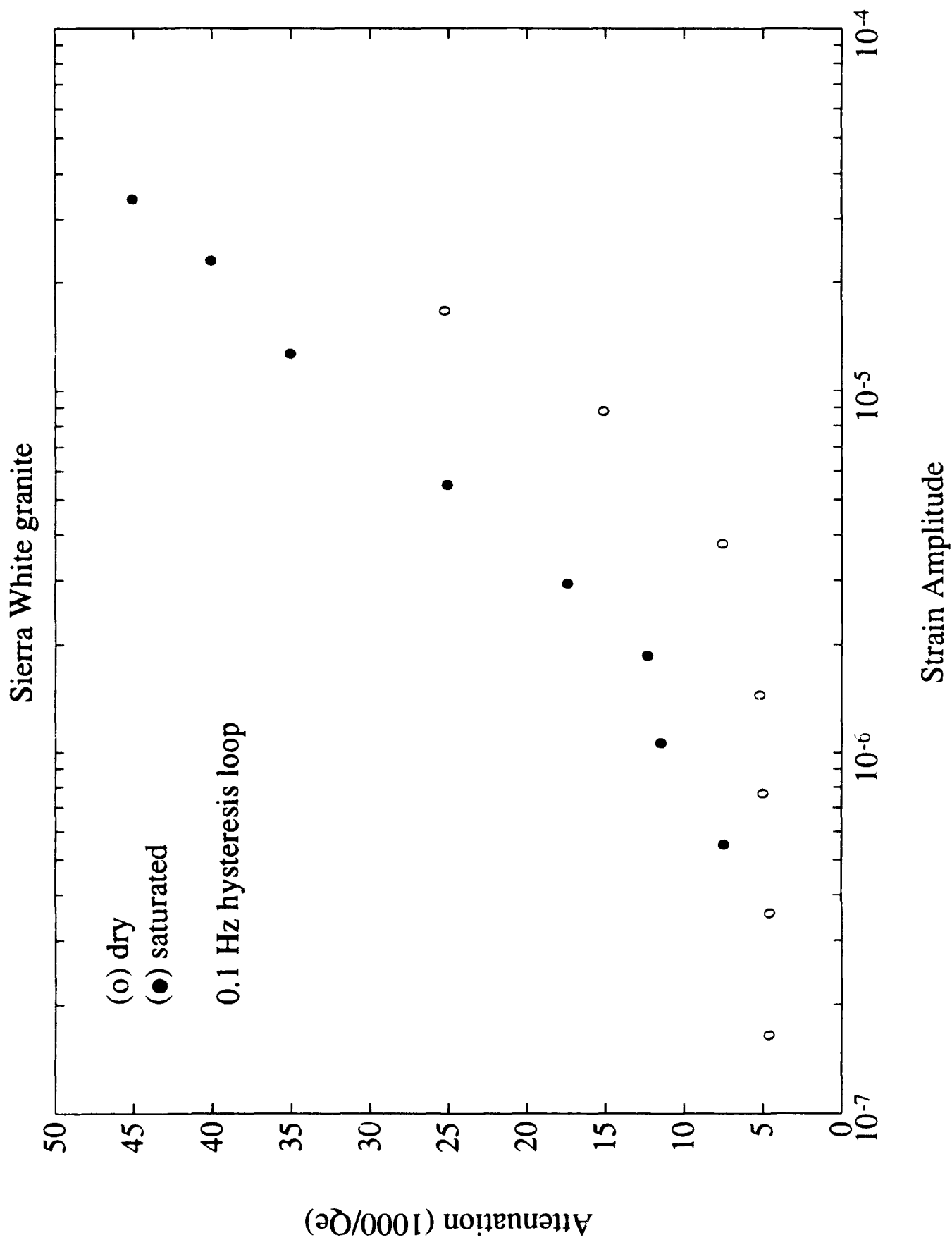
Berea sandstone : Effect of strain amplitude on modulus

Hysteresis loops

(x) dry sample (0.1 Hz)
(o) saturated sample (0.1 Hz)
(+) saturated sample (10 Hz)

Young's modulus (GPa)

axial strain (amplitude)

FIGURE 7

23
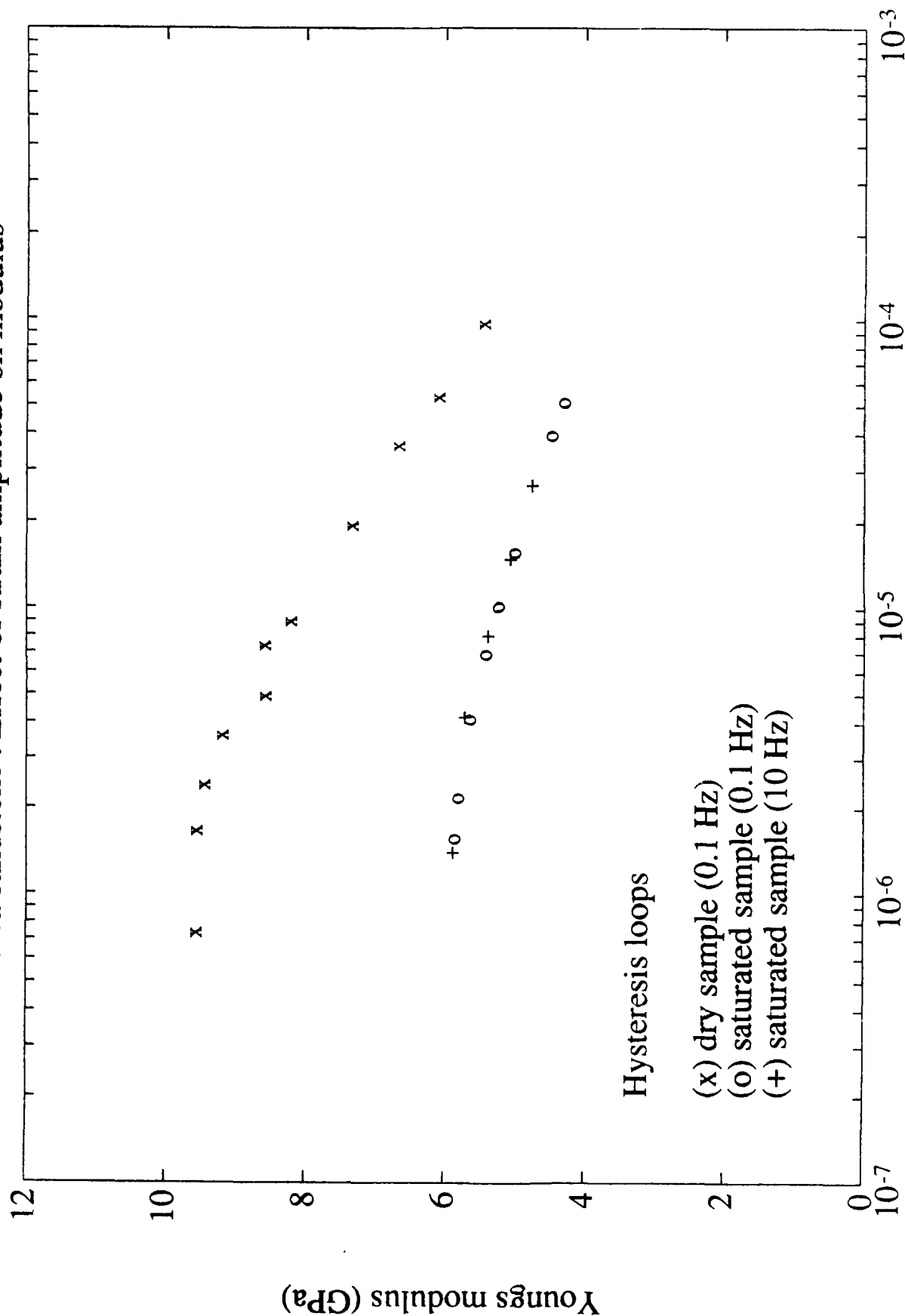
Berea sandstone : Effect of strain amplitude on attenuation

Hysteresis loops

(x) dry sample (0.1 Hz)
(o) saturated sample (0.1 Hz)
(+) saturated sample (10 Hz)

attenuation (1000/Qe)
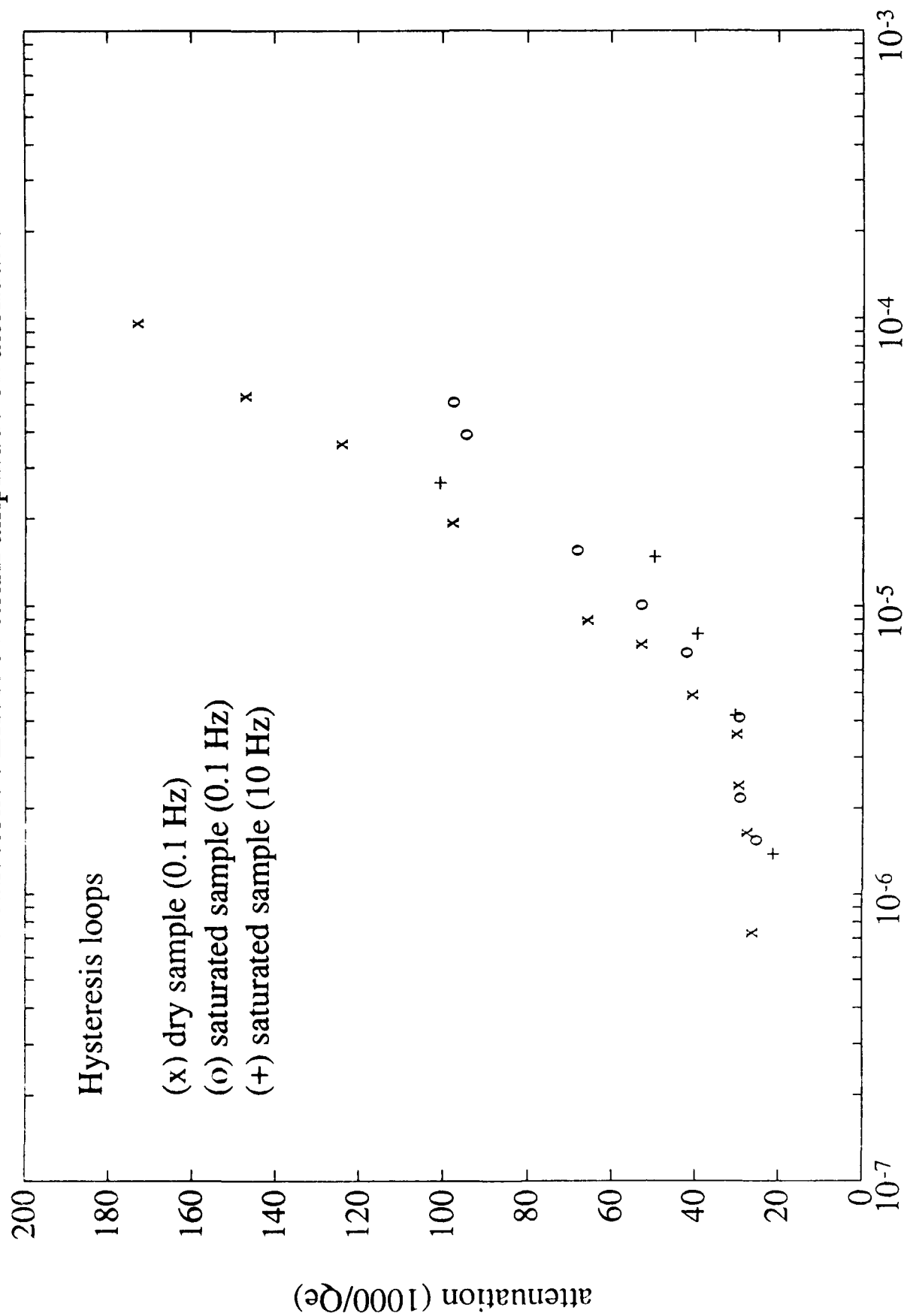
axial strain (amplitude)

FIGURE 8

24

DISCUSSION

Changes in moduli and attenuation in granite and sandstone samples are observed as functions of frequency and strain amplitude. The magnitude and frequency dependence of these rock properties are strongly affected by the presence of pore fluid. Moreover, there are considerable differences exhibited between rock types. As the axial load is increased, producing strain amplitudes above 5×10^{-6}, a predominant strain amplitude dependence is observed in both rock types in dry and saturated states. These dependences are controlled by the pore structure, sample dimension, sample geometry, and loading conditions.

The effects water saturation and frequency

Dry state

Modulus dispersion and changes in attenuation are independent of frequency to the first order in dry granite and sandstone. However, frequency dependences are exhibited above 10^5 Hz. Trends in resonant bar, waveform inversion and ultrasonic data show an increase in attenuation. This increase can be attributed to scattering effects where the wavelength begins to approach the scale of sample grain size, pore size, and heterogeneities. This increase is more pronounced in the sandstone than the granite. The pores and sample inconsistencies in the sandstone are characterized to be larger than those in granite.

A large variation in attenuation is evident in Berea sandstone between the waveform inversion and resonant bar data at overlapping frequencies. Resonant bar attenuation measurements are particularly sensitive to changes in humidity (Tittmann, et al., 1977 and 1980). Humidity effects are also documented in Appendix C describing resonant bar experiments in greater detail. When vacuum dry samples are exposed to atmosphere conditions, attenuation increases by several orders of magnitude as the sample absorbs humid air over time. The associated modulus is also observed to decrease between 10 - 20% over the time span. Resonant bar and waveform inversion measurements were obtained in two different building locations and times of year. The resonant bar measurements for the sandstone were obtained in several winter months where humidity was low. The lower attenuations are then attributed to humidity and the ability of the sample to absorb moisture. Little to no differences in attenuation are observed between the waveform inversion and resonant bar data in dry granite. The granite samples have a much lower permeability than sandstone, in turn humidity infiltration into

25

granite may not play as much as a factor. The humidity dependence in waveform inversion measurements has not been investigated.

Saturated state

The presence of pore fluid, change in frequency and sample dimensions have significant and inter-related effects on the modulus and attenuation. A large reduction in Young's modulus is documented in the samples using the cyclic loading tests, especially at very low frequencies. The modulus reduction can be attributed to a decrease in surface energy along the grain boundaries, microcracks, and pores within the rock caused by the pore fluid (Murphy, 1982; Bulau et al., 1984; Murphy et al., 1984). Strain in rock causes solid bonds to break in the vicinity of crack tips and junctions between grain boundaries increasing the net surface area. Anions in pore fluid are adsorbed onto the newly exposed surfaces to complete the broken solid bonds. Cations are then hydrated to the highly viscous anion layer forming an electric double layer at the mineral/fluid interface. The bonds in the electric double layer are considerably weaker than solid bonds, in turn the surface energy has been reduced. Spencer, 1981 and Pride and Morgan, 1991 concluded that the surface energy of the double layer depends pore fluid chemistry, the mineral surface electrical charge, and electrochemical interactions occurring between the mineral and fluid. As a result, reductions in the modulus depend on the electrolyte species and concentrations contained in the pore fluid.

Tap water was used to saturate each specimen for all experiments. It is assumed that differences in electrochemistry for the experiments were negligible. Results show that the modulus reduction is more pronounced in sandstone than in granite. This is due, at least in part, to the pore geometry and solid-solid bond strength between grain boundaries. Cementation in sandstone is weaker than the quartz grains and strains more easily to stress. The addition of pore fluid softens the rock even further, especially compared to a crystalline rock.

A number of mechanisms are primarily responsible for an increase in wave attenuation in saturated rocks. Energy is lost to move pore fluid. Biot, 1956; Walsh, 1969; O'Connell and Budiansky, 1977; and Mavko and Nur, 1979, have developed fluid-mechanical models to describe viscous and inertial effects of pore fluid as dominant mechanisms of attenuation. The elastic deformation resulting from a stress produces pressure gradients in pore fluid and generates fluid flow. The viscous drag of the pore fluid also depends on the bond strength of the electric double layer that is controlled by fluid electrochemistry (Spencer, 1981, and Pride and Morgan, 1991). The stronger the bond strength between the fluid and mineral, the stronger

26

is the coupling between the fluid and mineral surface. Spencer demonstrated that attenuation varied considerably at a given frequency in the same rock specimen using fluids with different electrical properties and electrolytes but with similar densities and viscosities.

Frequency dependence in saturated rock

Both the modulus and attenuation exhibit a frequency dependence, especially in Sierra White granite. Young's modulus almost doubles over the entire frequency range in the granite specimens. A dramatic increase in the modulus is observed with increasing frequency in the large sample used in the cyclic loading tests. The frequency dependence of the modulus can be attributed to the apparent viscosity and fluid flow within the sample. When the cyclic loading rate exceeds the time constant for fluid diffusion within the pore space, the specimen begins to stiffen due to the compression of the pore water. In turn, the effective modulus increases. The point at which the relative stiffening occurs is directly related to the sample diameter, pore geometry, and the boundary conditions for fluid flow within the specimen (Spencer, 1981; Dunn, 1987).

At frequencies between 10^{-2} and 10^2 Hz, attenuation increases from 0.012 to 0.060 in granite. This increase can be attributed to a number of mechanisms. Fluid-mechanical models also describe changes in attenuation with loading frequency. The viscous drag of the pore fluid is strongly dependent on frequency. As the loading frequency increases, the rate of fluid flow increases and viscous losses control the attenuation. Once the deformation rate is significantly greater then the pore fluid response, stiffening occurs and attenuation decreases. This decrease is clearly demonstrated in the resonant bar and ultrasonic data.

Fluid flow is also governed by the sample pore geometry, sample dimensions and boundary conditions imposed by the experimental set up. Relatively small increases in the modulus and attenuation in Berea sandstone are observed over frequency (only cyclic loads were examined in this study). Differences in modulus dispersion and attenuation in the granite and sandstone samples are primarily attributed to pore geometry. The permeability of the granite specimen is considerably smaller than that of sandstone. As a result, pressure gradients that drive the fluid flow build up at a faster rate in the granite with frequency. In turn, the rock stiffens at a faster rate and attenuation becomes significantly greater with frequency. Another critical factor is that the specimens were tested with a free radial boundary under drained conditions. Flow in and out of the sample is considerably larger for the sandstone sample than granite. The magnitude of the pressure gradients in sandstone are in turn smaller and stiffening of the fluid was

minimal. The rate of stiffening is also controlled by sample radius. Dunn, 1986, showed that stiffening occurred at lower frequencies with larger diameter samples.

The effect of strain amplitude

Young's modulus and seismic wave attenuation clearly exhibit a strain amplitude dependence in dry and saturated Sierra White granite and Berea sandstone. For rocks with low aspect ratio cracks (granite) or elliptical pores (sandstone), the modulus has been shown to decrease while attenuation increases with increasing strain amplitude (Winkler et al., 1979). Walsh, (1969), Mavko (1979), and Winkler et al., (1979) have proposed frictional mechanisms in which sliding on microcracks dissipates energy, observed as attenuation. Alternative mechanisms based on changes in surface energy and movement of fluid films in partially saturated rocks have been proposed by Spencer, (1981), Mavko and Nur, (1979), Bulau et al., (1984) and Murphy et al. (1984).

The dry and water saturated specimens showed similar trends in modulus and attenuation changes with strain amplitude. The modulus trends in dry and saturated granite mimic each other closely. The significant differences in these trends are in their magnitudes where the modulus in the saturated state is consistently lower than dry state by 25%. The attenuation is larger at a given strain amplitude in saturated granite. However, there are subtle but important differences that occur at different strain amplitudes.

Below 5×10^{-6} strain, the modulus and attenuation are relatively independent of strain amplitude in dry granite. Above this threshold, the modulus decreases while attenuation rises with strain amplitude. The deformation and strain due to loading is able to overcome frictional forces and initiate sliding of surfaces within microcracks. In turn, the strain becomes more nonlinear with increasing stress and effects the modulus and attenuation. These nonlinear effects are discussed in further detail by Winkler et al., 1979 and Martin et al., 1990. In saturated rock, attenuation begins to rise at a lower strain amplitude threshold. The hydrated layers on mineral surfaces reduce surface energy and the forces resisting microcrack sliding. This threshold occurs between 10^{-7} to 10^{-6} strain in the granite.

The strain amplitude dependence of the modulus and attenuation in Berea sandstone is similar to that of the granite. The modulus trends in the dry and saturated sandstone are different. The modulus in the dry rock drops at a faster rate than that in saturated rock with increasing strain amplitude. Attenuation in dry and saturated sandstone are approximately the

same value at a given strain amplitude. It is difficult to explain these results. One possible explanation is that the clay content in Berea sandstone may have an effect on the modulus and attenuation. Clay surfaces have a significant effect on the adsorption and desorption processes involving pore fluid. In turn, clays can swell when in contact with water and perhaps lower attenuation. As a result, the net effect of clay and fluid flow on attenuation may be equivalent to the dry state in clay rich sandstone.

CONCLUSIONS

Mechanical rock properties such as elastic moduli and seismic wave attenuation were determined experimentally in the laboratory. Four different techniques were used to compare moduli and attenuation over many orders of frequency. Data were examined at frequencies and strain amplitudes that are observed in the explosive source region. These data can then be incorporated into existing models to compute far field seismic pulse characteristics. By characterizing rock properties at a test site, it may be possible to discriminate the yields of nuclear explosions from natural teleseir nic events using far field signals.

The moduli and attenuations determined from the experiments have been compared as a function of frequency, strain amplitude, and saturation. It is concluded from the data that:

(1) The changes in modulus and attenuation are small in the dry Sierra White granite and Berea sandstone. Modulus dispersion and frequency dependent attenuation are exhibited in the saturated samples. The frequency dependence is attributed to the flow of pore fluid caused by the loading stress and sample geometry. Increased stiffening occurs with frequency which causes an increase in modulus. At higher frequencies, the fluid motion cannot keep up with the rate of deformation. As a result, attenuation decreases and approaches that of dry rock.

(2) The effect of saturation in the unconfined samples produces a significant reduction in Young's modulus and increase in attenuation at low frequencies. A reduction in surface energy caused by the presence of pore fluid softens the rock lowering the modulus. Fluid flow and viscous drag increase attenuation.

(3) Both the modulus and attenuation are strain amplitude dependent in dry and saturated samples. The modulus decreases while attenuation decreases significantly with increasing strain amplitude, especially above 5×10^{-6} strain in dry rock and is attributed to nonlinear strain in response to linear stress. This threshold shifts to 10^{-7} to 10^{-6} in saturated granite. The presence of clay may raise these thresholds in saturated sandstone.

REFERENCES

Biot, M.A., 1956, Theory of propagation of elastic waves in fluid-saturated porous solid. I. Low frequency range, J. Acoust. Soc. Am., 28, 168-178.

Bulau, J.R., B.R. Tittmann, M. Abdel-Gawad, and C. Salvado, 1984, The role of aqueous fluids in the internal friction of rock: J. Geophys. Res., 89(B6), 4207-4212.

Coyner, K.B., 1984, Effects of stress, pore pressure, and pore fluids on bulk strain, velocity, and permeability in rocks: Ph.D. thesis, Massachusetts Institute of Technology

Dunn, K.J., 1986, Acoustic attenuation in fluid-saturated porous cylinders at low frequencies: J. Acoustic. Soc. Am. 79(6), 1709-1721.

Dunn K.J., 1987, Sample boundary effect in acoustic attenuation of fluid-saturated porous cylinders: J. Acoustic. Soc. Am. 81(5), 1259-1266.

Gardner, G.H.F., 1962, Extensiona' waves in fluid-saturated porous cylinders: J. Acoustic Soc.Am. 34(1), 36-40.

Gist, G.A., 1992, Viscous attenuation mechanisms for wave propagation in fluid-saturated sandstones, submitted to J. Acoust. Soc. Am.

Gordon, R.B.. and L.A. Davis, 1968, Velocity and attenuation of seismic waves in imperfectly elastic rock: J. Geophys. Res., 73, 3917-3935.

Lucet, N., P.N. Rasolofosaon, and B. Zinsner, 1991, Sonic properties of rocks under confining pressure using the resonant bar technique: J. Acoust. Soc. Am 89(3), 980-990.

Martin, R.J.,III, K.B. Coyner, and R.W. Haupt, 1990, Physical property measurements on granites related to the Joint Verification Experiment: DARPA Report F19628-89-C-0097, GL-TR-90-0171, ADA230571.

Mavko, G.M., 1979, Frictional attenuation: An inherent amplitude dependence: J. Geophys. Res., 84, 4769-4775.

Mavko, G. and A. Nur, 1979, Wave attenuation in partially saturated rocks: Geophysics, 44, 161-178.

Murphy, W.F.,III, 1982, Effects of partial water saturation on attenuation in Massilon sandstone and Vycor porous glass: J. Acoust. Soc. Am., 71(6), 1458-1468.

Murphy, W.F.,III, K.W. Winkler and R.L. Kleinberg, 1984, Frame Modulus Reduction in Sedimentary Rocks: The Effect of Adsorption on Grain Contacts: J. Geophys Res. Lett, 9, 805-808.

O'Connell, R.J. and B. Budiansky, 1977, Viscoelastic properties of fluid-saturated cracked solids: J. Geophys. Res., 82, 5719-5735.

Pride, S.R., and F.D. Morgan, 1991, Electrokinetic dissipation induced by seismic waves, Geophysics, 56, no.7, 914-925.

Paffenholz, J. and H. Burkhardt, 1989, Absorption and modulus measurements in the seismic frequency and strain range on partially saturated sedimentary rocks: J. Geophys Res., 94, 9493-9507.

Spencer, J.W., 1981, Stress relaxations at low frequencies in fluid-saturated rocks: Attenuation and modulus dispersion: J. Geophys. Res., 86, 1803-1812.

Tang, X., 1992, A waveform inversion technique for measuring elastic wave attenuation in cylindrical bars: Geophysics, 57, no.6, 854-859.

Tittmann, B.R., L. Ahlberg, H. Nadler, J. Curnow, T. Smith and E.R. Cohen, 1977, Internal friction quality-factor Q under confining pressure: Proceedings of the Eighth Lunar Science Conference, 1209-1224.

Toksoz, M.N.,D.H. Johnston, and A. Timur, 1979, Attenuation of seismic waves in dry and saturated rocks: I. Laboratory measurements: Geophysics, 44, 681-690.

Toksoz, M.N., and D.H. Johnston, 1981, Seismic Wave Attenuation: Geophysics reprint series, No. 2.

Walsh, J.B., 1969, Seismic wave attenuation in rock due to friction: J. Geophys. Res., 71, 2591-2599.

White, E. J., 1986, Biot-gardner theory of extensional waves in porous rocks: Geophysics, 51, 742-745.

Winkler, D., A. Nur,and M. Gladwin, 1979: Friction and seismic attenuation in rocks. Nature, 277, 528-531.

APPENDIX A

CYCLIC LOADING

CYCLIC LOADING (Hysteresis Loop)

Young's modulus and Q_E were determined from steady-state stress and strain data measured during unconfined cyclic loading tests. A continuous sinusoidal axial load was applied to cylindrical rock samples. The cylindrical sample dimensions were 6 inches in diameter by 12 inches in length. Measurements were performed on room dry and saturated samples. The sample was mounted in a servocontrolled loading frame. Axial stress was imposed by a piston in the loading column and controlled by a Hewlett Packard 203A function generator. Cyclic loads were prescribed from continuous sine functions at single frequencies ranging from 0.01 Hz to 100 Hz. Three axial LVDTs are used to measure strain. The LVDTs are set 120 degrees apart from another and held to the sample with fixed rings. The experimental and sample configurations are shown in Figure 7. The three LVDT strain measurements are collected on separate channels, then averaged. If the strains vary outside 10% from another, the LVDTs are repositioned and the experiment is repeated (assuming the sample is isotropic).

The sample was initially loaded to 10 bars, then cycled approximately 0.5 bar around the 10 bar preload. This load was chosen to minimize mechanical losses across interfaces in the loading column. The experimental procedure is duplicated for an aluminum core with the same dimensions to calibrate the hysteresis of the experimental system.

Data Acquisition and Processing

Data were collected digitally at a sample resolution up to 50 microseconds. In particular, this minimum time step is necessary to resolve small phase shifts on the order of 5 milliradians and to adequately sample the 100 Hz cycles. The voltages from the load cell and three LVDTs are collected via an A to D card set in a PC. The modulus and Q were determined from different techniques depending on the frequency of the sinusoidal load. For frequencies below 5 Hz, the modulus and Q were determined from single loops, with 1400 points of data per cycle. For frequencies at and above 5 Hz, many cycles (up to 200) were collected and analyzed to compute the modulus and Q. The number of points per cycle decreased with increasing frequency. The signal noise level is handled by applying a Butterworth filter to the raw data, then compute stress and strain values. The filtered data is represented in Figure 8.

System Calibration

The energy losses of the system are critical in determining the modulus and Q of the sample of interest. The system includes the interfaces in the loading column, the mechanical features and responses in the loading frame and sample column, electronic filters which remove signal noise, and signal amplifiers. The system loss (phase angle) was determined by performing a duplicate experiment at each frequency and preload using a low loss aluminum reference sample. The system phase angle was then subtracted from the net phase angle measured for the sample of interest. The stress-strain hysteresis loop for aluminum measured at 0.5 Hz is shown in Figure 9. The data has
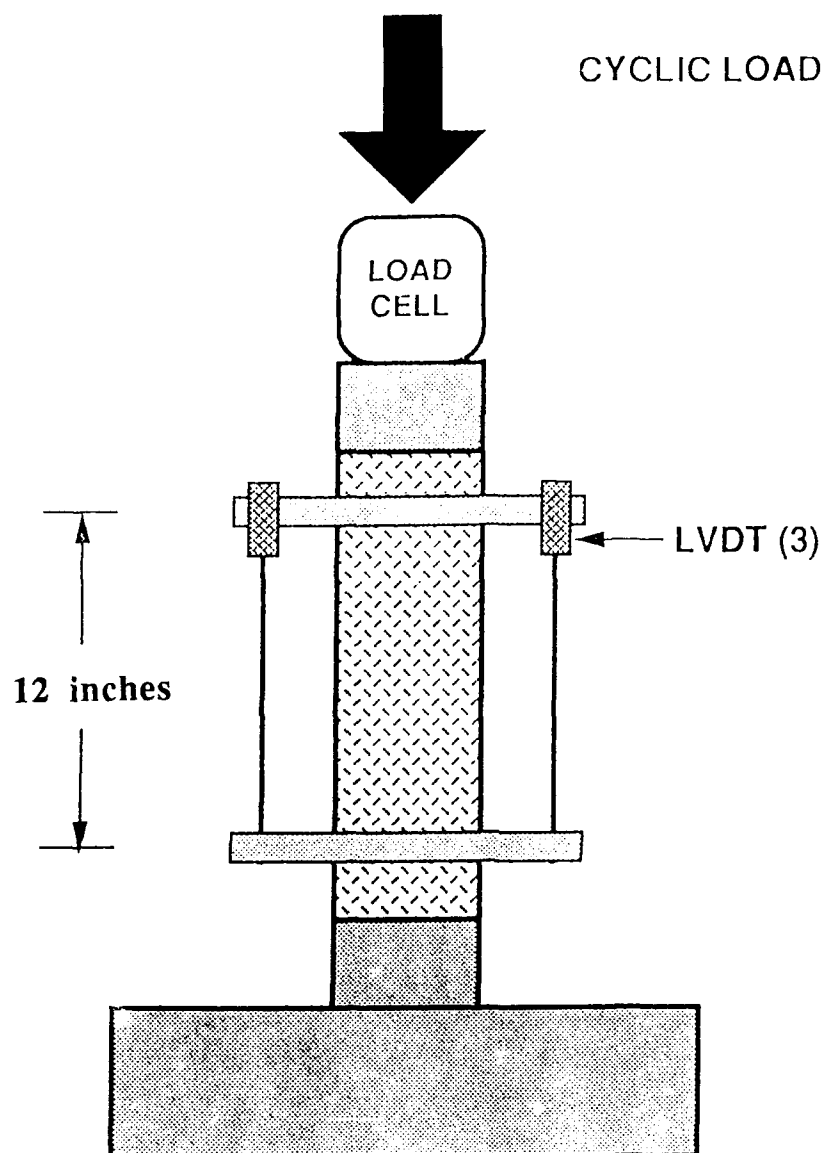
Figure 7. Schematic diagram of the experimental apparatus for low-frequency hysteresis loop modulus and attenuation measurements. The sample is mounted in a servo-controlled loading frame.
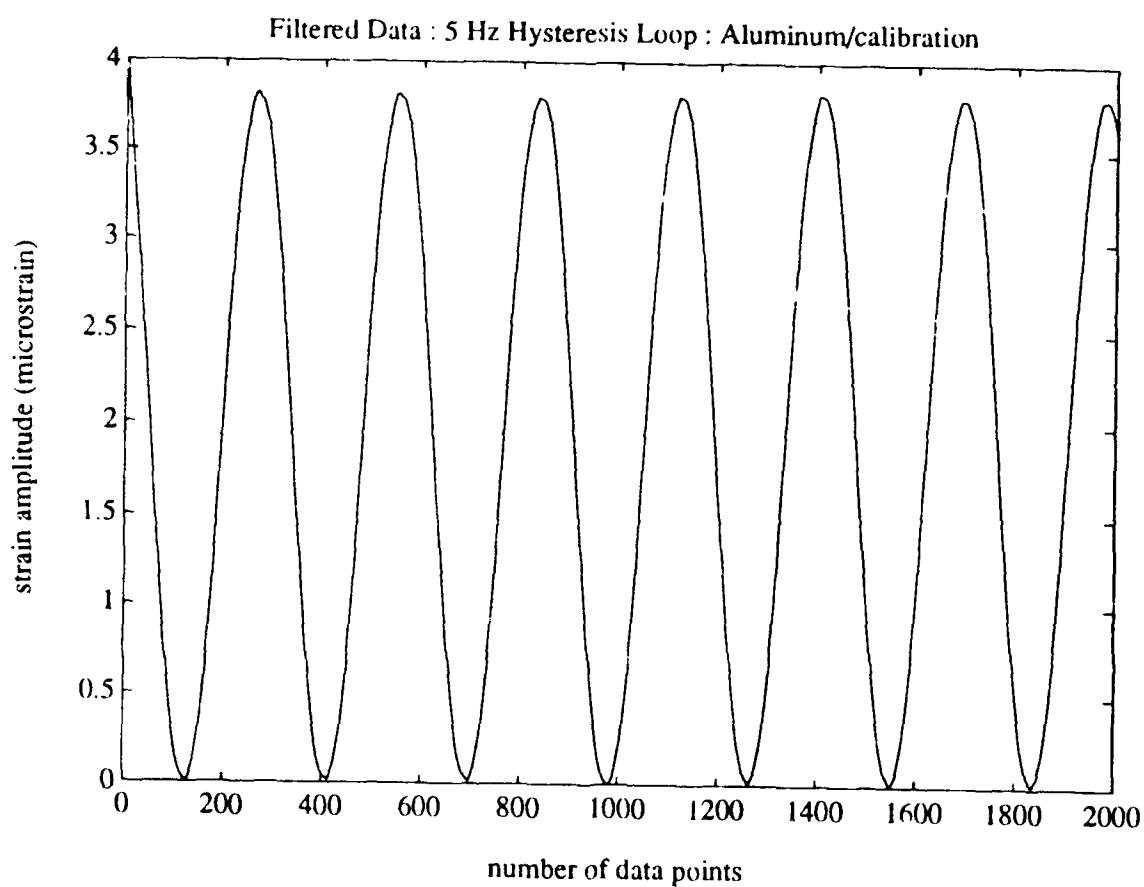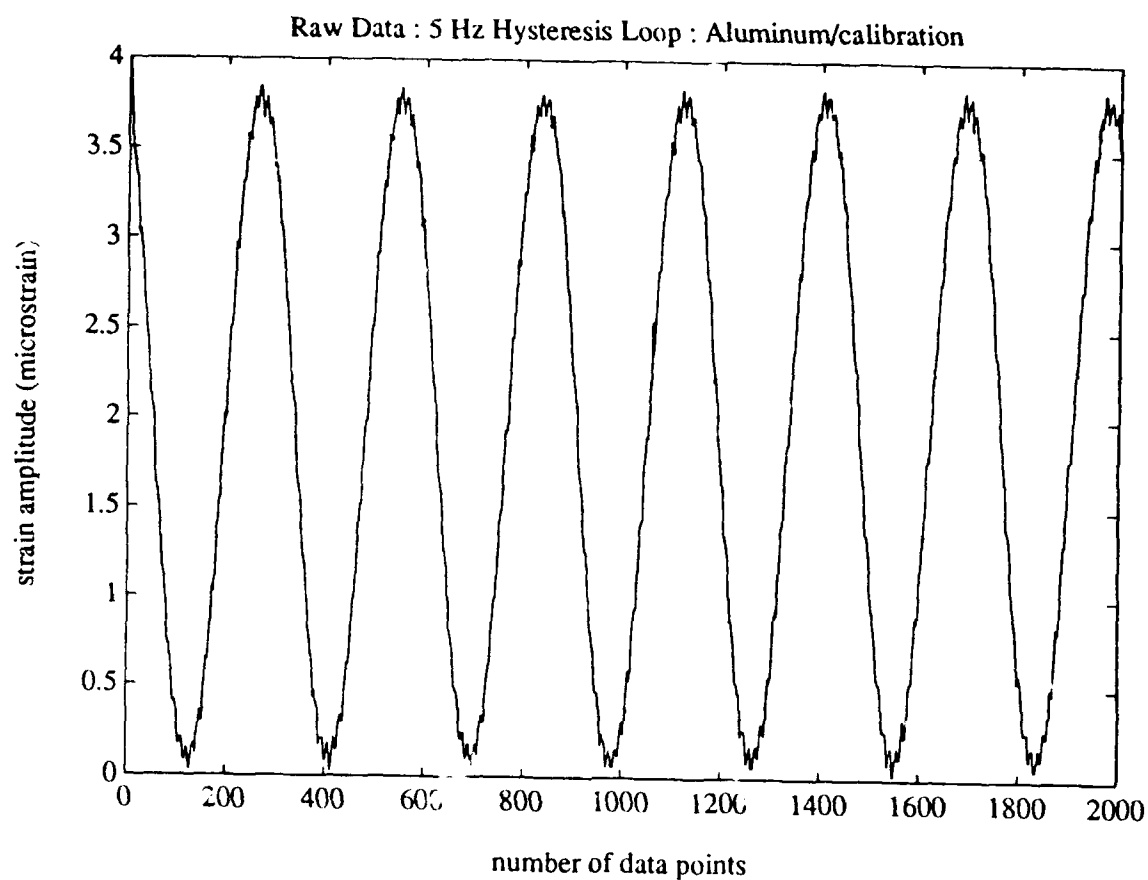
Raw Data : 5 Hz Hysteresis Loop : Aluminum/calibration

number of data points

Filtered Data : 5 Hz Hysteresis Loop : Aluminum/calibration

number of data points

FIGURE 8

36

been filtered to remove signal noise. The calibration phase angle is then subtracted from the phase angle of the rock phase angle as depicted in the bottom panel in Figure 10. Once the phase angle is computed, the Q value is determined from the tangent to that corrected angle.

Determining Young's Modulus

Below 5 Hz:

Young's modulus was determined from the slope of the line which bisects the averaged stress-strain loop at a single frequency. The 5 Hz hysteresis loop for the aluminum calibration is shown in Figure 9. The dotted line is a plot of the measured data (including system hysteresis).

At and Above 5 Hz:

Complex Young's modulus was determined by computing the Fast Fourier Transforms of the stress and strain sinusoids. The amplitude spectra for stress and strain are shown in Figure 10. The complex modulus was next computed from the ratio of the peak stress and strain spectra at the input frequency. The modulus amplitude was then calculated from the complex modulus and compared with moduli at lower frequencies. As the frequency was increased above 10 Hz, an apparent increase in Young's modulus was observed. Since the modulus of aluminum is independent of frequency below 100 Hz (Spencer, 1981), this increase was attributed to system losses. It was assumed that the strain amplitude was under estimated above 10 Hz. A correction factor was required to process the data to obtain Young's modulus. To account for the amplitude loss, a scaling factor was computed and applied to the apparent modulus. First, the apparent modulus of aluminum was fitted with a polynomial as a function of frequency from 0.01 to 100 Hz. The modulus fit for aluminum is constant at frequencies below 10 Hz. The scaling factor was then computed from the polynomial by reducing the aluminum signal loss to the constant value below 10 Hz. The scaling factor was then applied to the rock data.
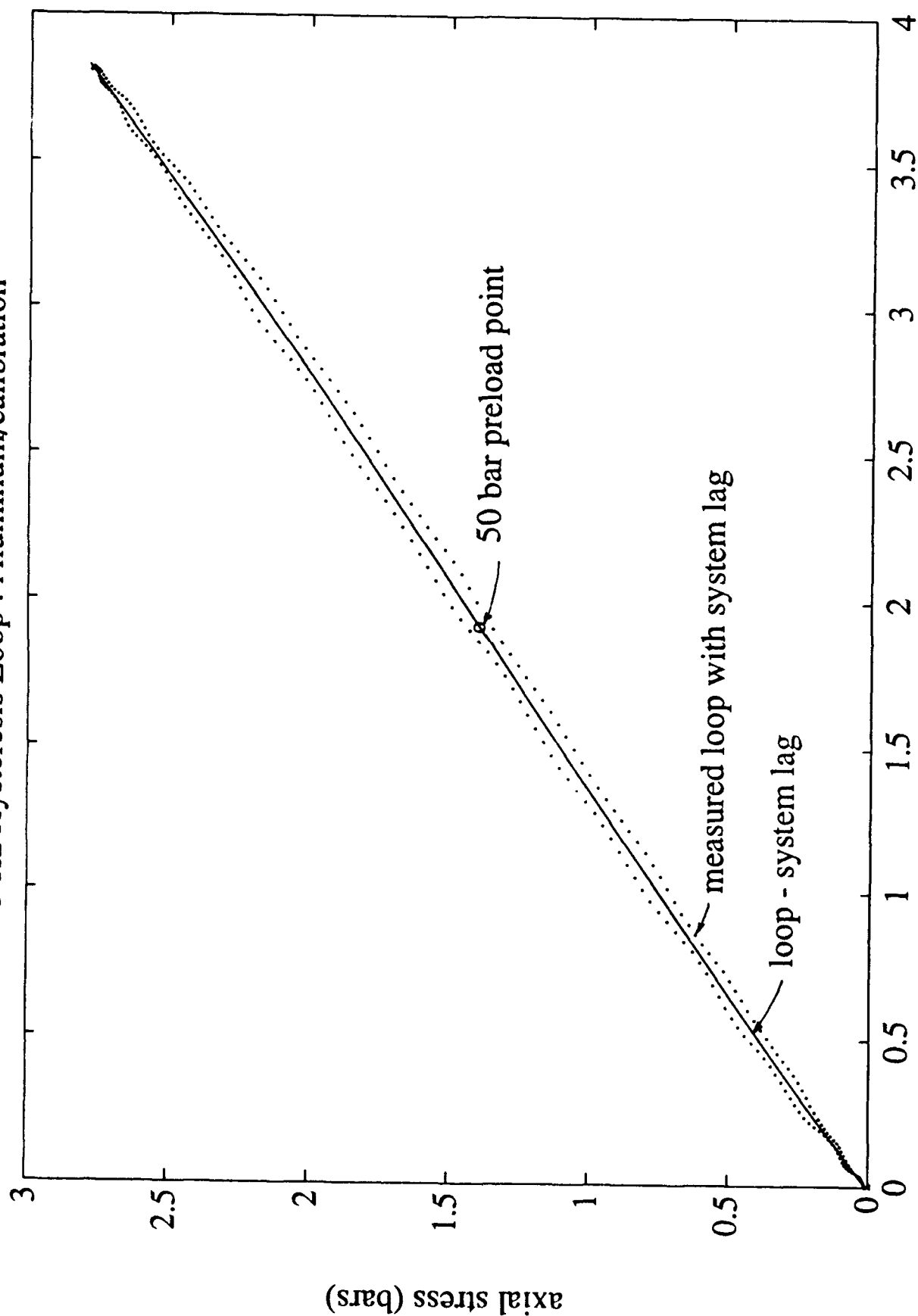
Determining Attenuation

Attenuation was determined from the phase angle measured between the stress and strain sinusoids.

Below 5 Hz

Two sinusoidal signals of the same frequency can be compared to determine the phase shift in time. For example, there are 1400 points per cycle or period, T, in a single loop.

37

5 Hz Hysteresis Loop : Aluminum/calibration

axial stress (bars)

axial strain (microstrain)

50 bar preload point

measured loop with system lag

loop - system lag

FIGURE 9

38

Amplitude Spectra - Sierra White granite - 30 Hz cyclic load

— stress
-- strain

frequency (Hz)

amplitude
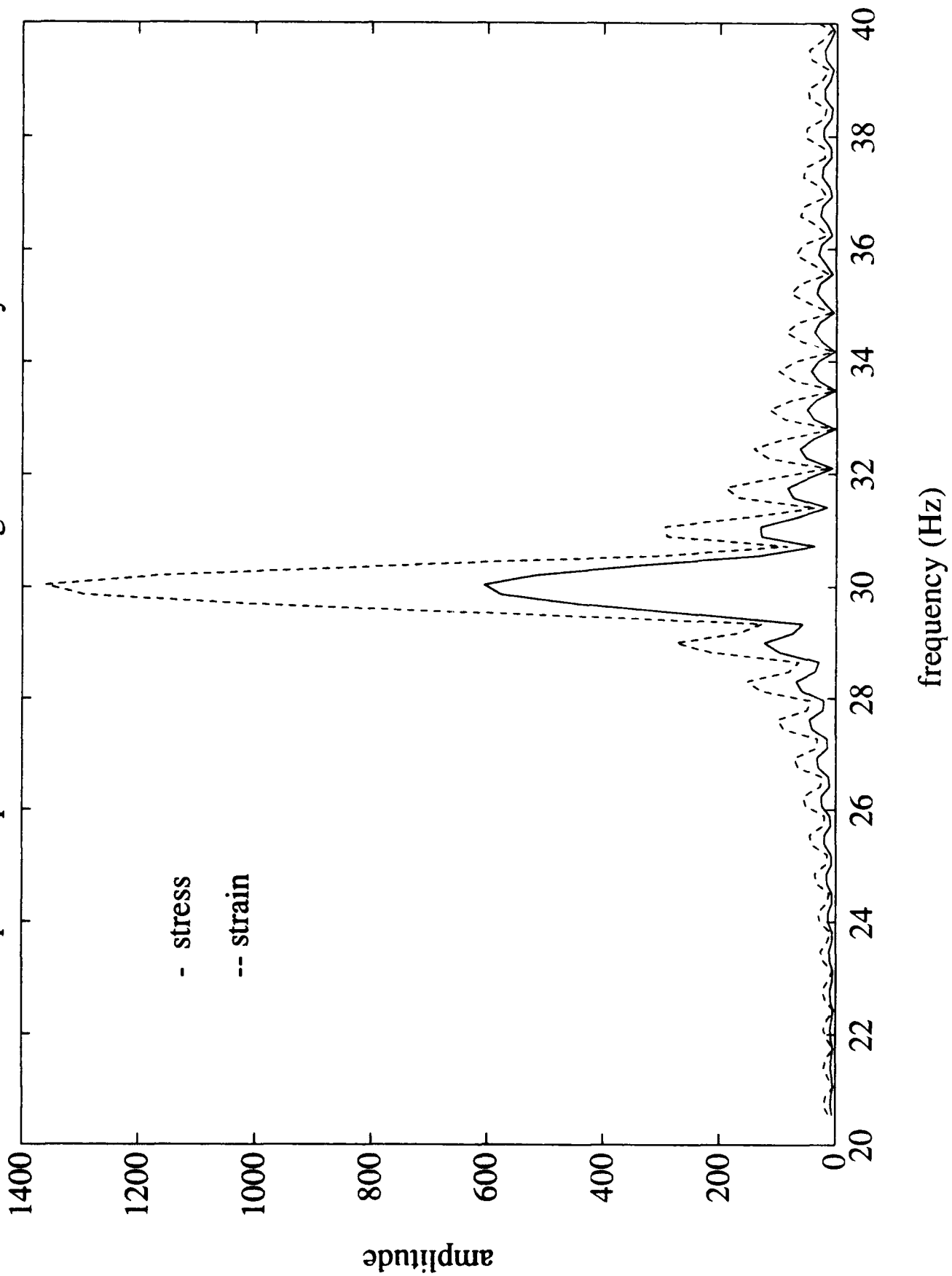
FIGURE 9

39

Berea sandstone (saturated) : Hysteresis Loop

0.1 Hz cyclic load
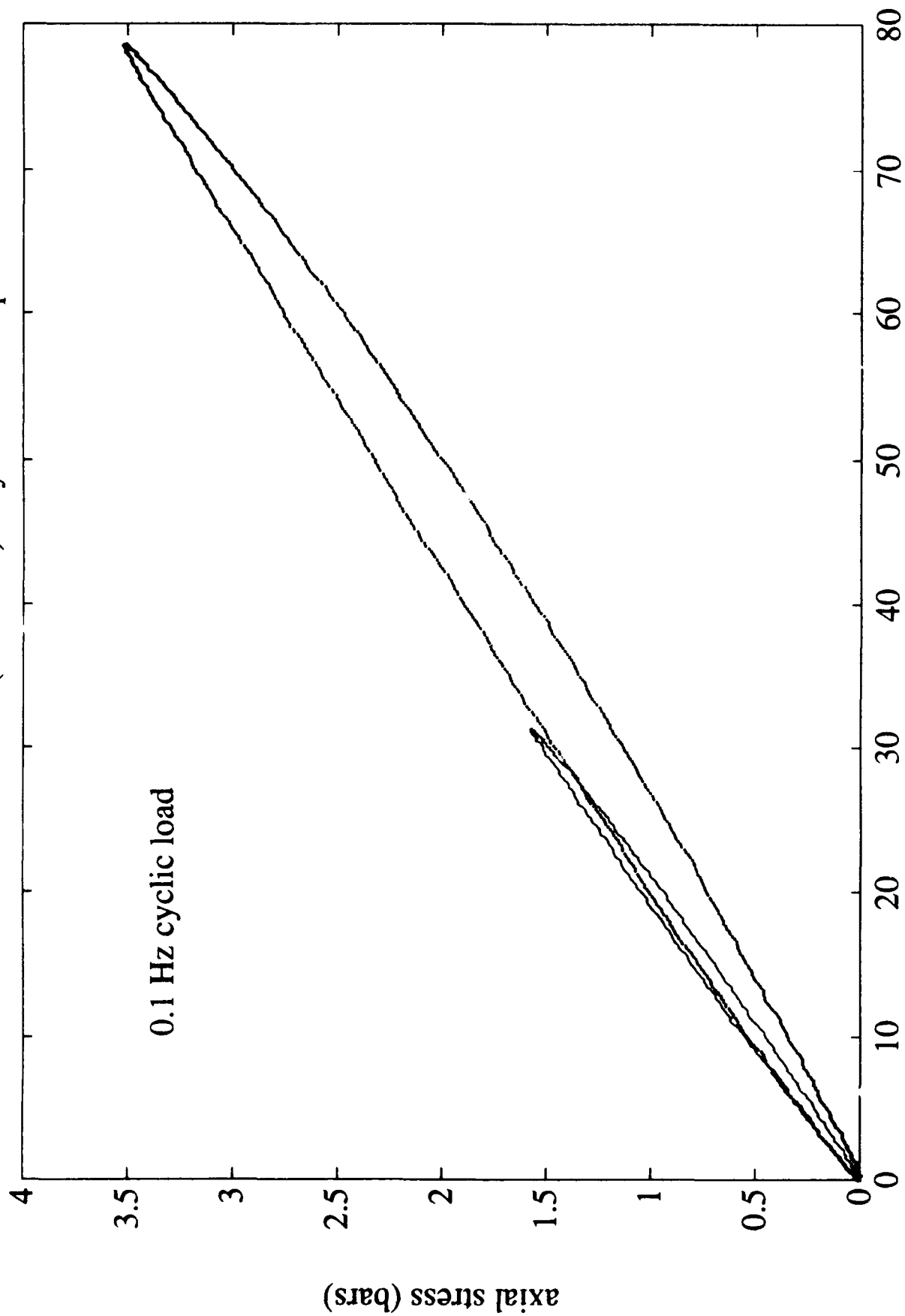
axial stress (bars)

axial strain (microstrain)

FIGURE 10

40

The phase shift is then the difference in the number of points, Δn for the maximum stress and strain. The phase in radians is:

$$\phi = 2\pi \Delta n / T$$

The phase angle and Q_E^{-1} were also computed from the area of the hysteresis loop for comparison purposes. The error was within 7%.

At or above 5 Hz

Q_E^{-1} was determined directly from the complex Young's modulus by computing the ratio of the imaginary and real modulus components. The system attenuation increased with frequency above 10 Hz. The calibration phase angle for the system was determined at each frequency point and subtracted from the measured sample phase angle (sample + system).

APPENDIX B

RESONANT BAR EXPERIMENTS

RESONANT BAR EXPERIMENTS

Benchtop resonant bar experiments were conducted on cylindrical or square rods of rock specimen. The samples were cored from a 12" cubic block and ground to this shape with the ends flat and parallel to within 0.001 inches. Two identical, 0.25 inch diameter, 1 MHz, compressional, PZT, piezoelectric crystals were epoxied to the sample using Epotek 301 epoxy, with one crystal arbitrarily designated as the excitation source and the second as the sensing receiver. During the epoxy cure schedule a small load was applied to the crystals with a small screw-driven loading frame and a stiff spring. After curing, number 38 gauge wires were tightly coiled and soldered to the piezoelectric crystal chrome-gold electrodes.

Crystals epoxied to the sample ends were used to drive the sample in extensional (also referred to as longitudinal) mode. The crystals epoxied to the sample ends were also used to measure a mixed compressional wave/bar velocity in an ultrasonic pulse experiment.

Resonant bar experiments were conducted in a modified dessicator bell-jar that isolated the sample in a controlled atmosphere. The sample was supported at its midpoint with a thin, cotton string suspended from a fixture. The coiled leads from the piezoelectric crystals were clasped with spring-loaded test hooks. The leads from these test hooks were brought out of the chamber through a sealed fitting and into coaxial connectors. A lock-in amplifier was used to resonate the rod at the fundamental resonances and at higher harmonics, up to the 18th harmonic for the extensional resonance of the dry sample. The corrected fundamental extensional resonance was approximately 6.0 kHz. Both source and sensing piezoelectric crystals were wired to the amplifier, one to the reference sine wave output and the second to the differential amplifier input. The differential amplifier input from the sensing crystal was able to "lock-in" to the phase shifted sine wave frequency being used to resonate the rod. A PC-controlled D/A converter was used to externally control the lock-in amplifier reference sine wave output to sweep through the entire frequency band of interest, and an A/D input was used to measure the amplified signal from the sensing crystal.

Computation of Velocity, Modulus, and Attenuation

Extensional velocity, Young's modulus, and extentional wave attenuation are determined from the half-power width frequency band, where F is the resonant or center frequency. A correction is applied to the measurement accounting for the effects of the crystal mass and sample jacketing. F corr is the value of the resonant frequency after it is corrected for the effect of end loading by the piezoelectric crystals. The correction used is from Lucet and others (1991):

Berea sandstone : Resonant Bar

Amplitude
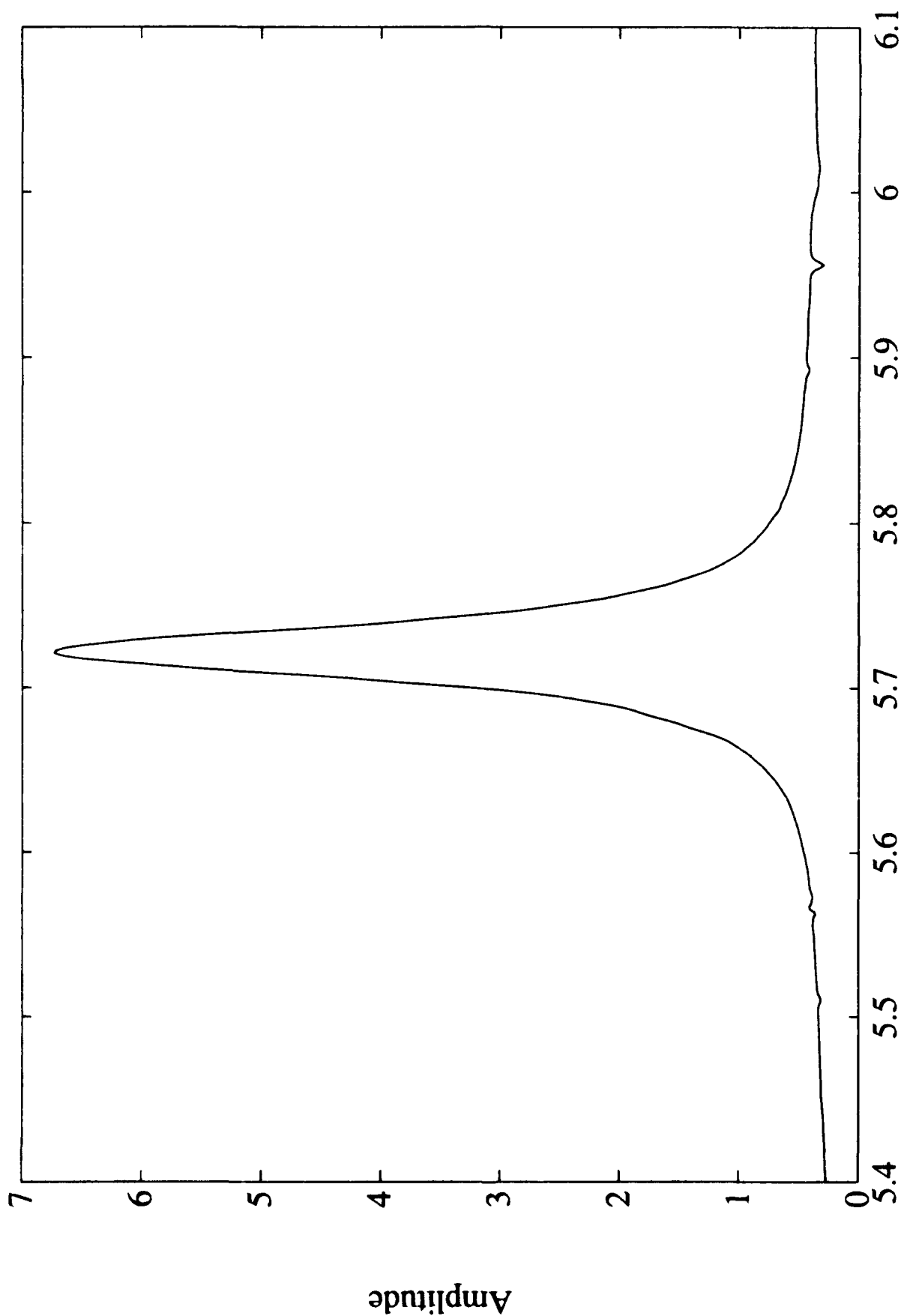
Frequency (kHz)

FIGURE 11

44

$$F_{corr} = \frac{F_{meas}}{1 - \alpha}$$

$$\alpha = \frac{M_{crystals}}{M_{bar}}$$

where F_{meas} is the measured frequency and $M_{crystals}$ is the mass of the piezoelectric crystals and M_{bar} is the mass of the bar without the piezoelectric crystals.

Q is the quality factor, ΔF is the frequency half power band width:

$$Q = \frac{F_{corr}}{\Delta F}$$

Ve is the extensional velocity in m/s.

$$V_e = F_{corr} \, l \left(\frac{2}{peak} \right)$$

where l is the length of the bar in meters and 2/peak corrects for the wavelength of the resonant frequency. For example, the fundamental is one-half wavelength, so the length of the bar needs to be doubled to get the correct velocity.

E is the Young's Modulus in GPa.

$$E = V_e^2 \rho$$

where ρ is the density in kg/m^3. For the flexural measurements,

$$V_s = F_{corr} \, l \left(\frac{2}{peak} \right)$$

$$G = V_s^2 \rho$$

For the measurements made on samples wrapped in teflon tape, the data was corrected using the technique of Lucet and others (1991). First, Fcorr was calculated and Ve was determined from it. This corrects for the end-loading of the sample. Next the Ve was corrected for the effect of the jacketing using the equation:

45

$$V_{e\,corr} = V_e \sqrt{\left[\frac{M_{wrapped\,sample}}{M_{unwrapped\,sample}} \right]}$$

where Ve is the calculated Ve from the Fcorr. Then, a new center frequency was calculated using the relation

$$F_{corr\,new} = \frac{V_{e\,corr}\left(\frac{peak}{2}\right)}{1}$$

An error of less than 5% can be associated with the attenuations and moduli from the resonant bar experiment.

Table 1 contains results of extensional resonant bar measurements on the room dry specimen of Berea sandstone sample. The measured center frequencies have been corrected using the procedure of Lucet and others (1991). The measured frequency was corrected by dividing by 1-α, where α is the ratio of the mass of the crystals epoxied to the sample to the mass of the sample. For a crystal mass of 1.139 g and a bar mass of 34.045 g, α is 0.0335. In the table are columns of corrected center resonant frequency, the harmonic of the resonance, the velocity in km/s, Young's modulus in GPa, and extensional quality factor Q_e.

TABLE 1

Attenuation Measurements in Berea sandstone Bar Utilizing the Resonant Bar Technique.

CORRECTED FREQUENCY (Hz)	HARMONIC	VELOCITY (km/s)	YOUNG'S MODULUS (GPa)	QUALITY FACTOR (Q_e)
6064	0	2.176	10.41	160
12220	1	2.193	10.56	153
17895	2	2.141	10.07	157
23955	3	2.149	10.15	150
30164	4	2.165	10.30	201
36229	5	2.167	10.32	148
42290	6	2.168	10.33	143
47668	7	2.139	10.05	139
53883	8	2.149	10.15	139
60287	9	2.164	10.29	143
65500	10	2.137	10.03	136
72240	11	2.161	10.26	136
78634	12	2.171	10.35	146
84174	13	2.158	10.23	114
89637	14	2.145	10.11	102
95447	15	2.141	10.07	132
101330	16	2.139	10.05	90
107545	17	2.144	10.10	117
111449	18	2.105	9.74	109

Attenuation Measurements without Confining Pressure

The first experiments of Tittmann and others (1972) were performed using an extensional-mode excitation at room-temperature and pressure. The lunar samples were cut into long thin bars. Then a small tab of iron was glued onto each end of the bar. One end was driven electromagnetically and the electromagnetic response of the system was measured at the other end. Tittmann and others (1972) found that a room-dry lunar basalt (Sample 14310) yielded a Q_E of approximately 90. The same sample, when exposed to hot water vapor for thirty seconds, yielded a Q_E of approximately 10. Longer exposure to hot water vapor produced a Q so low that it could not be measured. When a vacuum of 5 x 10^{-8} Torr was applied, Q_E was found to increase to between 130 and 150. A Q_E of approximately 800 was obtained under simultaneous exposure to a vacuum of 5 x 10^{-8} Torr and temperature of -180°C.

These experiments were followed by further extensional-mode experiments (Tittmann et al, 1974) that documented higher Q values with more extensive outgassing procedures. A lunar basalt (Sample W-8) was outgassed to 2x10^{-8} Torr at room temperature and a Q_E of 688 was obtained at a resonant frequency of 15,531 Hz. The sample was then heated to 200°C at 10^{-8} Torr to further outgas it. It was cooled and then exposed to N_2-enriched air for about two hours. This produced a Q_E of 1478 at a resonant frequency of 15,335 Hz. The sample was again heated to 200°C at 10^{-8} Torr and allowed to cool under a 10^{-8} Torr vacuum to room temperature. Under a 10^{-8} Torr vacuum, a Q_E of 1890 was measured two hours after the heat treatment; a Q_E of 2010 was measured five and one-half hours after the heat treatment. Both measurements had a resonant frequency of 15,294 Hz. The changes in Q_E were found to be reversible; reexposing the sample to laboratory air lowered the Q_E to approximately 100. The changes in Q_E were attributed to the presence of H_2O in the sample.

Another set of extensional measurements (Tittmann et al, 1975) was carried out in a new vacuum chamber. The new chamber was constructed from stainless steel and was designed to allow a better vacuum to be attained in the system. Experiments on a lunar basalt (Sample 70215,85) in the new chamber yielded the following results. A Q_E of 60 at a resonant frequency of 19,969 Hz was obtained at laboratory temperature and pressure. The sample was then placed in the vacuum chamber and a pressure of 10^{-3} Torr was established. A Q_E of 340 at 20,335 Hz was obtained. The first of three heating cycles to 300°C at 10^{-3} Torr produced a Q_E of 400 at 20,353 Hz. The new two cycles produced a Q_E of 800 at 20,253 Hz. A fourth heating cycle to 200°C was followed by lowering the pressure to 10^{-6} Torr. This produced a Q_E of 2420 at 20,138 Hz. Continued pumping, for one week, further reduced the pressure to 10^{-7} Torr and yielded a Q_E of 3130. A Q_E of 142 at 20,154 Hz was obtained after long term reexposure to laboratory air.

Measurements of Attenuation under Confining Pressure

Tittmann and others (1976,1977) began a program to measure attenuation in outgassed samples as a function of confining pressure. In order to make these measurements, a system utilizing torsional resonance was developed, in order to prevent attenuation due to coupling between the sample and the confining pressure medium. They also developed a system that allowed rock samples to be cased in thin-walled copper tubing under a vacuum of 1×10^{-5} Torr. This allowed measurements to be obtained on outgassed samples. These experiments on terrestrial basalts (Tittmann et al, 1977) documented large differences in Q_T between vacuum-outgassed samples and samples with 0.04 and 2.0% H_2O. As before, the outgassed samples had a Q that was substantially higher than the wet samples. The variation of Q_T with pressure seems to depend on the porosity of the sample. A terrestrial basalt with 10% porosity had a Q_T that increased as a function of pressure from 0 to 1 kbar. Two samples of terrestrial basalt with a porosity of 1% had Q_T's that increased up to about 50-100 bars; then Q_T remained constant or decreased as the pressure was increased.

Tittmann and others (1978) developed a system for measuring Q_E under confining pressure. They rounded the end-plugs used to jacket the samples in an effort to produce an aerodynamic shape that would interact as little as possible with the confining pressure fluid. Using this technique, they measured Q_E under confining pressure for an outgassed terrestrial basalt with 1% porosity. They found that Q_E behaved similarly to Q_T for the low porosity basalt (Tittmann et al, 1977). Q_E was high and decreased slightly as confining pressure was increased.

Tittmann and others (1979) measured Q_E as a function of temperature and pressure on a terrestrial basalt that had been outgassed and encapsulated at 1×10^{-6} Torr. The measurement was designed to simulate conditions along the lunar selenotherm. As the confining pressure was increased from 0.25 kbar to 1.25 kbar and the temperature was simultaneously increased from 20°C to 120 °C, Q_E was found to increase from approximately 800 to near 1400. They concluded that these values were consistent with the high Q obtained for the lunar crust using seismic observations and that the high lunar Q was due to the extremely dry condition of the lunar crust.

Temperature Dependence of Attenuation

Tittmann and others (1976) conducted a series of experiments on the temperature dependence of the Q of terrestrial basalts to determine if Q was changed to a higher value by welding of the grains at high temperature. A torsional mode experiment was conducted near 55 Hz using temperatures from 25°C to 600°C under a 10^{-7} Torr vacuum. The heating/cooling rate was near 60°C/hour. The Q_T increased from 500 to 920 at room temperature after the heating cycle, but the resonant frequency returned to nearly its original value. The small hysteresis in

Q_T was thought to be due to the relatively fast heating/cooling rate. Two extensional mode experiments were conducted under a vacuum at frequencies between 15 kHz and 17 kHz and temperatures between -40°C and 170°C. The heating/cooling rates were 30°C/hour and 1°C/hour. For the 30°C heating/cooling rate, the resonant frequency increased from about 15.4 kHz at 25°C to about 16.3 kHz at 150°C. For the 1°C heating/cooling rate, the resonant frequency increased from about 15.6 kHz at -40°C to about 17.6 kHz at 170°C. In both cases the resonant frequency returned to its original value on cooling. The lack of hysteresis in the resonant frequency for all three experiments indicates that there was no permanent change in the elastic moduli. Therefore, Tittmann and others concluded that no permanent welding of the grains had occurred. They suggested that the increase in the elastic moduli may be due to a thermally-induced partial closing of microcracks in the rock.

Tittmann and others (1978) measured the temperature dependence of Q using the torsional method. Their results are given below. For an outgassed terrestrial basalt, Q_T decreased as temperature increased from -100°C to 100°C. Then Q_T began to increase from 150°C to 450°C.

Temperature	Q_T
-100	1670
-50	1430
0	1330
50	800
100	620
150	700
250	900
350	950
450	900

Tittmann and others (1979) conducted a series of thermal cracking experiments on Westerly Granite in order to determine the relative importance of thermal cracking versus adsorbed water content. In this set of experiments, the sample was heated to the required temperature at less than 2°C/minute under vacuum. It was then cooled to room temperature, backfilled with dry nitrogen gas and iron driving tabs were attached. The sample was placed into the torsional apparatus and a vacuum was reestablished. The resonant frequency was found to decrease smoothly from about 14 kHz at 0°C to 8 kHz at 480°C; then a large downward shift occurred between 500°C and 600°C and the resonant frequency again decreased smoothly from 4.2 kHz at 600°C to 3.8 kHz at 750°C. Q_T was found to constantly increase from about 400 to 1400 over the same range of temperature. Tittmann and others (1979) attributed the drop in resonant frequency between 500°C and 600°C to the α–β phase transition in quartz. They concluded that high degrees of thermal cracking are not inconsistent with high Q when the sample is dry.

50

Effect of Volatiles at Room Pressure

Tittmann and others (1975) also conducted a detailed set of experiments to determine what effect different volatiles would have on the Q. The experiment consisted of placing a terrestrial basalt sample into the chamber and outgassing it until the Q was approximately 500. Then the sample was exposed to 1 atm of the volatile of interest and the Q was measured. They reported the results of these experiments as percent decrease from the original Q. I have recalculated their figures to a Q value assuming the original outgassed Q is always 500.

Gas	Q
He	485
CO_2	460
O_2	425
H_2	375
H	300
CO	275

With the exception of helium, all the gases caused a reduction in Q. Tittmann and others (1975) suggest that the adsorption of gas is responsible for the decrease in Q.

The test chamber was attached to a gas-source mass spectrometer to analyze the residual gas that remained after outgassing the sample. The dominant gases that remained in the chamber were H_2O and either CO or N_2 Tittmann and others (1975) suggested that it was primarily the presence of H_2O that prevented the achievement of higher Q values in the outgassed terrestrial basalt.

Tittmann and others (1976) also continued their systematic study of the effect of different volatiles on the Q of a terrestrial basalt. The procedure involved outgassing the sample at 400°C and 10^{-8} Torr and then allowing 1 atm of the gas to equilibrate with the sample. The results were again reported as a percent reduction in Q. I have recalculated their figures to a Q value assuming the original outgassed Q is always 735. These values are reported below.

Gas	Q	Viscosity (cP)	Partial Pressure (mm Hg)	Boiling Point (°C)	Dipole Moment (Debye)
N_2	691	-	760	-198.5	0
Trichloroethylene	441	1.20	68	86.7	0.9
Benzene	419	0.62	90.8	80.1	0
Dichloromethane	390	0.42	382	40.7	1.60
Freon 14	672	0.97	760	-130	0
H_2O	294	0.89	21.1	100.0	1.82

Any reduction of Q due to the viscosity of the condensed liquid is masked by other effects, since liquid trichloroethylene has a viscosity larger than liquid dichloromethane; yet the reduction in Q due to trichloroethylene is less than dichloromethane. Dichloromethane has a vapor pressure that is larger than trichloroethylene. Both dichloromethane and trichloroethylene, like water, have a non-zero dipole moment. The dipole moment of dichloroethylene is larger than trichloroethylene. Tittmann and others (1976) report that the changes in Q are completely reversible; the original high Q can be restored by a bake-out under vacuum. They concluded that the reduction in Q is due to an absorption mechanism.

Tittmann and others (1979) measured the dependence of Q on the partial pressure of water in a terrestrial basalt. They constructed a chamber in which the partial pressure of water could be controlled. The sample was placed in the chamber and Q was measured for a range of partial pressures from 0 to 0.8. The weight of the sample was continually monitored. Even at a partial pressure of 0.72, the sample did not absorb more than 0.2 mg of H_2O per gram of rock. The Q decreased from 1450 to 950 over this range. A similar effect was observed for methanol over a range of partial pressures from 0 to 0.9. The Q did not decrease monotonically over this range. Tittmann and others (1979) noted two regimes in which the behavior of Q was different. They attributed the change in behavior of Q as reflecting a region, at low partial pressures, where water or methanol was adsorbed onto grain surfaces and a region, at high partial pressures, where water or methanol condensed in capillary space between grains.

Attenuation in crystalline rocks

Gordon and Davis (1968) measured the attenuation of a variety of crystalline rocks using the resonant bar technique. They used a composite piezoelectric resonator comprised of a rock sample glued to a quartz crystal to measure the extensional attenuation. They measured the attenuation at 90 kHz at a variety of strain amplitudes. Below, I have compiled their data on dry samples at a strain amplitudes between 2.3×10^{-7} and 3.0×10^{-7}. These samples were cleaned using pentane and alcohol and then placed under vacuum prior to being measured. The relatively high Q_E measured is consistent with Tittmann and others (1972, 1974, 1975, 1976, 1977, 1978, 1979) work on the attenuation of dry crystalline rock samples at similar strain amplitudes (10^{-8} range) (Tittmann, 1977)

Sample	Attenuation	Q_E
Single Quartz Crystal	5.37×10^{-5}	18622
Quartzite (15)	1.00×10^{-3}	1000
Dunite (28)	1.45×10^{-3}	690
Basalt (29)	3.31×10^{-3}	302
Pyroxenite (8)	3.80×10^{-3}	263

Basalt (25)	4.57×10^{-3}	219
Anorthosite (11)	5.89×10^{-3}	170
Granite (3)	1.38×10^{-3}	72
Diopsidite (33)	1.74×10^{-2}	57
Amphibolite (5)	2.04×10^{-2}	49
Quartzite (Q-2)	2.95×10^{-2}	34

It is not clear whether the large range in Q is due to intrinsic differences between the samples or it is the result of different, uncontrolled moisture content. The fact that samples of quartzite had both the highest and lowest Q's further complicates the analysis.

Gordon and Davis (1968) also measured Q_E in quartzite (sample 15) as a function of temperature.

Temperature (°C)	Attenuation	Q_E
30°	1.03×10^{-3}	970
41°	1.07×10^{-3}	935
60°	1.15×10^{-3}	870
80°	1.10×10^{-3}	910
100°	1.37×10^{-3}	730
151°	1.57×10^{-3}	637
199°	1.90×10^{-3}	526

These results are similar to those found by Tittmann and others (1978) using torsional resonance on an outgassed terrestrial basalt. In both experiments, Q decreased as a function of temperature up to 200°C. However, Gordon and Davis did not perform their experiment under vacuum like Tittmann and others. Note that some researchers (Toksoz and Johnston Q-book, Johnston and others, 1979) cite this experiment as demonstrating that Q is relatively constant as a function of temperature up to 150°C. It is important to note the relatively high values of Q found by Gordon and Davis (1968) at elevated temperatures, especially in light of the frequently held assertion that this experiment shows a decrease in Q due to thermal cracking of the sample at temperatures above 150°C. Any decrease in Q due to thermal cracking is evidently a small effect compared to the change to extremely low Q due to water-saturation.

Gordon and Davis (1968) also conducted an experiment comparing the effect of water-saturation on granite (sample 3). They measured Q before and after repeated cycles to high strain amplitude on both wet and dry samples.

Sample	Attenuation	Q_E
Dry Before	6.86×10^{-3}	146
Dry After	8.11×10^{-3}	123
Wet Before	5.87×10^{-2}	17
Wet After	7.11×10^{-2}	14

Gordon and Davis (1968) attributed the difference in the Q before and after the repeated cycles to high strain amplitude to sample fatigue. The large differences in Q between the wet and dry samples are again consistent with the work of Tittmann and others (1972, 1974, 1975, 1976, 1977, 1978, 1979).

Summary

These experiments on basalt and other crystalline rock indicate that the Q of a dry sample is highly dependent on the nature and amount of volatiles contained in the sample. The presence of water, even in minute amounts, is especially effective at reducing the Q. Q increases dramatically, in both lunar and terrestrial rocks, as the sample is outgassed under vacuum. Heating the sample under vacuum increases the amount of outgassing and causes further increases in Q. Backfilling the outgassed sample with anhydrous gases at atmospheric pressure can also reduce the Q, although not all are as effective as water vapor. The reduction in Q appears to be due to the adsorption of vapor on the grains within the sample. Even at high partial pressures of H_2O, the sample does not gain enough weight to be more than a few percent saturated. However, the identification of two regions of behavior of Q as a function of the partial pressure of H_2O suggests that the two attenuation mechanisms may exist.

The increase in Q of dry samples as temperature increases seems primarily to reflect the effect of outgassing the sample. Therefore, high degrees of thermal cracking are not inconsistent with high Q when the sample is dry. The effect of temperature on a fully-saturated sample have not been reported.

The effect of confining pressure on a dry sample varies, apparently depending on the porosity. However, the Q is very high for all reported measurements on dry samples under confining pressure. Here again, the Q appears to depend more strongly on the amount and type of vapor present than on the applied confining pressure.

APPENDIX C

WAVEFORM INVERSION TECHNIQUE

WAVEFORM INVERSION TECHNIQUE

The main purpose for measuring seismic wave attenuation in the laboratory is to infer the rock properties at in-situ scales and seismic frequencies. The pulse transmission technique (Toksoz et al, 1979) operates in the megahertz frequency range, while the resonant bar technique operates at sonic frequencies of a few kilohertz. It is desirable to measure attenuation in a range between sonic and ultrasonic frequencies. For this purpose, New England Research has designed a new technique that operates between 10 kHz and 150 kHz, depending on the sample dimensions.

The Technique:

The technique consists of measuring low-frequency waveforms using cylindrical bars of the same material but of different lengths. The bar is essentially a waveguide which allows the low-frequency fundamental mode to be propagated without having to use rock blocks of large sizes. The procedure of measuring attenuation consists of two major steps. In the first, the waveform received with the short bar is theoretically propagated to the distance of the long bar, in which the dispersion effect on the waveform due to the waveguide is removed. The second step is the inversion of attenuation ($1/Q_E$) or Q_E of the bar material through minimizing the difference between the propagated waveform and the actually measured waveform with the long bar. Since the waveform inversion is performed in the time domain, the waveforms can be appropriately truncated to avoid multiple reflections due to the finite size of the (short) sample, allowing attenuation to be measured at long wavelengths or low frequencies. For a detailed description of the technique and inversion formulation the reader is referred to the paper by Tang (1991).

Experimental Procedure

We used the waveform inversion technique to measure extensional Q_E for Berea Sandstone samples of different dimensions. The first set B-90-C, had diameters of 0.524 inches and lengths of 1.5 inches and 6.83 inches. The second group of samples are labeled as 7 inch and 16 inch; the diameters are 1.25 inches and the lengths are 7.177 inches and 15.70 inches. All the samples are room dry. The relative humity in lab was ~ 50%. During the measurement, the source and receiver transducers are mounted at the two ends of the bar sample and a signal generator is applied to drive the transducer at various frequencies. The waveforms are recorded with a digital oscilloscope.

Results

To illustrate the application of the technique, we show the comparison of inverted wavefrom from the short sample with the waveform measured from the large sample. Figure 1 shows the result at 10 kHz for the 1.25 inch diameter sample and Figure 2 shows the result at 80 kHz for the 0.524 inch diameter sample. The matches are very good. Furthermore, the Q_E values obtained from the two measurements of very different frequencies and sample sizes are fairly consistent (38.9 vs. 36.1), showing the constant Q_E behavior of the dry sample. Table 1 shows the inverted Q_E values for the two pairs of samples for the measured frequencies.

Table 1. Q_E Values From Waveform Inversion

Sample Set	Frequency (kHz)	Extensional Q_e
7" & 16" (1.25")	10	38.9
7" & 16" (1.25")	20	33.8
7" & 16" (1.25")	30	33.4
B-90-C (0.524")	60	34.6
B-90-C (0.524")	80	36.1

Future Directions

The waveform inversion technique can be easily adapted to measure attenuation under confining pressure appropriate to the in-situ condition, if the length of the pressure vessel is modified to accommodate the bar geometry and the low-frequency transducers are designed to operate under pressure. Temperature apparatus may also be added as necessary. Since the frequency of the waveforms is adjustable within a certain range, this technique can be used to measure Q_E as a function of frequency within this range. Furthermore, the waveforms of flextural and tortional modes in the bar can also be inverted to find the shear attenuation of the bar. This would be the direction of future research.
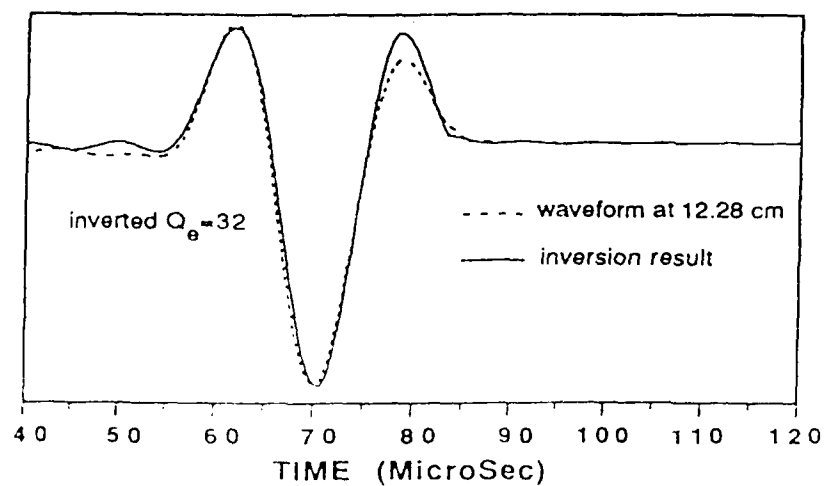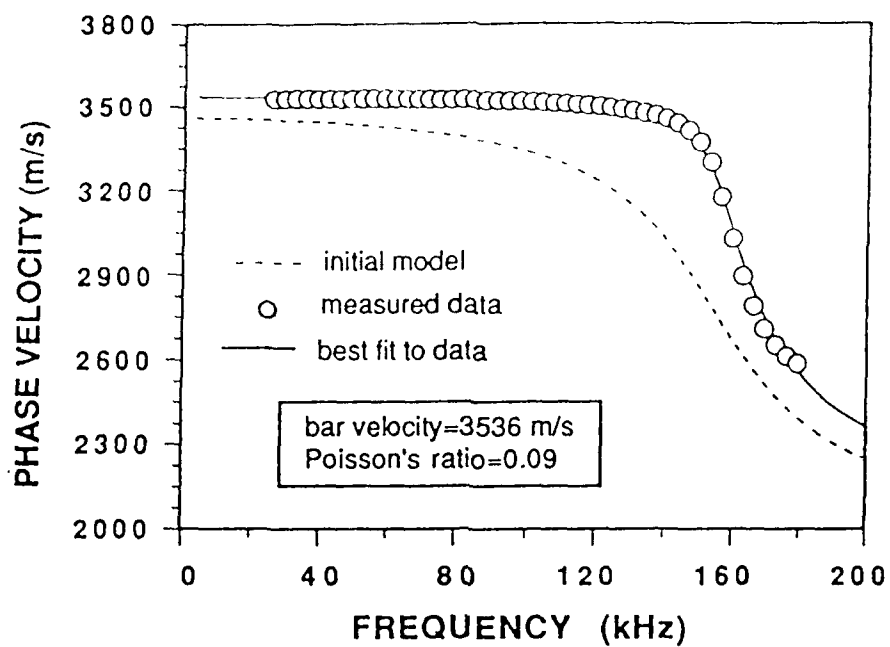
a.   **Waveforms Measured Within Berea Sandstone Bars**

b.

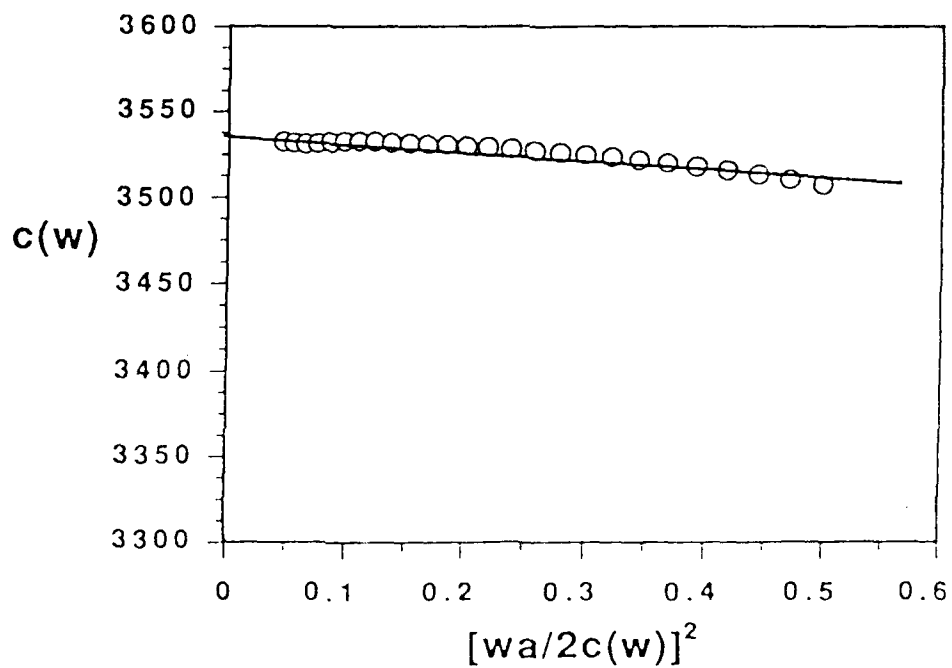FIGURE 12

58

a.

b.

FIGURE 13

59

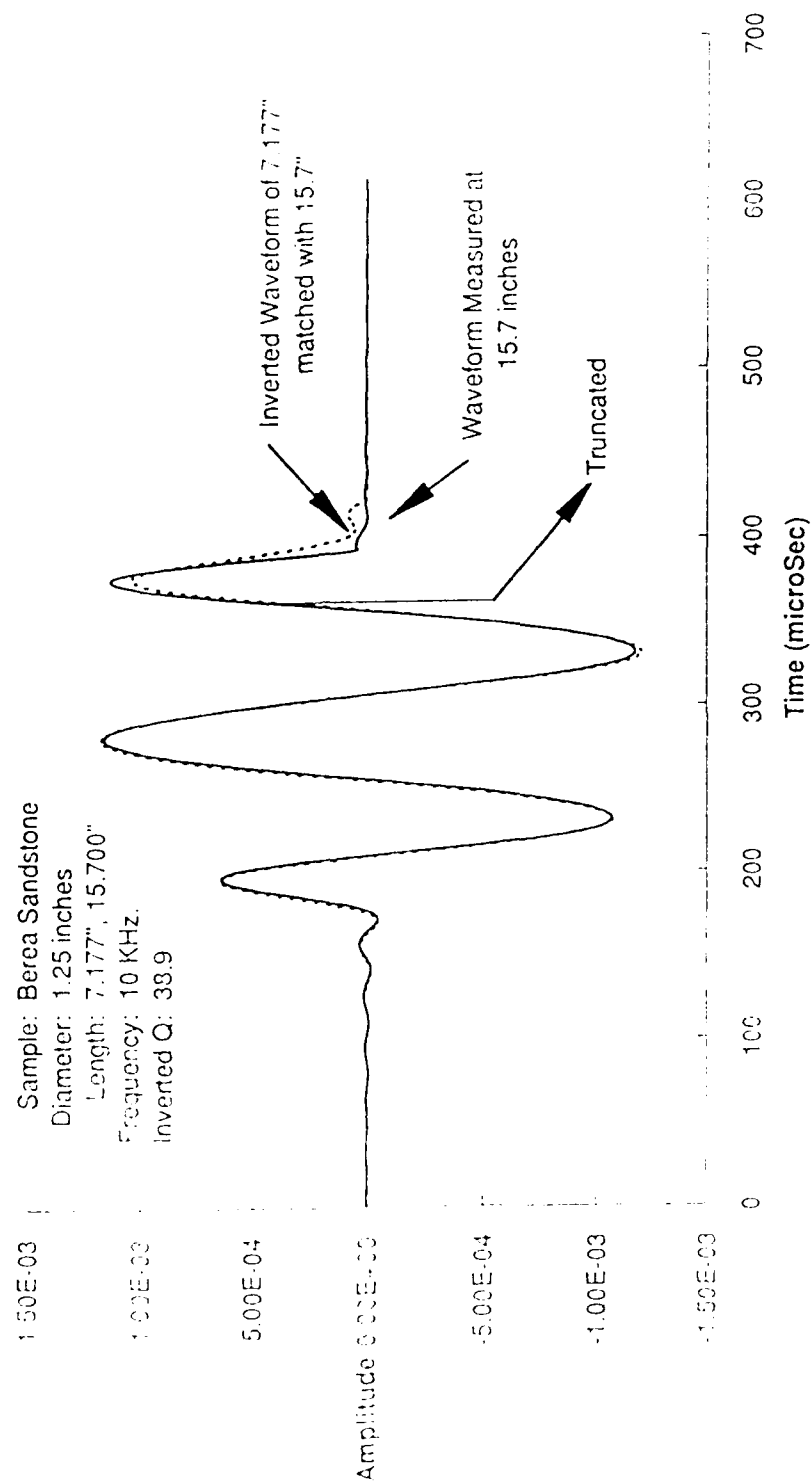Waveform Inversion Method for Measuring Attenuation Using Cylindrical Bars

Sample: Berea Sandstone
Diameter: 1.25 inches
Length: 7.177", 15.700"
Frequency: 10 KHz.
Inverted Q: 33.9

Inverted Waveform of 7.177"
matched with 15.7"

Waveform Measured at
15.7 inches

Truncated

Time (microSec)

FIGURE 14

60

Wavefrom Inversion Method for Measuring Attenuation Using Cylindrical Bars

Sample: Berea Sandstone
Diameter: 0.524 inches
Length: 1.5", 6.83"
Frequency: 80 KHz.
Inverted Q: 36.1

Inverted Waveform of 1.5"
matched with 6.83"

Waveform Measured
at 6.83 inches

Truncated

Time (microSec)

Amplitude

FIGURE 15

61

APPENDIX D

ULTRASONIC VELOCITY MEASUREMENT

ULTRASONIC VELOCITY MEASUREMENT

The compressional (P) and shear (S) wave velocities for the rock, at any stress condition, were obtained by measuring the one way travel time of a P or S wave through the core and dividing by the sample length. The wave propagation direction was parallel to the core axis. The ultrasonic transducer consisted of a piezoelectric source and receiver pair of like crystals (P or S) positioned at opposing ends of the cylindrical core. Only one crystal pair could be activated at a time. The source crystal was driven with a short electrical pulse (center frequency of 1 MHz) generated with a Panametrics 5055PR pulser-receiver.

The signal from the receiver crystal was amplified, high-pass filtered at 0.3 MHz, and displayed on a LeCroy 9400 digital oscilloscope. The travel time was measured on the oscilloscope screen with a cursor control marking the first break of the signal. The break was defined by a threshold voltage that was 1.25% of the peak-to-peak amplitude of the first three half-cycles of the signal. The arrival time was picked at the point when the threshold voltage was exceeded relative to the baseline voltage and had a resolution of ± 0.01 microsecond. The travel time of the wave through the end pieces is subtracted form the total time measured on the oscilloscope. The travel times of P and S wave propagation through the titanium end pieces or *zero times* were measured as a function of confining pressure by placing the end pieces head to head.

Well: BENCH TOP
Sample: CALIBRATION   Length:0.000 inch   Fluid: DRY
Conf Pr:79.00 psi   Pore Pr :0.00 psi   Temp :21.00 C
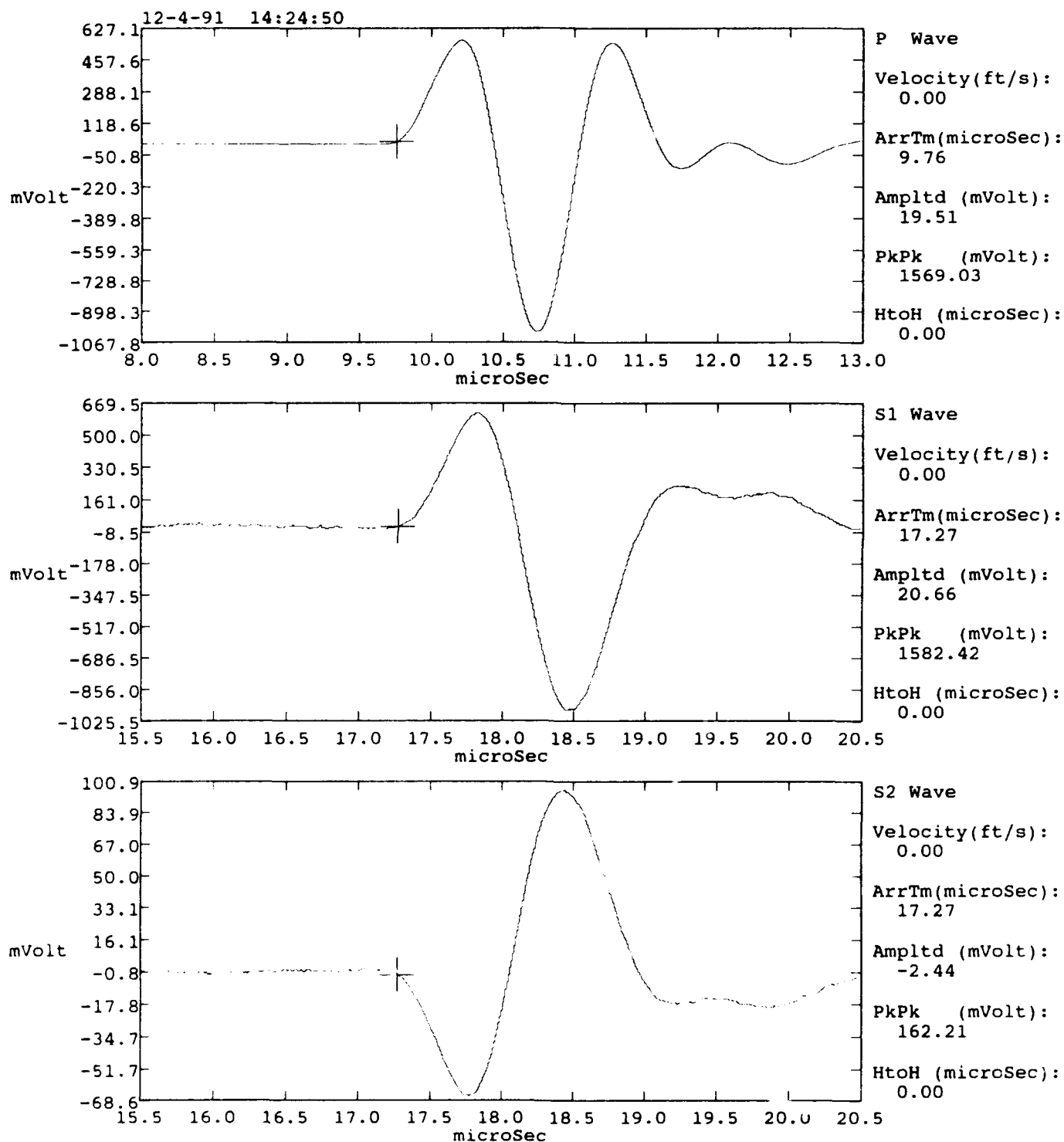File: BTHTH.1   Pick: Manual   12-4-91   14:24:50

12-4-91   14:24:50

P Wave

Velocity(ft/s):
 0.00

ArrTm(microSec):
 9.76

Ampltd (mVolt):
 19.51

PkPk   (mVolt):
 1569.03

HtoH (microSec):
 0.00

S1 Wave

Velocity(ft/s):
 0.00

ArrTm(microSec):
 17.27

Ampltd (mVolt):
 20.66

PkPk   (mVolt):
 1582.42

HtoH (microSec):
 0.00

S2 Wave

Velocity(ft/s):
 0.00

ArrTm(microSec):
 17.27

Ampltd (mVolt):
 -2.44

PkPk   (mVolt):
 162.21

HtoH (microSec):
 0.00

FIGURE 16

64

Well:
Sample: ALUMINUM   Length:1.019 inch   Fluid: DRY
Conf Pr:79.00 psi   Pore Pr :0.00 psi   Temp :21.00 C
File: ALUMINUM1.1   Pick: Manual   12-4-91   15:27:26
        OPERATOR= TIMOTHY HILL

FIGURE 17

65
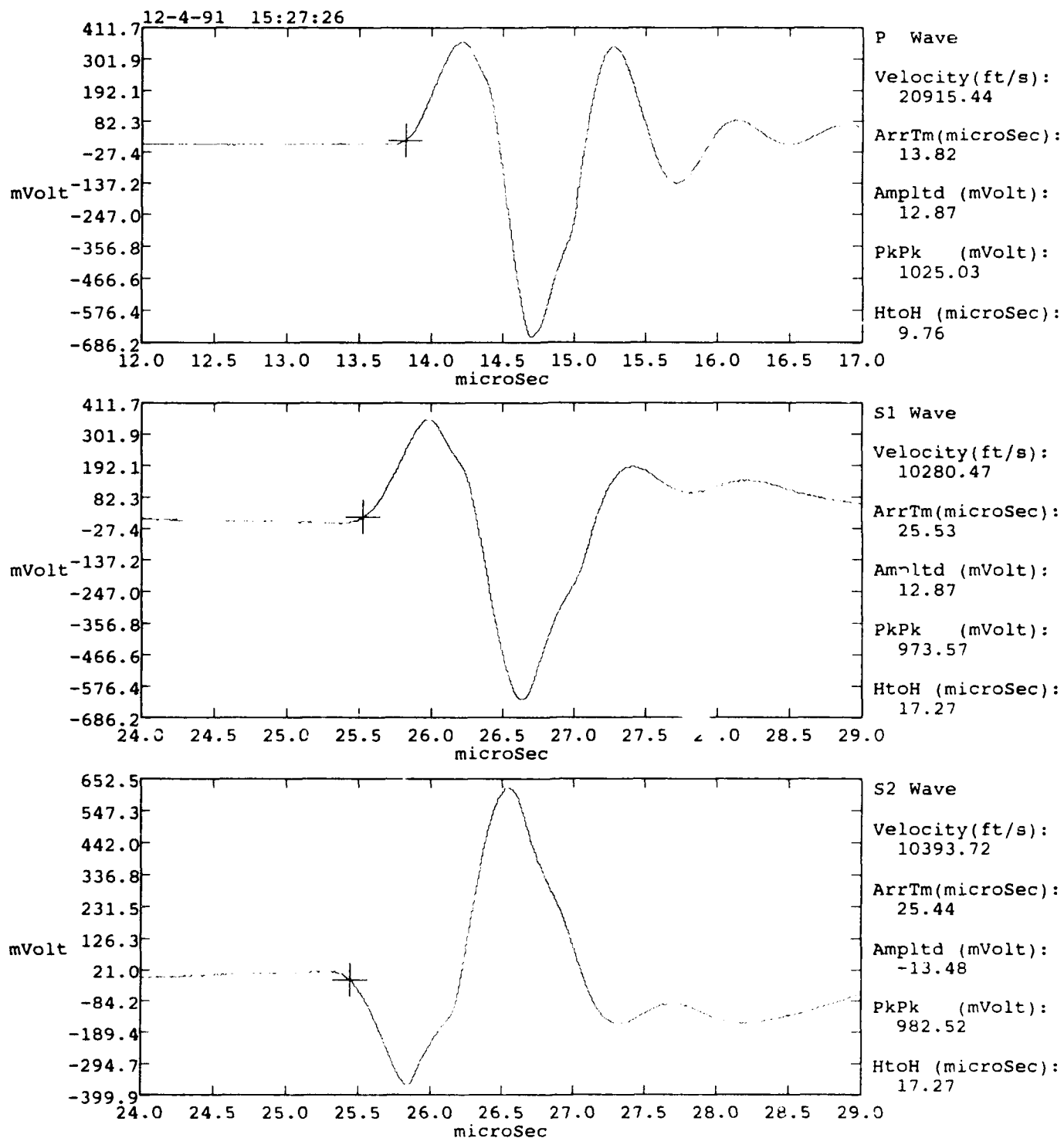
Well: SW-15A-90
Sample: GRANITE   Length:1.754 inch   Fluid: DRY
Conf Pr:80.00 psi   Pore Pr :0.00 psi   Temp :21.00 C
File: GRANITE.1D   Pick: Manual   12-16-91 12:18:16

FIGURE 18

66
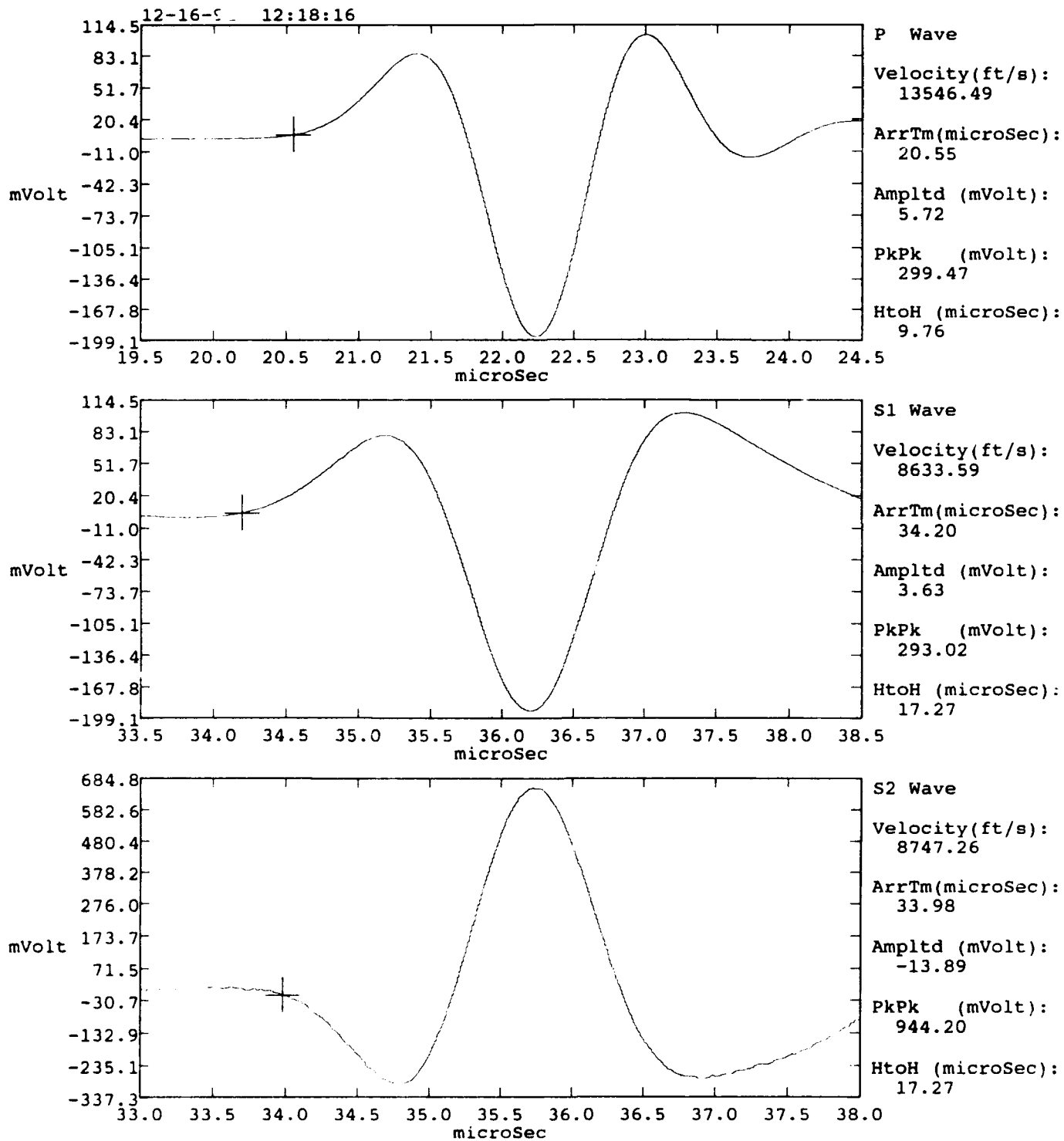
Well:
Sample: SIERRA WHITE   Length:1.013 inch   Fluid: DISTILLED WATER
Conf Pr:79.00 psi   Pore Pr :0.00 psi   Temp :21.00 C
File: SIERRA.1   Pick: Manual   12-6-91   17:15:12
          SATURATED IN DISTILLED WATER UNDER A VACCUM
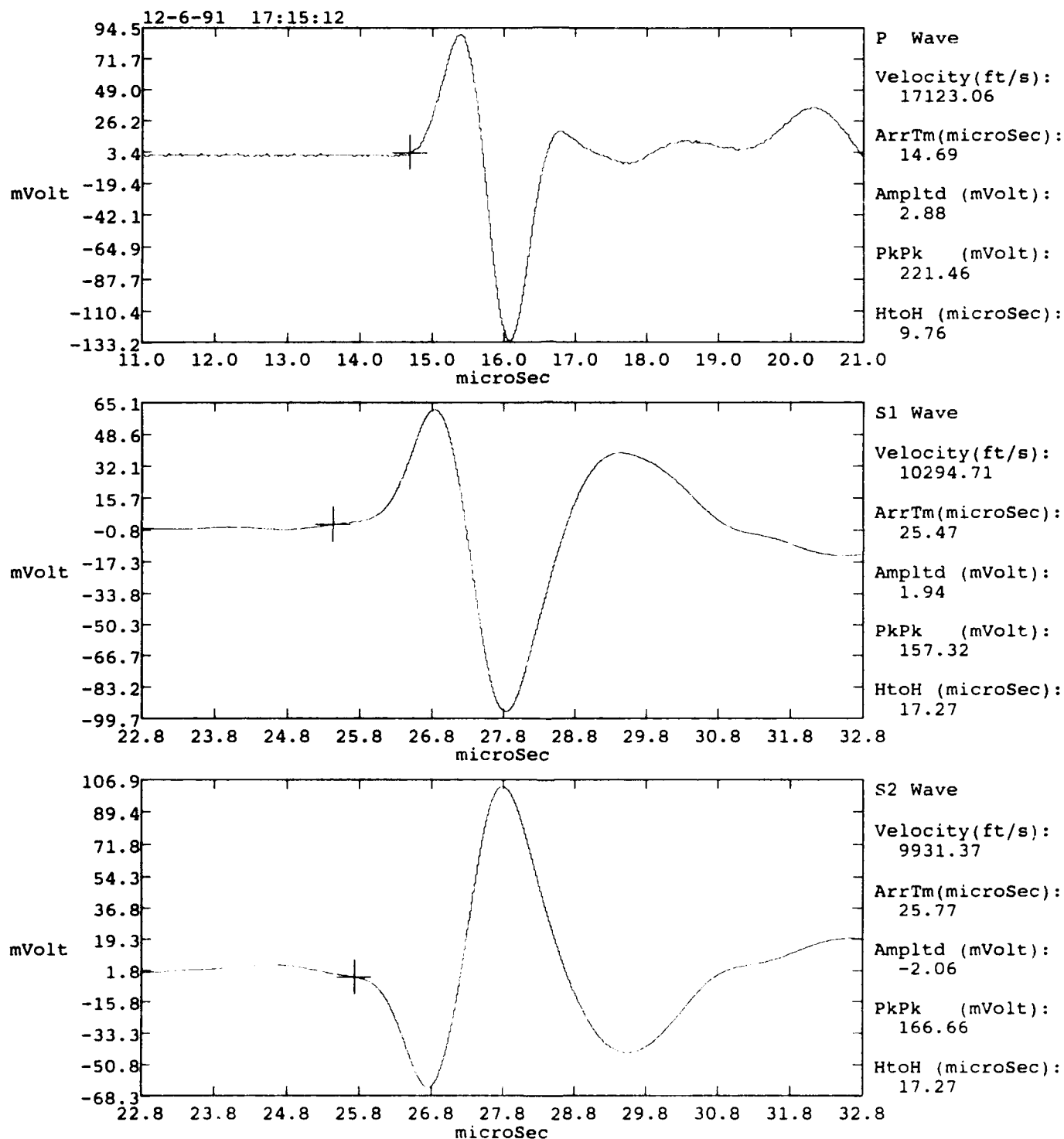
FIGURE 19
67

Well: BEREA SANDSTONE
Sample: BS/91/1-6/1 HP   Length:4.379 cm   Fluid: DRY
Conf Pr:20.00   Pore Pr :0.00   Temp :22.00 C
File: BS161HPD.4   Pick: Manual   7-31-91 7:49:0
ISR/ASTM rocks at · gh pressure with small diameter subsamples; Dry.
Orientation plane is parallel to polarization plane of S2.
7-31-91   7:49:0

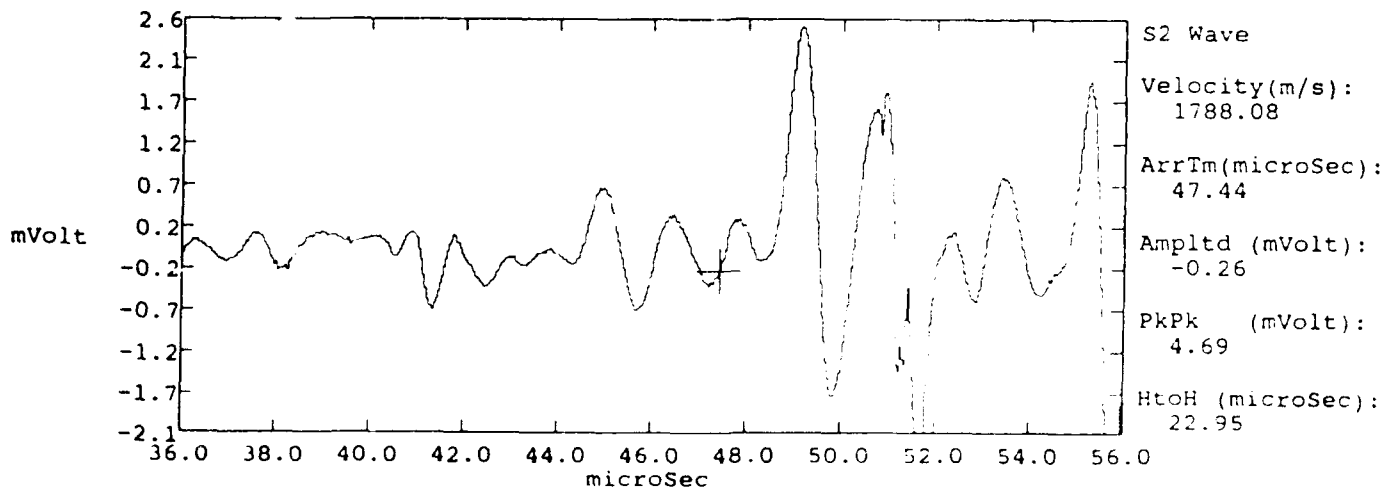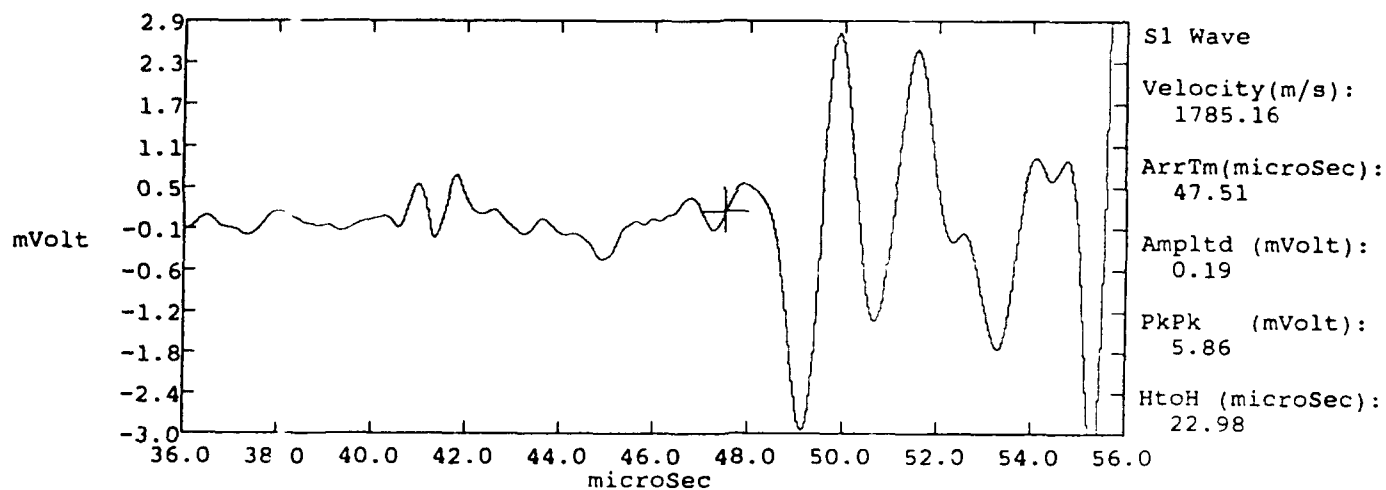FIGURE 20

68
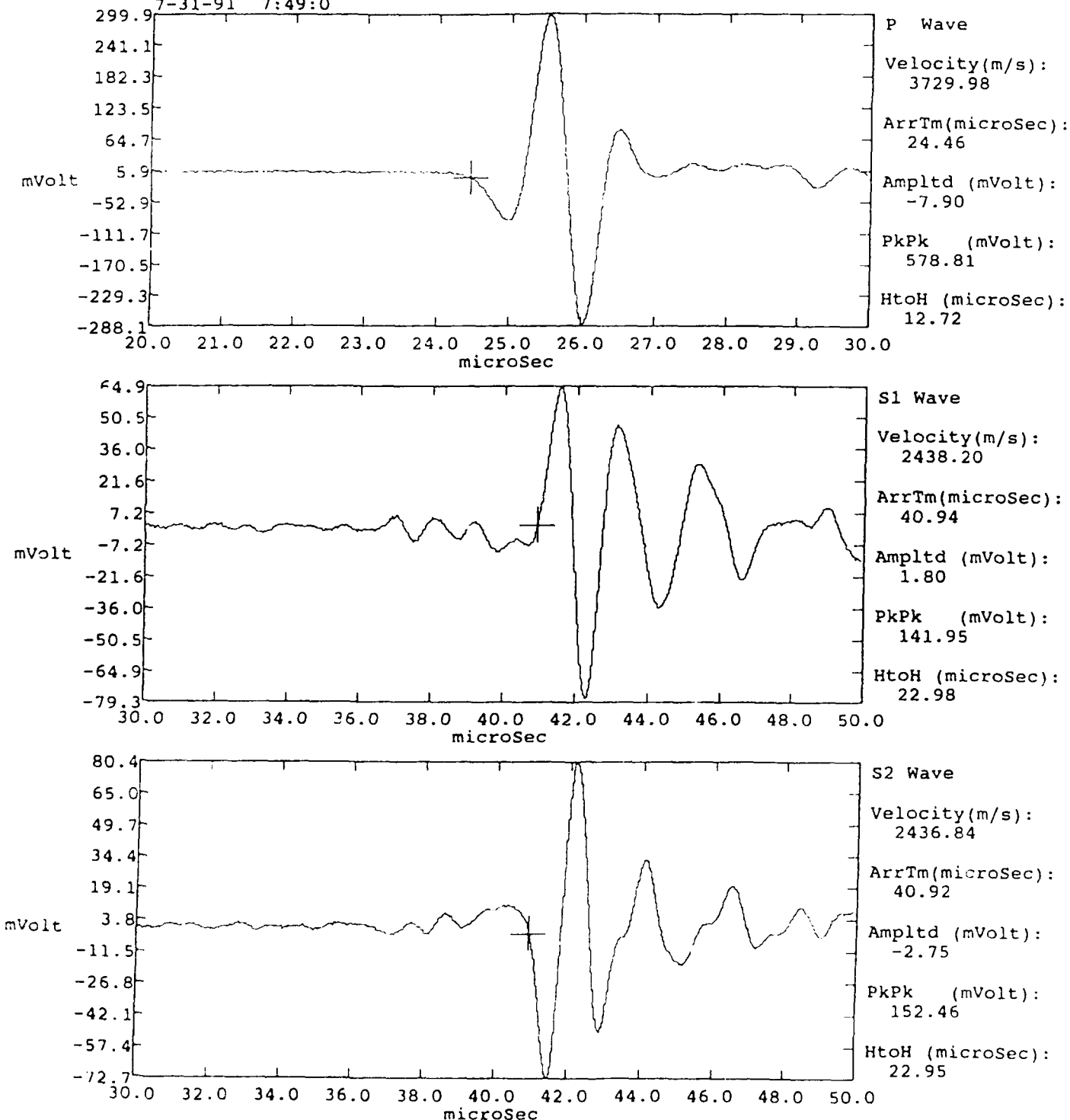
Well: BEREA SANDSTONE
Sample: BS/91/1-6/1 HP   Length:4.379 cm   Fluid: WATER
Conf Pr:1.00   Pore Pr :0.00   Temp :22.00 C
File: BS161HPS.1   Pick: Manual   8-1-91 9:30:16
ISR/ASTM rocks at high pressure w/ small diam. subsamples; Saturated.
Orientation plane is parallel to the polarization plane of S2.
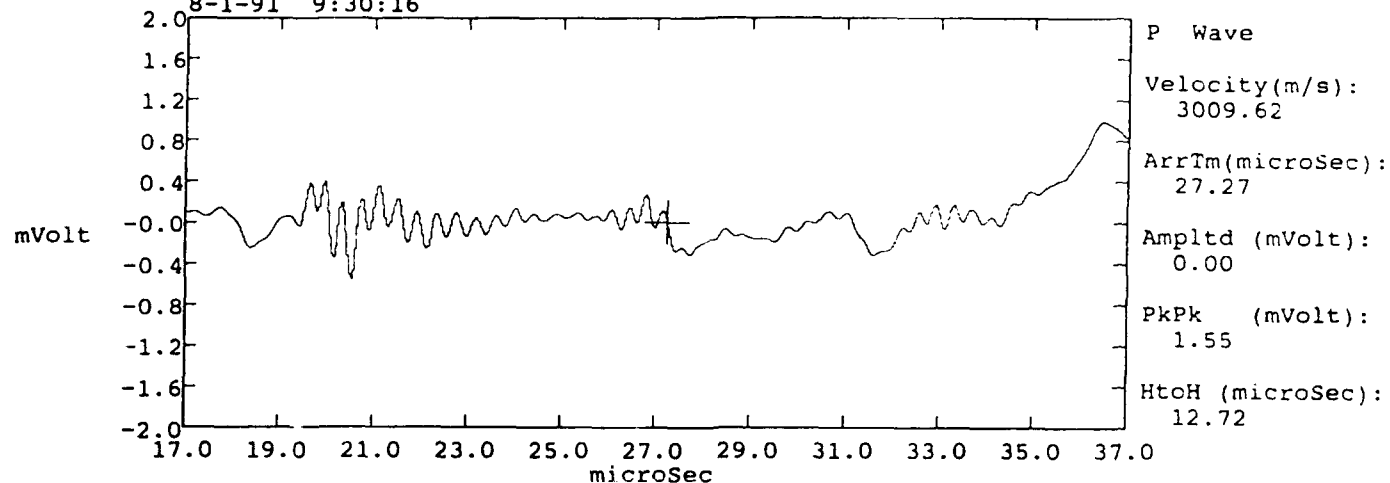8-1-91 9:30:16

P Wave

Velocity(m/s):
3009.62

ArrTm(microSec):
27.27

Ampltd (mVolt):
0.00

PkPk   (mVolt):
1.55

HtoH (microSec):
12.72

S1 Wave

Velocity(m/s):
1785.16

ArrTm(microSec):
47.51

Ampltd (mVolt):
0.19

PkPk   (mVolt):
5.86

HtoH (microSec):
22.98

S2 Wave

Velocity(m/s):
1788.08

ArrTm(microSec):
47.44

Ampltd (mVolt):
-0.26

PkPk   (mVolt):
4.69

HtoH (microSec):
22.95

FIGURE 21

69

ULTRASONIC Q AND PROCEDURE

Values of ultrasonic Q_E were determined for Sierra White granite and Berea sandstone in dry and saturated conditions during hydrostatic loading tests. Compressional and shear wave time series are collected for specific pressure increments for the rock and duplicated for a reference sample with a very high Q, such as aluminum. The Q value for alumium is approximately 150,000 (Toksoz et al, 1979). The value of Q at a given pressure can then be computed from the spectral ratio of the rock and aluminum. Moreover, in this technique, the extrinsic loss mechanisms of the transducer apparatus can be isolated and accounted for.

The procedure is as follows:

1) Time Series
The received times series through the rock and aluminum are edited for Fourier analysis in the following order:
1. DC value is first removed
2. Taper the signal end with a $\cos^2$ function to zero
3. Pad signal on front and end with zeroes (4096 total pts) for FFT

Unedited times series for Berea (dry) and aluminum are shown in Figure 1.

2) FFT
The Cooley-Tukey FFT is used to compute the spectrum of each time series and is the IEEE approved algorithm (Brenner, 1967).

3) Derivation and computation of Q
Q is derived from the spectra of the rock and aluminum signals in the following manor. The amplitude spectrum of the rock, R(f) and aluminum, A(f) are shown below:

$$A(f) = G_A(x)e^{-\alpha_A(f)x_A}e^{i(2\pi ft - k_A x_A)} \tag{1}$$

$$R(f) = G_R(x)e^{-\alpha_R(f)x_R}e^{i(2\pi ft - k_R x_R)} \tag{2}$$

where f is frequency, x is the sample length, k is the wave number, v is velocity, and α is the attenuation coefficient. G(x) is the geometrical factor which depicts the extrinsic loss mechanisms of the transducer and wave spreading. The subscript A and R refer to aluminum and rock, respectively. The wave number can be described in terms of frequency and velocity as:
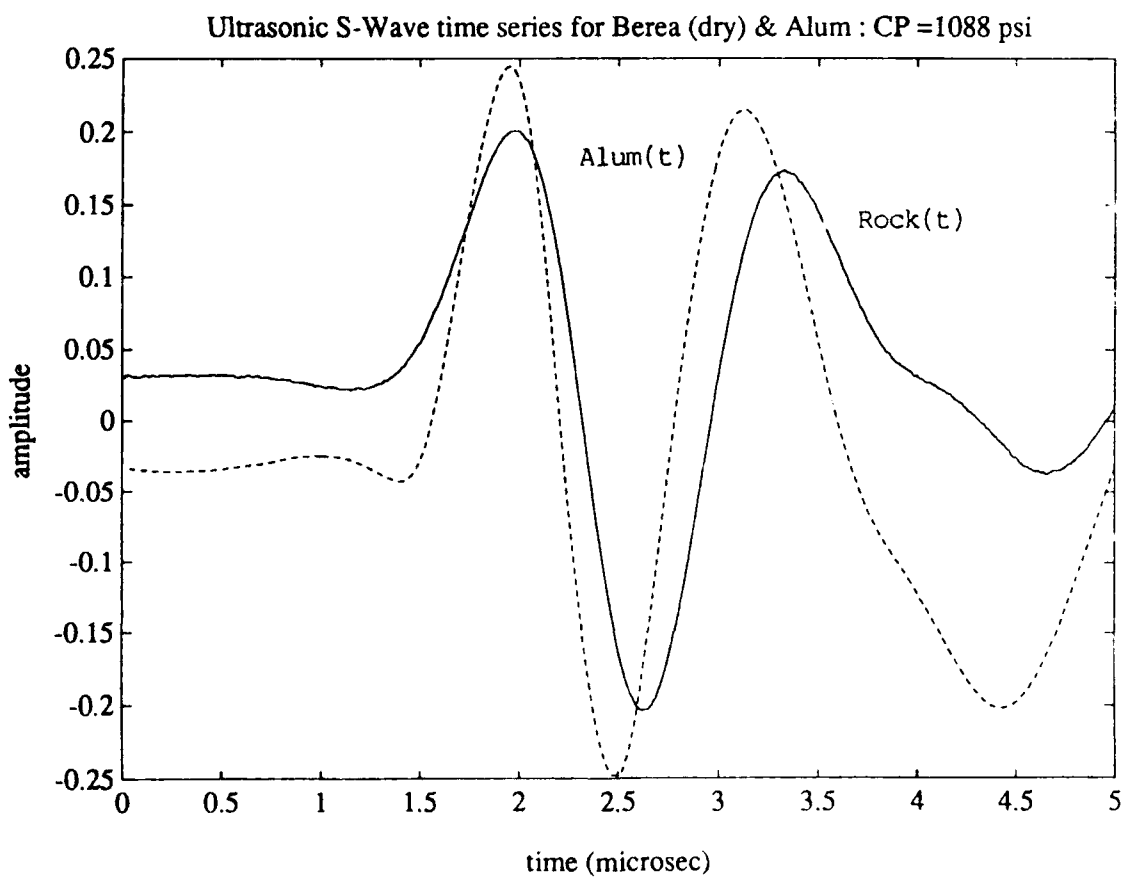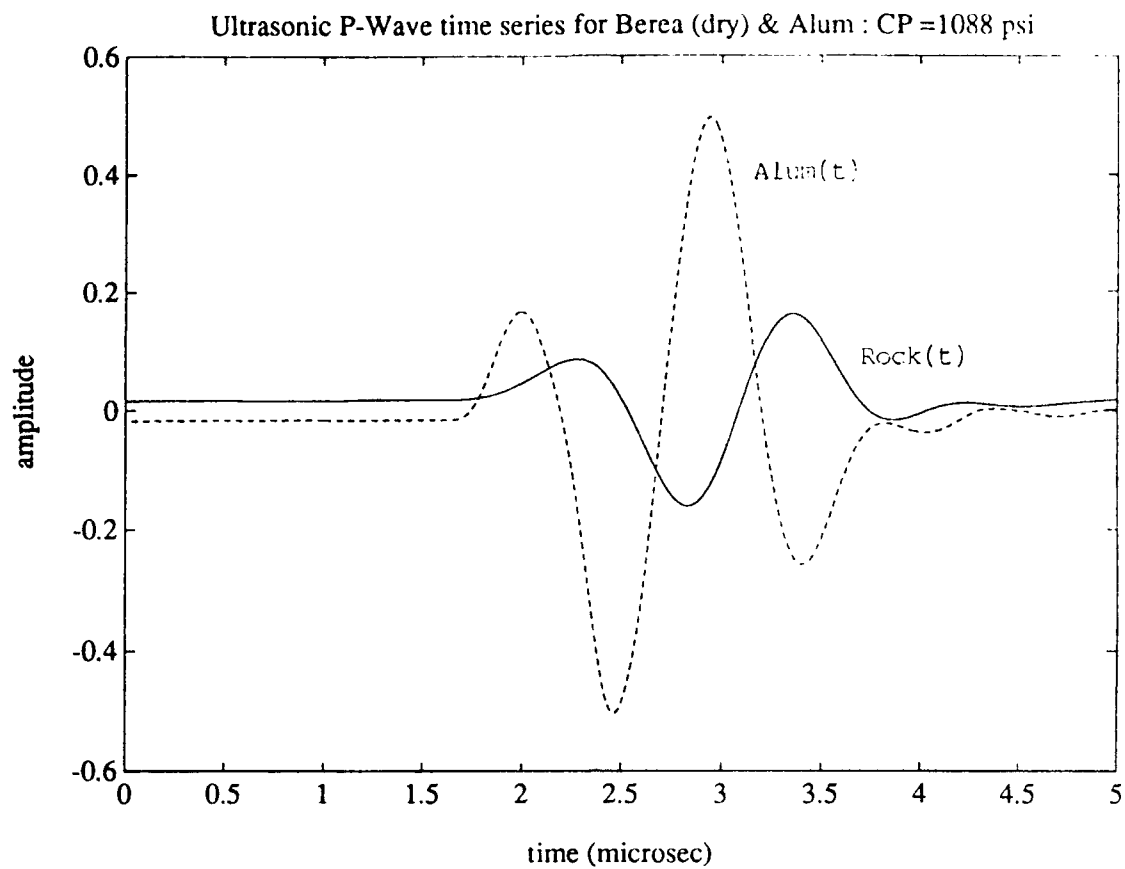
Ultrasonic P-Wave time series for Berea (dry) & Alum : CP =1088 psi

Ultrasonic S-Wave time series for Berea (dry) & Alum : CP =1088 psi

Figure 1

71

$$k = \frac{2 \pi f}{v}$$

In the frequency range from 0.1 to 1.0 MHz, α is assumed to be linear (Toksoz et al., 1979) thus,

$$\alpha(f) = \gamma f$$

where γ is a constant related to the quality factor of attenuation.
Taking the spectral ratio reduces to

$$\frac{A(f)}{R(f)} = \frac{G_A}{G_R} e^{-(\gamma_A x_A - \gamma_R x_R)f} \tag{3}$$

Taking the natural log (3) becomes

$$\ln\left(\frac{A(f)}{R(f)}\right) = (\gamma_R x_R - \gamma_A x_A) f + \ln\left(\frac{G_A}{G_R}\right) \tag{4}$$

and

$$\gamma = \frac{\pi}{Q v}$$

where Q is the quality factor. Substitute Q into equation (4) yields

$$\ln\left(\frac{A(f)}{R(f)}\right) = \left(\frac{x_R}{Q_R v_R} - \frac{x_A}{Q_A v_A}\right) \pi f + \ln\left(\frac{G_A}{G_R}\right) \tag{5}$$

For the aluminum reference, $Q_A v_A$ is very large ($Q_A = 150,000$), thus γ_A is approximately zero. Equation (5) further reduces to

$$\ln\left(\frac{A(f)}{R(f)}\right) = \frac{x_R \pi f}{Q_R v_R} + \ln\left(\frac{G_A}{G_R}\right) \tag{6}$$

The ratio of G_A to G_R is approximately constant over frequency, thus taking the derivative with respect to frequency will drop that term, accounting for the extrinsic losses. The value

72

of Q can then be determined from equation (6) where

$$\frac{d}{df}\left[\ln\left(\frac{A(f)}{R(f)}\right)\right] = \frac{x_R \pi}{Q_R v_R} \tag{7}$$

Q_R is best approximated by fitting a straight line to the left hand side of (7) defining the slope of the ratio with respect to frequency. Thus

$$Q_R = \frac{\pi x_R}{(v_R)\, slope} \tag{8}$$

This method is further exemplified in Figure 2. The spectra of recorded times series for dry Berea and aluminum are displayed in the top panel of Figure 2. The data were acquired during hydrostatic compression tests. The natural log of the spectral ratio as depicted in equation (6) is represented by the star points in the bottom panel of Figure 2. A least squares fit was applied to the ratio data and is represented by the solid line.

Only a portion of the spectral ratio is fit. The spectral window length is determined by the following criteria:

1. The front end of the window is determined by the aluminum spectrum. This point is chosen 3, 10 , or 20 db down from the maximum aluminum amplitude.

2. The back end of the window is determined by the rock spectrum. This point is chosen 3, 10 , or 20 db down from the maximum rock amplitude.

In the example in Figure 2, the end points are determined 3 db from the maximums. To note, 3 db down is the half power point. The ultrasonic pulse and spectral ratio technique to determine Q is further explained in detail by Toksoz et al. 1979 and Spencer, 1979.

ULTRASONIC Q RESULTS

Ultrasonic velocities and time series were measured during hydrostatic compression tests up to 13,750 psi. Results are shown for dry and saturated Berea sandstone samples. Dry compressional and shear wave velocities, Vp and Vs are shown in Figure 3. The signal quality was good to excellent and there is a high degree of confidence in the first arrival picks. The signal times series are also of good quality allowing for reliable spectral data. Qp and Qs are plotted in Figure 4 as a function of pressure. The actual calculations of Q from the measured data are represented by the point markers. A polynomial curve fit is applied to the data and also shown. Vp and Vs are shown in the top panel of Figure 5 for saturated Berea. The pore pressure was held constant at 145 psi. Qp and Qs are shown
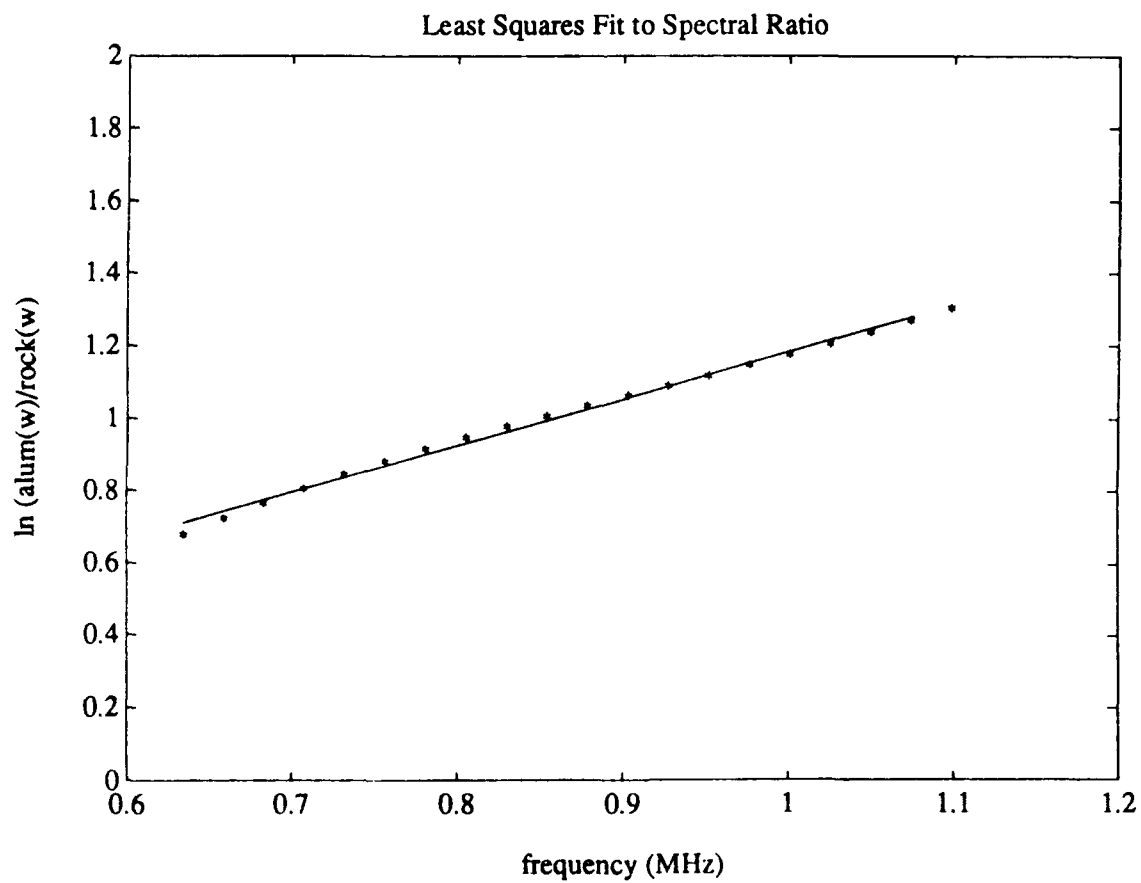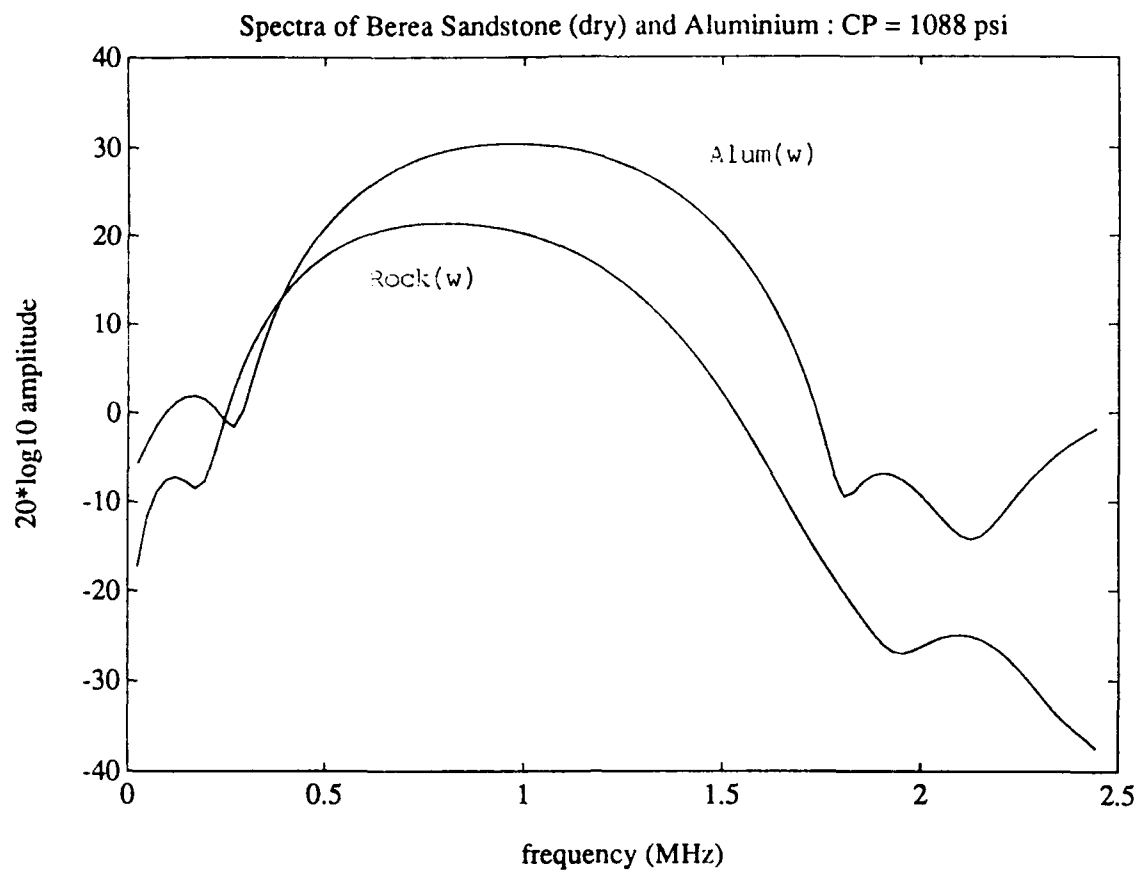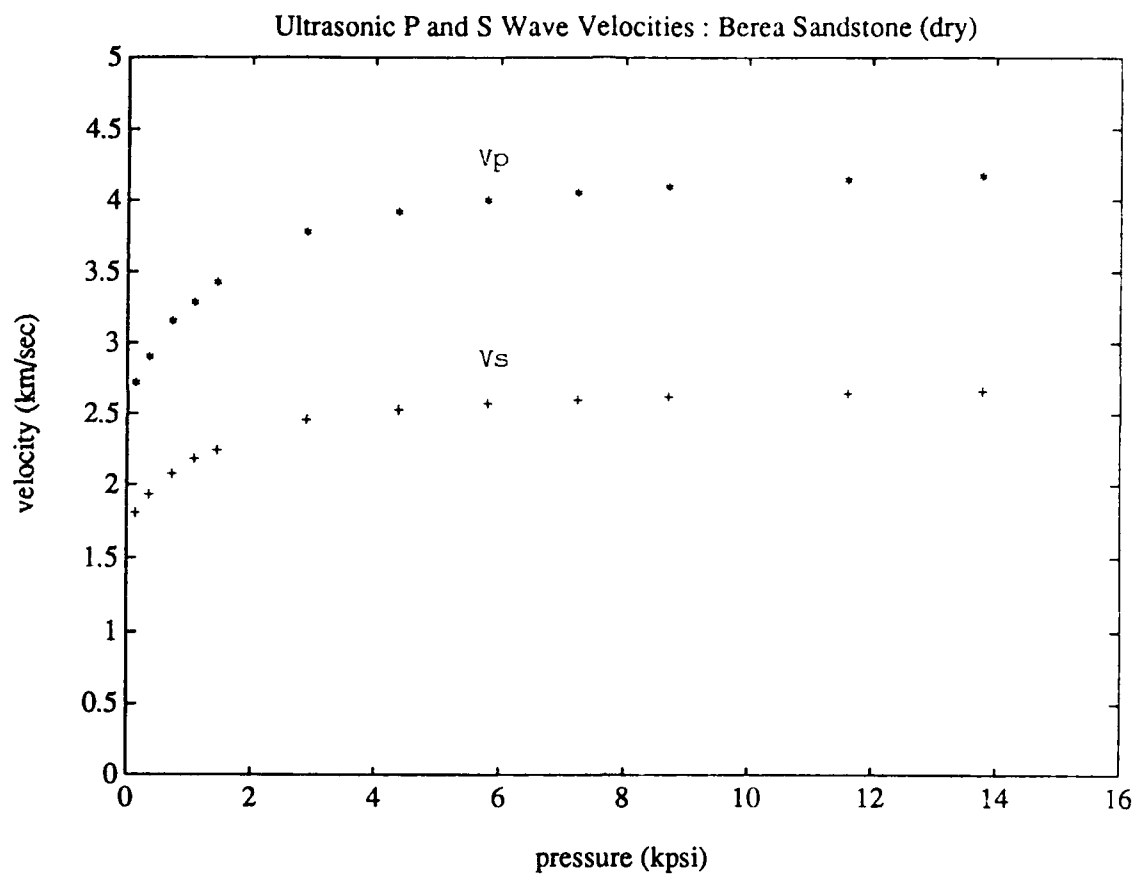
Spectra of Berea Sandstone (dry) and Aluminium : CP = 1088 psi

Least Squares Fit to Spectral Ratio

Figure 2

74

Figure 3

Ultrasonic P-Wave Attenuation : Berea sandstone (dry)

Ultrasonic S-Wave Attenuation : Berea sandstone (dry)

Figure 4

Ultrasonic P and S-Wave Velocities : Berea (saturated)

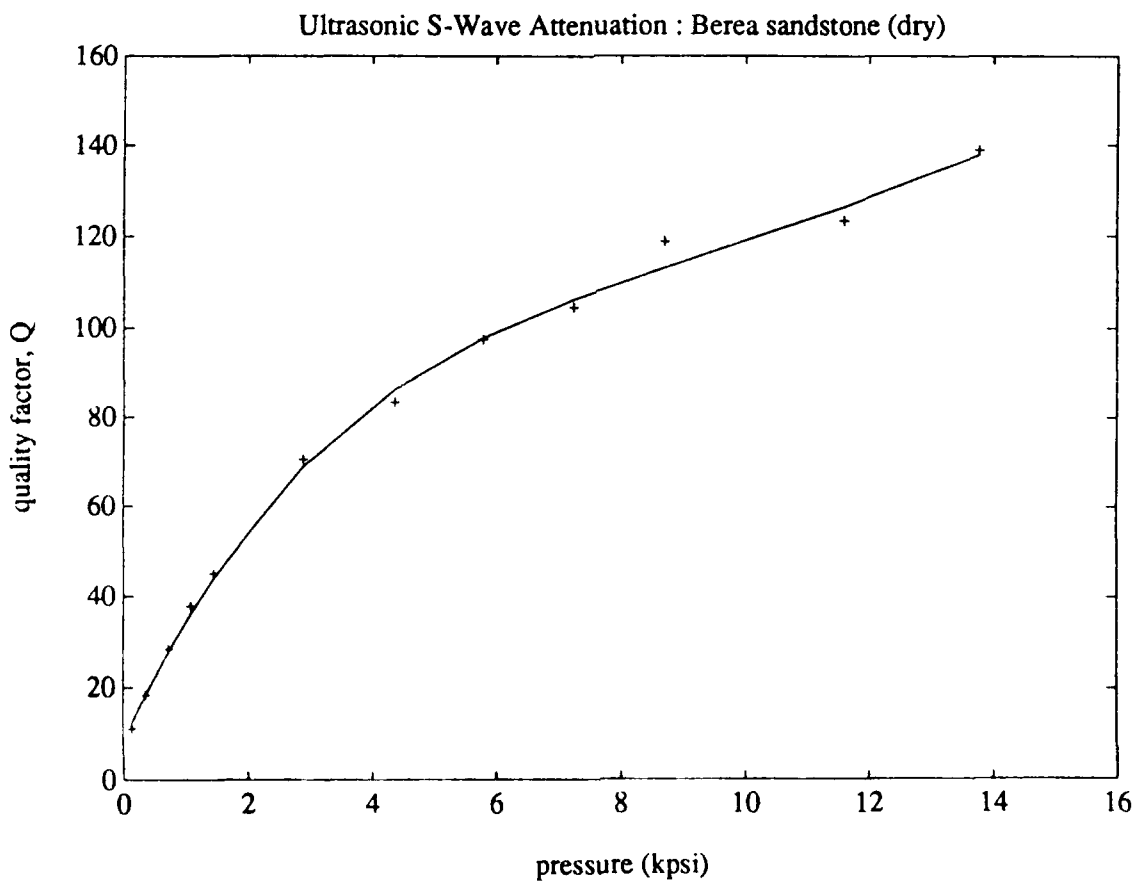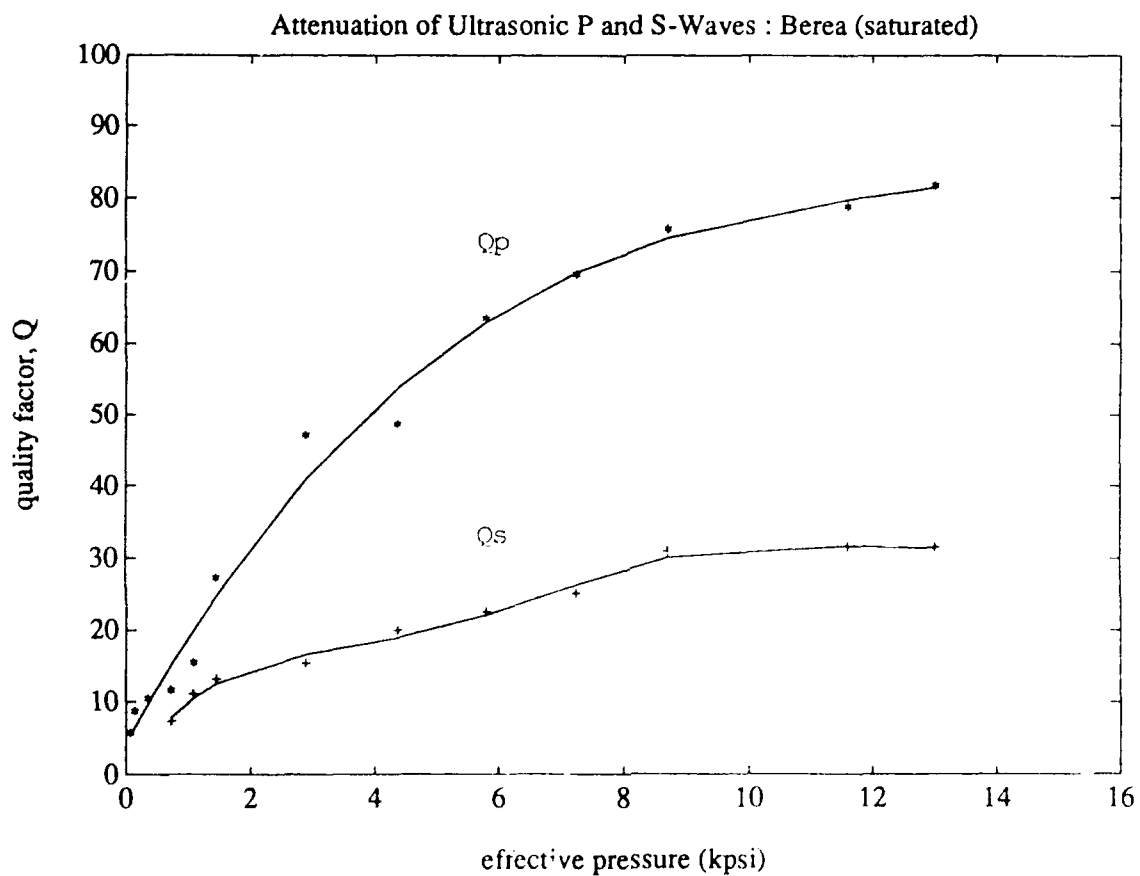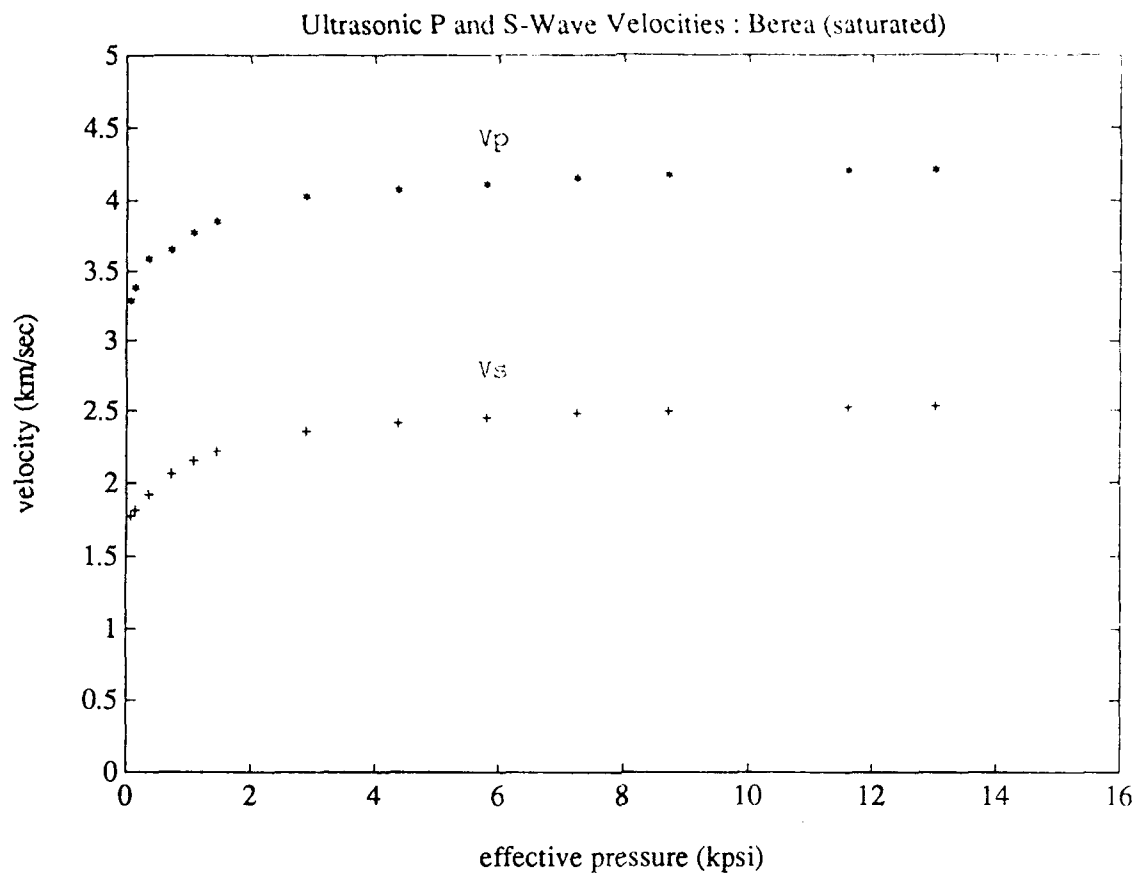## Attenuation of Ultrasonic P and S-Waves : Berea (saturated)

77
Figure 5
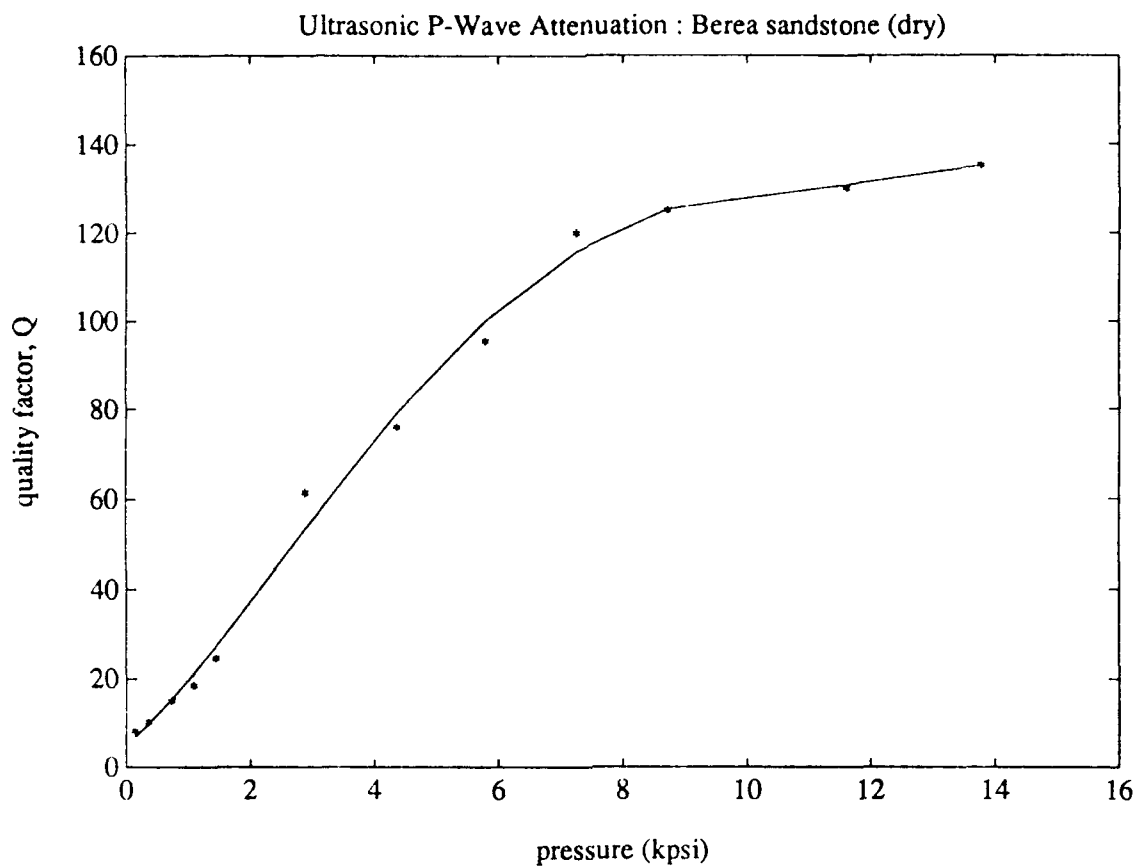
in the lower panel.

Q_E, (from anelastic Young's Modulus) is calculated from Qs and Qp in order to compare to the Hysteresis Loop and Resonant Bar Experimental values of Q_E. This ultrasonic parameter is as follows:

$$\frac{1+v}{Q_E} = \frac{(1-v)(1-2v)}{Q_P} + \frac{2v(2-v)}{Q_S} \tag{9}$$

where v is Poisson's Ratio and is determined from the ultrasonic velocities, Vp and Vs below:

$$v = \frac{V_p^2 - 2V_s^2}{2(V_p^2 - V_s^2)}$$

Poisson's Ratio is shown for the dry and saturated cases in the top panel of Figure 6. Q_E is shown for the dry and saturated cases in the bottom panel.

The ultrasonic Q is strongly dependent upon pressure. In the dry condition, Qp, Qs, and v are very comparable i.. value at each pressure increment. The rock strain is on the order of millistrain to 10's of millistrain due to the hydrostatic load (Martin et al., 1990, Haupt and Martin, 1991). As pressure increases, the porosity decreases with pore collapse and crack closure. Note that the rock strain due to the ultrasonic pulse is less than 1 microstrain. Thus, the rock is changing considerably with pressure and in turn strongly affects the attenuation and velocity. For the saturated condition the presence of water and pressure, both greatly affect Q_E. The effect of saturation suppresses Q with pressure as compared to the dry condition, especially for Qs and in turn Q_E.

Poissons Ratio - from Ultrasonic Velocity : Berea Sandstone

Ultrasonic QE : Berea Sandstone

Figure 6
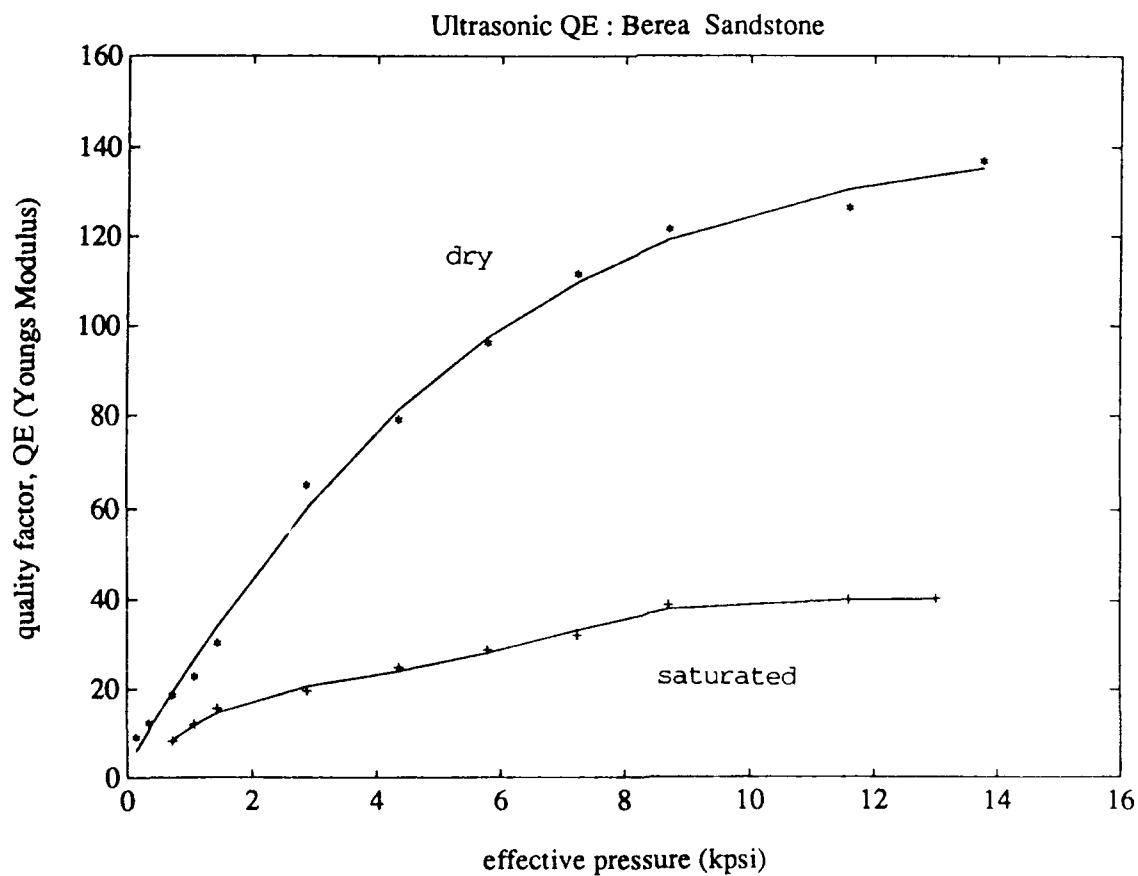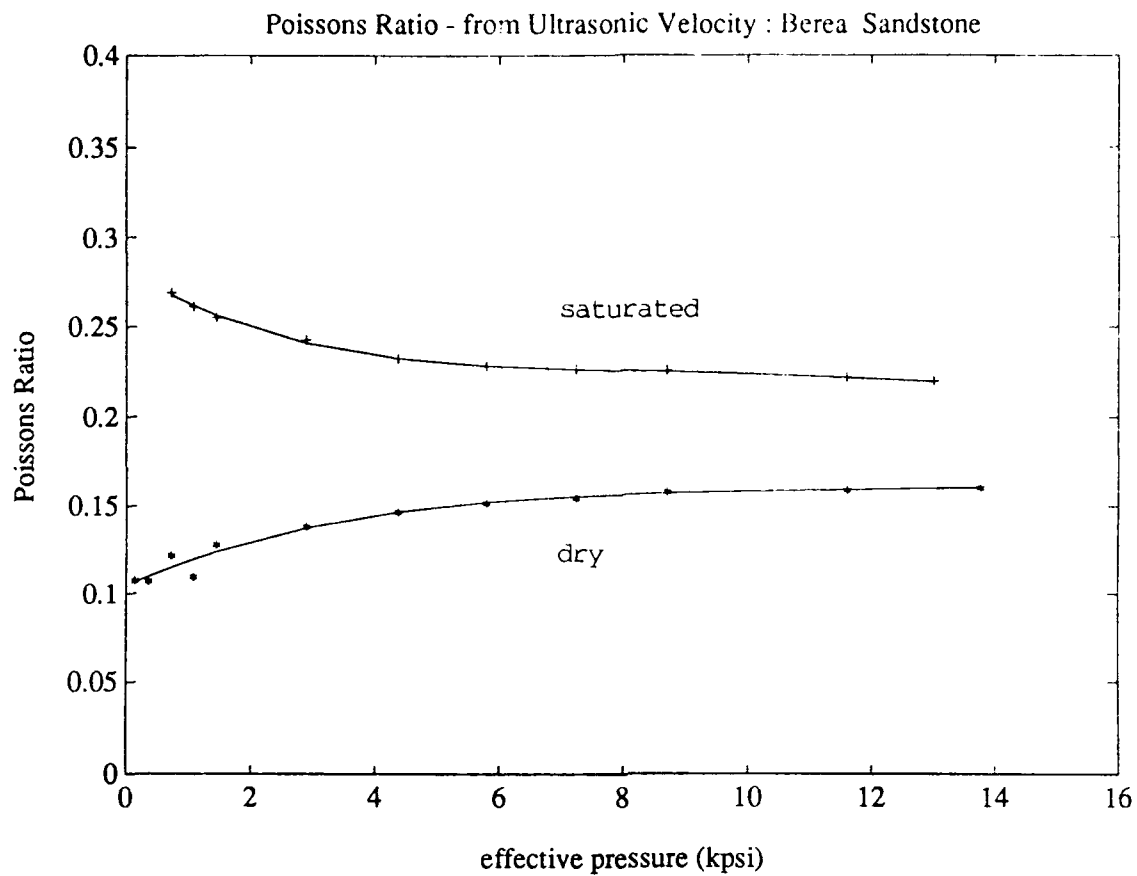
Prof. Thomas Ahrens
Seismological Lab, 252-21
Division of Geological & Planetary Sciences
California Institute of Technology
Pasadena, CA 91125

Prof. Keiiti Aki
Center for Earth Sciences
University of Southern California
University Park
Los Angeles, CA 90089-0741

Prof. Shelton Alexander
Geosciences Department
403 Deike Building
The Pennsylvania State University
University Park, PA 16802

Dr. Ralph Alewine, III
DARPA/NMRO
3701 North Fairfax Drive
Arlington, VA 22203-1714

Prof. Charles B. Archambeau
CIRES
University of Colorado
Boulder, CO 80309

Dr. Thomas C. Bache, Jr.
Science Applications Int'l Corp.
10260 Campus Point Drive
San Diego, CA 92121 (2 copies)

Prof. Muawia Barazangi
Institute for the Study of the Continent
Cornell University
Ithaca, NY 14853

Dr. Jeff Barker
Department of Geological Sciences
State University of New York
 at Binghamton
Vestal, NY 13901

Dr. Douglas R. Baumgardt
ENSCO, Inc
5400 Port Royal Road
Springfield, VA 22151-2388

Dr. Susan Beck
Department of Geosciences
Building #77
University of Arizona
Tuscon, AZ 85721

Dr. T.J. Bennett
S-CUBED
A Division of Maxwell Laboratories
11800 Sunrise Valley Drive, Suite 1212
Reston, VA 22091

Dr. Robert Blandford
AFTAC/TT, Center for Seismic Studies
1300 North 17th Street
Suite 1450
Arlington, VA 22209-2308

Dr. G.A. Bollinger
Department of Geological Sciences
Virginia Polytechnical Institute
21044 Derring Hall
Blacksburg, VA 24061

Dr. Stephen Bratt
Center for Seismic Studies
1300 North 17th Street
Suite 1450
Arlington, VA 22209-2308

Dr. Lawrence Burdick
Woodward-Clyde Consultants
566 El Dorado Street
Pasadena, CA 91109-3245

Dr. Robert Burridge
Schlumberger-Doll Research Center
Old Quarry Road
Ridgefield, CT 06877

Dr. Jerry Carter
Center for Seismic Studies
1300 North 17th Street
Suite 1450
Arlington, VA 22209-2308

Dr. Eric Chael
Division 9241
Sandia Laboratory
Albuquerque, NM 87185

Prof. Vernon F. Cormier
Department of Geology & Geophysics
U-45, Room 207
University of Connecticut
Storrs, CT 06268

Prof. Steven Day
Department of Geological Sciences
San Diego State University
San Diego, CA 92182

Marvin Denny
U.S. Department of Energy
Office of Arms Control
Washington, DC 20585

Dr. Zoltan Der
ENSCO, Inc.
5400 Port Royal Road
Springfield, VA 22151-2388

Prof. Adam Dziewonski
Hoffman Laboratory, Harvard University
Dept. of Earth Atmos. & Planetary Sciences
20 Oxford Street
Cambridge, MA 02138

Prof. John Ebel
Department of Geology & Geophysics
Boston College
Chestnut Hill, MA 02167

Eric Fielding
SNEE Hall
INSTOC
Cornell University
Ithaca, NY 14853

Dr. Mark D. Fisk
Mission Research Corporation
735 State Street
P.O. Drawer 719
Santa Barbara, CA 93102

Prof Stanley Flatte
Applied Sciences Building
University of California, Santa Cruz
Santa Cruz, CA 95064

Dr. John Foley
NER-Geo Sciences
1100 Crown Colony Drive
Quincy, MA 02169

Prof. Donald Forsyth
Department of Geological Sciences
Brown University
Providence, RI 02912

Dr. Art Frankel
U.S. Geological Survey
922 National Center
Reston, VA 22092

Dr. Cliff Frolich
Institute of Geophysics
8701 North Mopac
Austin, TX 78759

Dr. Holly Given
IGPP, A-025
Scripps Institute of Oceanography
University of California, San Diego
La Jolla, CA 92093

Dr. Jeffrey W. Given
SAIC
10260 Campus Point Drive
San Diego, CA 92121

Dr. Dale Glover
Defense Intelligence Agency
ATTN: ODT-1B
Washington, DC 20301

Dr. Indra Gupta
Teledyne Geotech
314 Montgomery Street
Alexanderia, VA 22314

Dan N. Hagedon
Pacific Northwest Laboratories
Battelle Boulevard
Richland, WA 99352

Dr. James Hannon
Lawrence Livermore National Laboratory
P.O. Box 808
L-205
Livermore, CA 94550

Dr. Roger Hansen
HQ AFTAC/TTR
Patrick AFB, FL 32925-6001

Prof. David G. Harkrider
Seismological Laboratory
Division of Geological & Planetary Sciences
California Institute of Technology
Pasadena, CA 91125

Prof. Danny Harvey
CIRES
University of Colorado
Boulder, CO 80309

2

Prof. Donald V. Helmberger
Seismological Laboratory
Division of Geological & Planetary Sciences
California Institute of Technology
Pasadena, CA 91125

Prof. Eugene Herrin
Institute for the Study of Earth and Man
Geophysical Laboratory
Southern Methodist University
Dallas, TX 75275

Prof. Robert B. Herrmann
Department of Earth & Atmospheric Sciences
St. Louis University
St. Louis, MO 63156

Prof. Lane R. Johnson
Seismographic Station
University of California
Berkeley, CA 94720

Prof. Thomas H. Jordan
Department of Earth, Atmospheric &
 Planetary Sciences
Massachusetts Institute of Technology
Cambridge, MA 02139

Prof. Alan Kafka
Department of Geology & Geophysics
Boston College
Chestnut Hill, MA 02167

Robert C. Kemerait
ENSCO, Inc.
445 Pineda Court
Melbourne, FL 32940

Dr. Max Koontz
U.S. Dept. of Energy/DP 5
Forrestal Building
1000 Independence Avenue
Washington, DC 20585

Dr. Richard LaCoss
MIT Lincoln Laboratory, M-200B
P.O. Box 73
Lexington, MA 02173-0073

Dr. Fred K. Lamb
University of Illinois at Urbana-Champaign
Department of Physics
1110 West Green Street
Urbana, IL 61801

Prof. Charles A. Langston
Geosciences Department
403 Deike Building
The Pennsylvania State University
University Park, PA 16802

Jim Lawson, Chief Geophysicist
Oklahoma Geological Survey
Oklahoma Geophysical Observatory
P.O. Box 8
Leonard, OK 74043-0008

Prof. Thorne Lay
Institute of Tectonics
Earth Science Board
University of California, Santa Cruz
Santa Cruz, CA 95064

Dr. William Leith
U.S. Geological Survey
Mail Stop 928
Reston, VA 22092

Mr. James F. Lewkowicz
Phillips Laboratory/GPEH
Hanscom AFB, MA 01731-5000(2 copies)

Mr. Alfred Lieberman
ACDA/VI-OA State Department Building
Room 5726
320-21st Street, NW
Washington, DC 20451

Prof. L. Timothy Long
School of Geophysical Sciences
Georgia Institute of Technology
Atlanta, GA 30332

Dr. Randolph Martin, III
New England Research, Inc.
76 Olcott Drive
White River Junction, VT 05001

Dr. Robert Masse
Denver Federal Building
Box 25046, Mail Stop 967
Denver, CO 80225

Dr. Gary McCartor
Department of Physics
Southern Methodist University
Dallas, TX 75275

Prof. Thomas V. McEvilly
Seismographic Station
University of California
Berkeley, CA 94720

Prof. John A. Orcutt
IGPP, A-025
Scripps Institute of Oceanography
University of California, San Diego
La Jolla, CA 92093

Dr. Art McGarr
U.S. Geological Survey
Mail Stop 977
U.S. Geological Survey
Menlo Park, CA 94025

Prof. Jeffrey Park
Kline Geology Laboratory
P.O. Box 6666
New Haven, CT 06511-8130

Dr. Keith L. McLaughlin
S-CUBED
A Division of Maxwell Laboratory
P.O. Box 1620
La Jolla, CA 92038-1620

Dr. Howard Patton
Lawrence Livermore National Laboratory
L-025
P.O. Box 808
Livermore, CA 94550

Stephen Miller & Dr. Alexander Florence
SRI International
333 Ravenswood Avenue
Box AF 116
Menlo Park, CA 94025-3493

Dr. Frank Pilotte
HQ AFTAC/TT
Patrick AFB, FL 32925-6001

Prof. Bernard Minster
IGPP, A-025
Scripps Institute of Oceanography
University of California, San Diego
La Jolla, CA 92093

Dr. Jay J. Pulli
Radix Systems, Inc.
2 Taft Court, Suite 203
Rockville, MD 20850

Prof. Brian J. Mitchell
Department of Earth & Atmospheric Sciences
St. Louis University
St. Louis, MO 63156

Dr. Robert Reinke
ATTN: FCTVTD
Field Command
Defense Nuclear Agency
Kirtland AFB, NM 87115

Mr. Jack Murphy
S-CUBED
A Division of Maxwell Laboratory
11800 Sunrise Valley Drive, Suite 1212
Reston, VA 22091 (2 Copies)

Prof. Paul G. Richards
Lamont-Doherty Geological Observatory
 of Columbia University
Palisades, NY 10964

Dr. Keith K. Nakanishi
Lawrence Livermore National Laboratory
L-025
P.O. Box 808
Livermore, CA 94550

Mr. Wilmer Rivers
Teledyne Geotech
314 Montgomery Street
Alexandria, VA 22314

Dr. Carl Newton
Los Alamos National Laboratory
P.O. Box 1663
Mail Stop C335, Group ESS-3
Los Alamos, NM 87545

Dr. George Rothe
HQ AFTAC/TTR
Patrick AFB, FL 32925-6001

Dr. Bao Nguyen
HQ AFTAC/TTR
Patrick AFB, FL 32925-6001

Dr. Alan S. Ryall, Jr.
DARPA/NMRO
3701 North Fairfax Drive
Arlington, VA 22209-1714

Dr. Richard Sailor
TASC, Inc.
55 Walkers Brook Drive
Reading, MA 01867

Prof. Charles G. Sammis
Center for Earth Sciences
University of Southern California
University Park
Los Angeles, CA 90089-0741

Prof. Christopher H. Scholz
Lamont-Doherty Geological Observatory
 of Columbia University
Palisades, CA 10964
       N Y

Dr. Susan Schwartz
Institute of Tectonics
1156 High Street
Santa Cruz, CA 95064

Secretary of the Air Force
(SAFRD)
Washington, DC 20330

Office of the Secretary of Defense
DDR&E
Washington, DC 20330

Thomas J. Sereno, Jr.
Science Application Int'l Corp.
10260 Campus Point Drive
San Diego, CA 92121

Dr. Michael Shore
Defense Nuclear Agency/SPSS
6801 Telegraph Road
Alexandria, VA 22310

Dr. Matthew Sibol
Virginia Tech
Seismological Observatory
4044 Derring Hall
Blacksburg, VA 24061-0420

Prof. David G. Simpson
IRIS, Inc.
1616 North Fort Myer Drive
Suite 1440
Arlington, VA 22209

Donald L. Springer
Lawrence Livermore National Laboratory
L-025
P.O. Box 808
Livermore, CA 94550

Dr. Jeffrey Stevens
S-CUBED
A Division of Maxwell Laboratory
P.O. Box 1620
La Jolla, CA 92038-1620

Lt. Col. Jim Stobie
ATTN: AFOSR/NL
Bolling AFB
Washington, DC 20332-6448

Prof. Brian Stump
Institute for the Study of Earth & Man
Geophysical Laboratory
Southern Methodist University
Dallas, TX 75275

Prof. Jeremiah Sullivan
University of Illinois at Urbana-Champaign
Department of Physics
1110 West Green Street
Urbana, IL 61801

Prof. L. Sykes
Lamont-Doherty Geological Observatory
 of Columbia University
Palisades, NY 10964

Dr. David Taylor
ENSCO, Inc.
445 Pineda Court
Melbourne, FL 32940

Dr. Steven R. Taylor
Los Alamos National Laboratory
P.O. Box 1663
Mail Stop C335
Los Alamos, NM 87545

Prof. Clifford Thurber
University of Wisconsin-Madison
Department of Geology & Geophysics
1215 West Dayton Street
Madison, WS 53706

Prof. M. Nafi Toksoz
Earth Resources Lab
Massachusetts Institute of Technology
42 Carleton Street
Cambridge, MA 02142

5

Dr. Larry Turnbull
CIA-OSWR/NED
Washington, DC 20505

DARPA/RMO/SECURITY OFFICE
3701 North Fairfax Drive
Arlington, VA 22203-1714

Dr. Gregory van der Vink
IRIS, Inc.
1616 North Fort Myer Drive
Suite 1440
Arlington, VA 22209

HQ DNA
ATTN: Technical Library
Washington, DC 20305

Dr. Karl Veith
EG&G
5211 Auth Road
Suite 240
Suitland, MD 20746

Defense Intelligence Agency
Directorate for Scientific & Technical Intelligence
ATTN: DTIB
Washington, DC 20340-6158

Prof. Terry C. Wallace
Department of Geosciences
Building #77
University of Arizona
Tuscon, AZ 85721

Defense Technical Information Center
Cameron Station
Alexandria, VA 22314 (2 Copies)

Dr. Thomas Weaver
Los Alamos National Laboratory
P.O. Box 1663
Mail Stop C335
Los Alamos, NM 87545

TACTEC
Battelle Memorial Institute
505 King Avenue
Columbus, OH 43201 (Final Report)

Dr. William Wortman
Mission Research Corporation
8560 Cinderbed Road
Suite 700
Newington, VA 22122

Phillips Laboratory
ATTN: XPG
Hanscom AFB, MA 01731-5000

Prof. Francis T. Wu
Department of Geological Sciences
State University of New York
 at Binghamton
Vestal, NY 13901

Phillips Laboratory
ATTN: GPE
Hanscom AFB, MA 01731-5000

AFTAC/CA
(STINFO)
Patrick AFB, FL 32925-6001

Phillips Laboratory
ATTN: TSML
Hanscom AFB, MA 01731-5000

DARPA/PM
3701 North Fairfax Drive
Arlington, VA 22203-1714

Phillips Laboratory
ATTN: SUL
Kirtland, NM 87117 (2 copies)

DARPA/RMO/RETRIEVAL
3701 North Fairfax Drive
Arlington, VA 22203-1714

Dr. Michel Bouchon
I.R.I.G.M.-B.P. 68
38402 St. Martin D'Heres
Cedex, FRANCE

Dr. Michel Campillo
Observatoire de Grenoble
I.R.I.G.M.-B.P. 53
38041 Grenoble, FRANCE

Dr. Kin Yip Chun
Geophysics Division
Physics Department
University of Toronto
Ontario, CANADA

Prof. Hans-Peter Harjes
Institute for Geophysic   ·
Ruhr University/Bochum
P.O. Box 102148
4630 Bochum 1, GERMANY

Prof. Eystein Husebye
NTNF/NORSAR
P.O. Box 51
N-2007 Kjeller, NORWAY

David Jepsen
Acting Head, Nuclear Monitoring Section
Bureau of Mineral Resources
Geology and Geophysics
G.P.O. Box 378, Canberra, AUSTRALIA

Ms. Eva Johannisson
Senior Research Officer
National Defense Research Inst.
P.O. Box 27322
S-102 54 Stockholm, SWEDEN

Dr. Peter Marshall
Procurement Executive
Ministry of Defense
Blacknest, Brimpton
Reading FG7-FRS, UNITED KINGDOM

Dr. Bernard Massinon, Dr. Pierre Mechler
Societe Radiomana
27 rue Claude Bernard
75005 Paris, FRANCE (2 Copies)

Dr. Svein Mykkeltveit
NTNT/NORSAR
P.O. Box 51
N-2007 Kjeller, NORWAY (3 Copies)

Prof. Keith Priestley
University of Cambridge
Bullard Labs, Dept. of Earth Sciences
Madingley Rise, Madingley Road
Cambridge CB3 OEZ, ENGLAND

Dr. Jorg Schlittenhardt
Federal Institute for Geosciences & Nat'l Res.
Postfach 510153
D-3000 Hannover 51, GERMANY

Dr. Johannes Schweitzer
Institute of Geophysics
Ruhr University/Bochum
P.O. Box 1102148
4360 Bochum 1, GERMANY